# 國立交通大學

## 電子物理系

## 博士論文

# 超導與超穎材料週期多層結構之光學性質探討

# Optical Properties of Periodic Multilayer Structures Containing Superconductors and Metamaterials

研　究　生：陳美頌

指導教授：楊宗哲　教授

儒森斯坦　教授

中華民國九十八年八月

# 超導與超穎材料週期多層結構之光學性質探討

# Optical Properties of Periodic Multilayer Structures Containing Superconductors and Metamaterials


研 究 生:陳美頌　　Student : Mei-Soong Chen

指導教授:楊宗哲　教授　　Advisor : Prof. Tzong-Jer Yang

儒森斯坦 教授　　Prof. Baruch Rosenstein


國立交通大學

電子物理系

博士論文

**A Thesis**

**Submitted to Institute of Electrophysics**

**College of Science**

**National Chiao Tung University**

**in Partial Fulfillment of the Requirements**

**for the Degree of**

**Doctor of Philosophy**

**in Electrophysics**

**August 2009**

**Hsinchu, Taiwan**

中 華 民 國 九 十 八 年 八 月

# 超導與超穎材料週期多層結構之光學性質探討

研 究 生:陳美頌　　指導教授:楊宗哲　教授

儒森斯坦 教授

國立交通大學電子物理系博士班

## 摘要

週期性多層膜結構的光學理論已發展了一段時間，過去採用的材料主要偏向於介電體，半導體以及金屬。近年來，許多不同於這些早期傳統的材料，例如超導體以及超穎材料，已被陸續開發出來。我們的研究工作重點，是將超導體材料(superconductors)及超穎材料(metamaterials)置於多層膜的結構中，探討電磁波在此週期性排列結構中的傳播特性以及光學能帶分佈，企圖尋求其特殊性質以及可應用功能的開發。對於一維的超導體的光子晶體，我們採用超導體的二流體模型理論來進行研究。從計算出的穿透頻譜和光子能帶圖，發現兩者幾乎完全的吻合。我們進一步對於二維的週期性多層膜的環型結構進行探討，採用克利提夫斯基(Kaliteevski)的計算理論，以圓柱波的轉移矩陣計算方式分別針對超導體材料及超穎材料來進行數值分析。計算會隨著頻率改變的介電係數(permittivity)和磁感係數(permeability)進而繪出反射頻譜，經過研究探討後，我們發現在材料的電漿頻率處附近圓柱波與平面波有截然不同的反應，此種特殊現象對於未來在通訊上設計濾波器或者共振器將有很大的助益。

# Optical Properties of Periodic Multilayer Structures Containing Superconductors and Metamaterials

**Student : Mei-Soong Chen** **Advisor : Prof. Tzong-Jer Yang**

**Prof. Baruch Rosenstein**

**Institute of Electrophysics**

**National Chiao Tung University**

## ABSTRACT

It has been developed for periods of time to research the optical properties of periodic multilayer structures. In the past years, the photonic band gap structure were mainly fabricated by using the usual dielectrics, semiconductor and metal as well. Recently, the new materials like superconductors and the metamaterials have been developed very soon. The main purpose of our research work is to study the optical properties of the periodic multilayer structures with superconductors and metamaterials. The discussions of photonic band structure have been made and we attempt to seek some unusual phenomena and the special property for application. The photonic band structure in the transversal electric mode for a one-dimensional superconductor-dielectric superlattice is theoretically calculated. By using the two-fluid model of superconductors, the band structure is shown be strongly consistent with the transmittance spectrum. Next, we investigate the optical properties of the annular Bragg reflectors containing superconductors and metamaterials. By using the transfer matrix method for the cylindrical waves developed by Kaliteevski *et al.*, we calculate the reflectance spectra for the annular Bragg reflectors. Numerical results show that the optical properties of the annular Bragg reflectors are fundamentally different from those of the planar Bragg reflector with azimuthal mode number $m \geq 1$. The special results suggest that the annular Bragg reflectors could be used to design a narrowband transmission filter or an annular resonator without introducing any physical defect layer in the structure.

# Acknowledgement

I would like to express my sincere gratitude to my advisors professor Tzong-Jer Yang (楊宗哲) and professor Baruch Rosenstein (儒森斯坦) for their guidance and support on my research. I would also like to show my deep appreciation to professor Chien-Jang Wu（吳謙讓）for his assistance during my thesis work. Finally, I am grateful to my family for the encouragement and love from them.

# Publication List

**Papers**： ( *：Corresponding Author)

1. M.-S. Chen, C.-J. Wu*, and T.-J Yang*, “Optical properties of a superconducting annular periodic multilayer structure”, Solid State Communications (available online).
2. M.-S. Chen*, C.-J. Wu, and T.-J Yang, “Wave properties of an annular periodic multilayer structure containing the single-negative materials”, Physics Letters A 373 (2009) 3594.
3. C.-J. Wu*, M.-S. Chen and T.-J Yang, “Photonic band structure for a superconductor-dielectric superlattice”, Physica C 432 (2005) 133.
4. L. Chen, D. Li, and B. Rosenstein, “Supercooled vortex liquid and superheated vortex solid in type II superconductors”, Chinese Journal of Physics, Vol.43, No. 3-II (2005) 598.

# Contents

# List of Figures

# Chapter 1
# Introduction

## 1.1 Background

Recently much work has been done on the computation of the photonic band structures of electromagnetic waves propagating in the periodic multilayer structures, because these periodic structures can be designed to produce the required photonic band structure. In the dissertation, we shall investigate the photonic band structures of the superconductor-dielectric superlattice and the annular periodic multilayer structure containing the superconducting materials, the single-negative materials or the double-negative materials.



### 1.1.1 Photonic crystals

In 1987, E. Yablonovitch and S. John provided the concept of photonic crystals (PCs), respectively [1-4]. In solid state physics there are electronic band diagrams for a crystal with the periodic arrangement of atoms or molecules. With the optical analogy it is known that PCs have photonic band gaps (PBGs) at which the electromagnetic waves cannot propagate through the periodic layered structures. When transmitting in a periodic media structure the light waves will interference destructively and then they are forbidden to propagate at special frequencies, that is, the PBGs will be formed in some frequency regions [5,6]. Photonic crystals can be in the one-dimensional, two-dimensional or three-dimensional periodic structures. (See Fig.1.1)

For the photonic band structures in the PCs, there are many physical ideas are from the solid state physics, such as the reciprocal lattice space, Brillouin zone and Bloch

theory as well. In solid state physics the wave motion of an electron is described by the Schrodinger equation

$$-\frac{\hbar^2}{2m}\nabla^2 + V(\vec{r})\psi = E\psi\,, \tag{1.1}$$

where

$$V(\vec{r}) = V(\vec{r} + \vec{R}_n)\,. \tag{1.2}$$

However, in the PCs the wave propagating of an photon satisfies the following wave equation,

$$-\nabla^2\vec{E} + \nabla(\nabla\cdot\vec{E}) - \frac{\omega^2}{c^2}\varepsilon(\vec{r})\vec{E} = \frac{\omega^2}{c^2}\varepsilon_0\vec{E}\,, \tag{1.3}$$

where the permittivity function is periodic, i.e.,

$$\varepsilon(\vec{r}) = \varepsilon(\vec{r} + \vec{R}_l)\,. \tag{1.4}$$

Comparing these two equations, we can establish the analogous relations as follows:

$$\frac{\omega^2}{c^2}\varepsilon(\vec{r}) \to V(\vec{r})\,, \tag{1.5}$$

$$\varepsilon_0\frac{\omega^2}{c^2} \to \vec{E}\,. \tag{1.6}$$

Although some similar physical meanings are in common for both the photonic crystals and the electrons in a solid, it should be noted that they have a fundamental difference, that is, the photons are bosons while the electrons are fermions.

To investigate the photonic band structure, there are, at present, three main numerical methods include the transfer matrix method (TMM), plane wave expansion (PWE) and finite-difference-time-domain (FDTD). Because the photon-photon interaction force is very small, the photonic crystal is a lattice which is quite suitable to examine and the Bloch theory can be employed.

For the study of a one-dimensional photonic crystal, we shall use the Abeles theory [7] for stratified layers to calculate the frequency-dependent transmittance, and calculate the band structure from the transcendental equation derived from the transfer matrix

method and the Bloch theorem [8]. The comparison between the transmittance spectrum and band structure shows excellent agreement for both methods.

### 1.1.2 Annular Bragg reflectors

A Bragg reflector with an annular geometric structure is shown in Fig. 1.2. With the advance of modern fabrication techniques the annular Bragg reflector has now been achievable. By creating a ring defect into the annular periodic multilayer structure, an annular resonator or laser has been recently reported [9,10]. Such an annular laser has a very important feature of vertical emission which makes it of particular use in the optical electronics and communication. Motivated by these facts, we shall also theoretically investigate the optical reflection properties of the annular Bragg reflector. In our analysis we use the transfer matrix method for the cylindrical waves developed by Kaliteevski *et al.* [11] to calculate the photonic band structures.

### 1.1.3 Superconductors in periodic multilayers structures

Kamerling Onnes discovered superconductivity in 1911, just three years after he had first liquefied helium. It was found in their laboratory that the resistance of Hg vanished at 4.2 K, the temperature of liquefied helium. For decades, a succession of theories on superconductivity were developed, for examples: Meissner effect, two-fluid model, London theory, Ginzburg-Landau (GL) theory and BCS theory.[12-15] A perfect diamagnetism of superconductors called the Meissner effect was found by Meissner and Ochsenfeld in 1933. For the electronic conduction mechanism of superconductors, Gorter and Casimir developed the two-fluid model in 1934. They assumed that in the superconductivity state there are two kinds of conduction electrons, one of which is normal electrons $n_n$ and another is electrons in superfluid state $n_s$. Based on the two-fluid model, famous London equations were provided in1935. Therefore the concept

of two-fluid model is very important and paves the way to the electrodynamics of superconductors.

In 1986, a new class of high-temperature superconductors (HTS) was discovered by Müller and Bednorz, which was a new era for superconductors. Because the HTS have the low resistance as well as the electronic conduction characteristic different from the metallic materials, the massive manpower and the financial resource have been spent to research and develop the HTS technology and the HTS electronic products for many years. While the preparation technology of superconductor thin films is getting mature, the application of superconductor materials is more broadened. It is seen that superconductors are frequently applied for the microwave devices and communication system owing to good microwave characteristics and the low impedance [16,17].

In the earlier stage, the photonic band gap structures were mainly fabricated by using the usual dielectrics, semiconductors and metals as well. Recently, the properties of the photonic band structures in a periodic multilayer structure consisting of superconducting and dielectric materials have also been researched [18-22]. In this work the optical reflection properties of a superconductor-dielectric superlattice and a superconducting annular Bragg reflector (SABR) are theoretically investigated. Regarding the superconductors of periodic multilayers structures, we calculate the index of refraction on the basis of the conventional two-fluid model.

### 1.1.4 Metamaterials in periodic multilayers structures

The electromagnetic metamaterials with both the negative permittivity $(\varepsilon < 0)$ and negative permeability $(\mu < 0)$ first predicted by Veselago early in 1968 [23] are now called the double-negative (DNG) materials. A significant result coming from the DNG material is that its index of refraction is negative. Thus, a DNG material is

commonly referred to as the negative-index material (NIM). The existence of this kind material was respectively experimentally demonstrated by Smith *et al*. [24,25] and one of the distinctive applications of the DNG materials was presented by Pendry. [26]

In addition to the DNG materials [27-30], the single-negative (SNG) materials also attract much attention recently. An SNG material means that only one of the two material parameters, $\varepsilon$ and $\mu$, is negative [31-33]. Thus an SNG material could be the epsilon-negative (ENG) medium with $\varepsilon < 0$ and $\mu > 0$ or the mu-negative (MNG) medium with $\mu < 0$ and $\varepsilon > 0$.

## 1.2 Preface of this dissertation

In the dissertation, we present the studies of the optical properties of periodic multilayers structures, which include the one-dimension superlattices and the annular Bragg reflectors as well. The materials we investigate for periodic multilayers comprise superconductors, single-negative metamaterials and double-negative metamaterials.

The Chapter 2 depicts basic theory of this dissertation. The PBGs in the superconductor-dielectric superlattices are described in Chapter 3. Optical properties of the SABR are reported in Chapter 4. We propose the photonic band structure of the annular periodic multilayer structure containing the single-negative materials in Chapter 5. Moreover, we discuss the wave properties of the annular periodic multilayer structure with the double-negative materials in Chapter 6. Finally, a conclusion of the results will be included in Chapter 7.

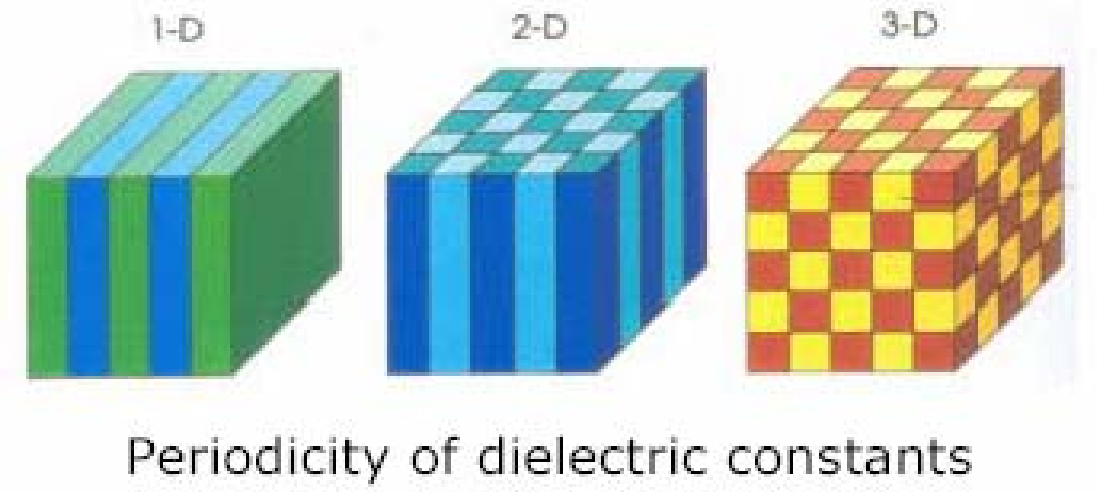


**Fig. 1.1.** The photonic crystal structures.

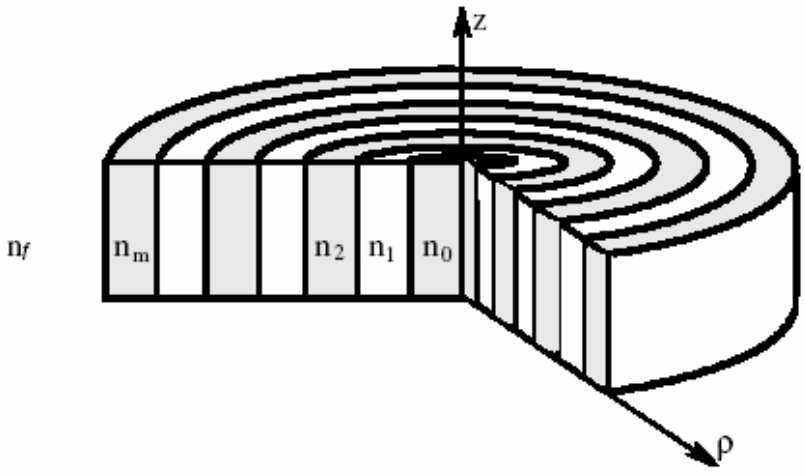


**Fig. 1.2.** An illustration of a multilayered structure with circular cylindrical symmetry. The figure is imaged from [11]

# Chapter 2
# Basic theory

## 2.1 Abeles theory

In order to calculate the transmittance and reflectance for a periodic multilayered structure, the elegant Abeles theory will be employed [7]. According to this theory, we must, in advance, set up the characteristic matrix corresponding to one period, with the result

$$\mathbf{M}(a)=\begin{bmatrix} m_{11} & m_{12} \\ m_{21} & m_{22} \end{bmatrix}=\begin{bmatrix} \cos\beta_2 & \frac{j}{p_2}\sin\beta_2 \\ jp_2\sin\beta_2 & \cos\beta_2 \end{bmatrix}\begin{bmatrix} \cos\beta_3 & \frac{j}{p_3}\sin\beta_3 \\ jp_3\sin\beta_3 & \cos\beta_3 \end{bmatrix}$$

$$=\begin{bmatrix} \cos\beta_2\cos\beta_3-\frac{p_3}{p_2}\sin\beta_2\sin\beta_3 & \frac{j}{p_3}\cos\beta_2\sin\beta_3+\frac{j}{p_2}\sin\beta_2\cos\beta_3 \\ jp_2\sin\beta_2\cos\beta_3+jp_3\cos\beta_2\sin\beta_3 & \cos\beta_2\cos\beta_3-\frac{p_2}{p_3}\sin\beta_2\sin\beta_3 \end{bmatrix}, \quad (2.1.1)$$

where $$\beta_2=\frac{2\pi}{\lambda_0}n_2a_2\cos\theta_2, \quad \beta_3=\frac{2\pi}{\lambda_0}n_3a_3\cos\theta_3, \quad (2.1.2)$$

and

$$p_2=\sqrt{\frac{\varepsilon_0}{\mu_0}}n_2\cos\theta_2, \quad p_3=\sqrt{\frac{\varepsilon_0}{\mu_0}}n_3\cos\theta_3, \quad (2.1.3)$$

where $\lambda_0=2\pi/k_0=2\pi c/\omega$ is the wavelength in free space. The angles $\theta_2$ and $\theta_3$, determined by Snell's law of refraction, are the ray angles in layer 2 and 3, respectively. Having constructed the matrix in Eq. (2.1.1), the total characteristic matrix for an *N*-period structure can be obtained, that is

$$\left[\mathbf{M}(Na)\right]=\begin{bmatrix} M_{11} & M_{12} \\ M_{21} & M_{22} \end{bmatrix}=\left[\mathbf{M}(a)\right]^N$$

$$= \begin{bmatrix} m_{11}U_{N-1}(\Psi) - U_{N-2}(\Psi) & m_{12}U_{N-1}(\Psi) \\ m_{21}U_{N-1}(\Psi) & m_{22}U_{N-1}(\Psi) - U_{N-2}(\Psi) \end{bmatrix}, \qquad (2.1.4)$$

where

$$\Psi = \frac{1}{2}(m_{11} + m_{22}), \qquad (2.1.5)$$

and $U_N$ are the Chebyshev polynomials of the second kind defined by

$$U_N(\Psi) = \frac{\sin\left[(N+1)\cos^{-1}\Psi\right]}{\sqrt{1-\Psi^2}}. \qquad (2.1.6)$$

Equation (2.1.4) gives the explicit expressions for matrix elements $M_{11}$, $M_{12}$, $M_{21}$, and $M_{22}$ as follows:

$$M_{11} = \left(\cos\beta_2\cos\beta_3 - \frac{p_3}{p_2}\sin\beta_2\sin\beta_3\right)U_{N-1}(\Psi) - U_{N-2}(\Psi)$$

$$M_{12} = j\left(\frac{1}{p_3}\cos\beta_2\sin\beta_3 + \frac{1}{p_2}\sin\beta_2\cos\beta_3\right)U_{N-1}(\Psi)$$

$$M_{21} = j\left(p_2\sin\beta_2\cos\beta_3 + p_3\cos\beta_2\sin\beta_3\right)U_{N-1}(\Psi)$$

$$M_{22} = \left(\cos\beta_2\cos\beta_3 - \frac{p_2}{p_3}\sin\beta_2\sin\beta_3\right)U_{N-1}(\Psi) - U_{N-2}(\Psi). \qquad (2.1.7)$$

The reflection and transmission coefficients can be determined and are given by [7]

$$\tilde{r} = \frac{(M_{11} + M_{12}p_\ell)p_1 - (M_{21} + M_{22}p_\ell)}{(M_{11} + M_{12}p_\ell)p_1 + (M_{21} + M_{22}p_\ell)}, \qquad (2.1.8)$$

and

$$\tilde{t} = \frac{2p_1}{(M_{11} + M_{12}p_\ell)p_1 + (M_{21} + M_{22}p_\ell)}. \qquad (2.1.9)$$

Here $p_1 = \sqrt{\varepsilon_0/\mu_0}\,(n_1\cos\theta_1)$ is for the first medium, and $p_\ell = \sqrt{\varepsilon_0/\mu_0}\,(n_\ell\cos\theta_\ell)$ is for the last medium. Both media here are taken to be free space. The reflectance (reflectivity) *R*, transmittance (transmissivity) *T* and $\tilde{r}$, $\tilde{t}$ are related by

$$R = |\tilde{r}|^2, \qquad T = \frac{p_\ell}{p_1}|\tilde{t}|^2. \tag{2.1.10}$$

Thus, the transmittance spectrum, $T$ versus $\omega$, can be numerically illustrated, as will be seen in Section III.

## 2.2 The Floquet (or Bloch) theorem

In the solid state physics, the wave function of a electron which has mass m will satisfied the Schrödinger equation

$$\left[-\frac{\hbar^2}{2m}\nabla^2 + V(\vec{r})\right]\psi(\vec{r}) = E\psi(\vec{r}), \tag{2.2.1}$$

where $V(\vec{r})$ is periodic electric field. If $\vec{R}$ is lattice transfer vector, then

$$V(\vec{r}) = V(\vec{r} + \vec{R}). \tag{2.2.2}$$

According Bloch theory [34], the solution of Eq. (2.2.1) is

$$\psi_{\vec{k}}(\vec{r}) = u(\vec{r})\exp(i\vec{k}\cdot\vec{r}), \tag{2.2.3}$$

where $$u(\vec{r}) = u(\vec{r} + \vec{R}). \tag{2.2.4}$$

This theory is also called Floquet theory, because Floquet is the first person to deduce the theory for one-dimensional case.

For the photonic crystal structure, we use Floquet theory to do Furior expantion for the function $u$. We get that

$$\begin{aligned} E(x) &= e^{-jk_{x0}x}P(x) \\ E(x) &= e^{-jk_{x0}x}\sum P_n e^{-j\frac{2n\pi}{d}x} \\ &= \sum_n P_n e^{-j(k_{x0}+\frac{2n\pi}{d})} \\ &= \sum_n P_n e^{-jk_{xn}x} \quad , \end{aligned} \tag{2.2.5}$$

where $$k_{xn} = k_{x0} + \frac{2n\pi}{d}, \qquad (2.2.6)$$

where d is periodic length of the lattice.

Based on the basic assumption of translational symmetry and aided by the Floquet (or Bloch) theorem together with the use of transfer matrix method, one can obtain a transcendental equation determining the band structure, namely [5]

$$\cos(Ka) = \cos(k_{sx}a_2)\cos(k_x a_3) - \frac{1}{2}\left(\frac{k_x}{k_{sx}} + \frac{k_{sx}}{k_x}\right)\sin(k_{sx}a_2)\sin(k_x a_3), \qquad (2.2.7)$$

where $K$ is the Bloch wave number,

$$k_x = \frac{\omega}{c}\sqrt{\varepsilon_{r3} - \sin^2\theta_1}, \qquad (2.2.8)$$

and

$$k_{sx} = \frac{\omega}{c}\sqrt{\cos^2\theta_1 - \frac{c^2}{\omega^2\lambda_L^2}}. \qquad (2.2.9)$$

Equation (2.2.7) can be numerically solved for $\omega$ as a function of $K$, yielding the so-called photonic band structure or dispersion relation.

## 2.3 Theory of annular Bragg reflectors

The structure of a SABR is shown in Fig. 1.2, in which the inner core region has a refractive index of $n_0$ and a starting radius of $\rho_0$, the layer 1 with index $n_1$ is assumed to be the superconductor, and layer 2 having index $n_2$ is the dielectric layer. In addition, the index of refraction of the outer region is denoted by $n_f$. To calculate the reflectance at the first circular boundary, $\rho = \rho_0$, we use the transfer matrix method in the cylindrical waves [11]. The cylindrical wave is assumed to be diverging from the axis of symmetry, $\rho = 0$, and then impinges normally on the first circular interface of $\rho = \rho_0$.

Assuming an $\exp(j\omega t)$ time dependence for the electromagnetic fields, the

source-free two curl Maxwell's equations are given by

$$\nabla \times E = -j\omega\mu H\,, \tag{2.3.1}$$

$$\nabla \times H = j\omega\varepsilon E\,. \tag{2.3.2}$$

In cylindrical coordinate,Eq.(2.3.1):

$$\frac{1}{\rho}\begin{vmatrix} \hat{\rho} & \rho\hat{\phi} & \hat{z} \\ \partial_\rho & \partial_\phi & \partial_z \\ E_\rho & \rho E_\phi & E_z \end{vmatrix} = -j\omega\mu(\hat{\rho}H_\rho + \hat{\phi}H_\phi + \hat{z}H_z)\,, \tag{2.3.3}$$

leading to

$$\frac{1}{\rho}\frac{\partial E_z}{\partial\phi} - \frac{\partial E_\phi}{\partial z} = -j\omega\mu H_\rho\,, \tag{2.3.4a}$$

$$\frac{\partial E_\rho}{\partial z} - \frac{\partial E_z}{\partial\rho} = -j\omega\mu H_\phi\,, \tag{2.3.4b}$$

$$\frac{1}{\rho}\left[\frac{\partial(\rho E_\phi)}{\partial\rho} - \frac{\partial E_\rho}{\partial\phi}\right] = -j\omega\mu H_z\,, \tag{2.3.4c}$$

and Eq.( 2.3.2):

$$\frac{1}{\rho}\begin{vmatrix} \hat{\rho} & \rho\hat{\phi} & \hat{z} \\ \partial_\rho & \partial_\phi & \partial_z \\ H_\rho & \rho H_\phi & H_z \end{vmatrix} = j\omega\varepsilon(\hat{\rho}E_\rho + \hat{\phi}E_\phi + \hat{z}E_z)\,, \tag{2.3.5}$$

$$\frac{1}{\rho}\frac{\partial H_z}{\partial\phi} - \frac{\partial H_\phi}{\partial z} = j\omega\varepsilon E_\rho\,, \tag{2.3.6a}$$

$$\frac{\partial H_\rho}{\partial z} - \frac{\partial H_z}{\partial\rho} = j\omega\varepsilon E_\phi\,, \tag{2.3.6b}$$

$$\frac{1}{\rho}\left[\frac{\partial(\rho H_\phi)}{\partial\rho} - \frac{\partial H_\rho}{\partial\phi}\right] = j\omega\varepsilon E_z\,. \tag{2.3.6c}$$

In the case that the propagation of cylindrical wave diverging from or converging to the axis of symmetry $\rho = 0$, the derivatives of the fields with respect to z vanish and Eq.(2.3.4) can be reduced to

$$\frac{1}{\rho}\frac{\partial E_z}{\partial \phi} = -j\omega\mu H_\rho, \qquad (2.3.7a)$$

$$\frac{\partial E_z}{\partial \rho} = j\omega\mu H_\phi, \qquad (2.3.7b)$$

$$\frac{1}{\rho}\left[\frac{\partial(\rho E_\phi)}{\partial \rho} - \frac{\partial E_\rho}{\partial \phi}\right] = -j\omega\mu H_z. \qquad (2.3.7c)$$

Eq. (2.3.6) gives in a similar way:

$$\frac{1}{\rho}\frac{\partial H_z}{\partial \phi} = j\omega\varepsilon E_\rho, \qquad (2.3.8a)$$

$$\frac{\partial H_z}{\partial \rho} = -j\omega\varepsilon E_\phi, \qquad (2.3.8b)$$

$$\frac{1}{\rho}\left[\frac{\partial(\rho H_\phi)}{\partial \rho} - \frac{\partial H_\rho}{\partial \phi}\right] = j\omega\varepsilon E_z. \qquad (2.3.8c)$$

In the circular cylindrical coordinates there are two possible modes, i.e., TE and TM modes. For TE wave, the nonzero fields, $E_z, H_\phi$, and $H_\rho$ in each single layer satisfy the three equations, Eqs. (2.3.7a), (2.3.7b) and (2.3.8c). Solutions for Eqs. (2.3.7c), (2.3.8a) and (2.3.8b) can be obtain for TM wave, which has non-zero components $H_z$ , $E_\phi$ and $E_\rho$.

In the case of TE wave, the electromagnetic field ( $E_z, H_\phi, H_\rho$ )obeys the relations:

$$H_\rho = j\frac{1}{\omega\mu}\frac{1}{\rho}\frac{\partial E_z}{\partial \phi}, \qquad (2.3.9a)$$

$$H_\phi = -j\frac{1}{\omega\mu}\frac{\partial E_z}{\partial \rho} \qquad (2.3.9b)$$

$$\frac{\partial(\rho H_\phi)}{\partial \rho} - \frac{\partial H_\rho}{\partial \phi} = j\omega\varepsilon\rho E_z. \qquad (2.3.9c)$$

Thus, Eq. (2.3.9c) becomes

$$\frac{\partial\left(-j\rho\frac{1}{\omega\mu}\frac{\partial E_z}{\partial \rho}\right)}{\partial \rho} - \frac{\partial}{\partial \phi}\left(j\frac{1}{\omega\mu}\frac{\partial E_z}{\partial \rho}\right) = j\omega\varepsilon\rho E_z. \qquad (2.3.10)$$

With Eq. (2.3.3), the governing equation for tangential electric field $E_z$ is given by

$$\rho\frac{\partial}{\partial\rho}\left(\rho\frac{\partial E_z}{\partial\rho}\right)-\rho^2\frac{1}{\mu}\frac{\partial\mu}{\partial\rho}\frac{\partial E_z}{\partial\rho}+\frac{\partial}{\partial\phi}\left(\frac{\partial E_z}{\partial\phi}\right)+\omega^2\mu\varepsilon\rho^2E_z=0. \qquad (2.3.11)$$

The solution of Eq. (2.3.11) can be obtained the method of separation of variables. Substituting $E_z(\rho,\phi)=V(\rho)\Phi(\phi)$ in Eq. (2.3.7) and using Eq. (2.3.11) we obtain:

$$\frac{1}{V}\rho\frac{\partial}{\partial\rho}\left(\rho\frac{\partial V}{\partial\rho}\right)-\frac{1}{V}\rho^2\frac{1}{\mu}\frac{\partial\mu}{\partial\rho}\frac{\partial V}{\partial\rho}+\frac{1}{\Phi}\frac{\partial^2\Phi}{\partial\phi^2}+\omega^2\mu\varepsilon\rho^2=0 \quad ,$$

(2.3.12)

$$\frac{1}{V}\rho\frac{\partial}{\partial\rho}\left(\rho\frac{\partial V}{\partial\rho}\right)-\frac{1}{V}\rho^2\frac{1}{\mu}\frac{\partial\mu}{\partial\rho}\frac{\partial V}{\partial\rho}+\omega^2\mu\varepsilon\rho^2=-\frac{1}{\Phi}\frac{\partial^2\Phi}{\partial\phi^2}=m^2. \qquad (2.3.13)$$

For the angular part:

$$\frac{\partial^2\Phi}{\partial\phi^2}+m^2\Phi=0. \qquad (2.3.14)$$

For the radial part:

$$\frac{1}{V}\rho\frac{\partial}{\partial\rho}\left(\rho\frac{\partial V}{\partial\rho}\right)-\frac{1}{V}\rho^2\frac{1}{\mu}\frac{\partial\mu}{\partial\rho}\frac{\partial V}{\partial\rho}+\omega^2\mu\varepsilon\rho^2=m^2. \qquad (2.3.15)$$

where $m$ is a positive or negative integer or zero, called the azimuthal number. Then, we obtain:

$$E_z(\rho,\phi)=V(\rho)\Phi(\phi), \qquad (2.3.16a)$$

$$H_\rho=-\frac{m}{\omega\mu}\frac{V(\rho)}{\rho}e^{jm\phi}, \qquad (2.3.16b)$$

$$H_\phi=-\frac{1}{j\omega\mu}\frac{\partial V(\rho)}{\partial\rho}e^{jm\phi}=U(\rho)e^{jm\phi}, \qquad (2.3.16c)$$

where the functions $U(\rho)$ and $V(\rho)$ obey

$$\frac{\partial V}{\partial\rho}=j\omega\mu U(\rho). \qquad (2.3.17)$$

We have

$$\rho\frac{\partial}{\partial\rho}\left(\rho\frac{\partial V}{\partial\rho}\right)+\omega^2\mu\varepsilon\rho^2V-m^2V=0. \qquad (2.3.18)$$

$$\rho\frac{\partial}{\partial\rho}\left(\rho\frac{\partial V}{\partial\rho}\right)+k^2V-m^2V=0, \qquad (2.3.19)$$

which is the Bessel's differential equation with the solution

$$V = AJ_m(k\rho) + BY_m(k\rho), \tag{2.3.20}$$

where A and B are constants, $k = \omega\sqrt{\mu\varepsilon}$ is the wave number in the layer, $J_m$ is a Bessel function, and $Y_m$ is a Neumann function.

The function $U(\rho)$ can be found from Eq.( 2.3.17) as

$$U(\rho) = \frac{k}{j\omega\mu}\left(AJ_m'(k\rho) + BY_m'(k\rho)\right), \tag{2.3.21}$$

$$U(\rho) = -jp\left(AJ_m'(k\rho) + BY_m'(k\rho)\right), \tag{2.3.22}$$

where $p = \sqrt{\varepsilon/\mu}$ is the intrinsic admittance of the layer, and the primes represent differentiation by the whole argument of the function (not just by $\rho$).

From Eqs. (2.3.16b) and (2.3.16c) we see that $V$ and $U$ determine the magnetic field components $H_\rho$ and $H_\phi$, respectively. Equations (2.3.8) and (2.3.9) enable us to construct a single layer matrix relating the electric and magnetic fields at its two interfaces. For instance, the matrix for the first layer (with refractive index $n_1$ and interfaces at $\rho = \rho_0$ and $\rho_1$) is written as [11]

$$\begin{bmatrix} V(\rho_1) \\ U(\rho_1) \end{bmatrix} = \mathbf{M}_1 \begin{bmatrix} V(\rho_0) \\ U(\rho_0) \end{bmatrix}, \tag{2.3.23}$$

The element of transfer matrix can be found by considering the relations Eqs. (2.3.20)-(2.3.23) when the vector $(V(\rho_0), U(\rho_0))$ has the special values $(1,0)$ and $(0,1)$. Solving the equation with the help of the identity

$$J_m(x)Y_m'(x) - J_m'(x)Y_m(x) = 2/\pi x, \tag{2.3.24}$$

thus the single layer matrix

$$\mathbf{M}_1 = \begin{bmatrix} m_{11} & m_{12} \\ m_{21} & m_{22} \end{bmatrix}, \tag{2.3.25}$$

has the following matrix elements

$$\begin{aligned}
m_{11} &= \frac{\pi}{2} k_1 \rho_0 \left[ Y_m'(k_1\rho_0) J_m(k_1\rho_1) - J_m'(k_1\rho_0) Y_m(k_1\rho_1) \right], \\
m_{12} &= j \frac{\pi}{2} \frac{k_1}{p_1} \rho_0 \left[ J_m(k_1\rho_0) Y_m(k_1\rho_1) - Y_m(k_1\rho_0) J_m(k_1\rho_1) \right], \\
m_{21} &= -j \frac{\pi}{2} k_1 \rho_0 p_1 \left[ Y_m'(k_1\rho_0) J_m'(k_1\rho_1) - J_m'(k_1\rho_0) Y_m'(k_1\rho_1) \right], \\
m_{22} &= \frac{\pi}{2} k_1 \rho_0 \left[ J_m(k_1\rho_0) Y_m'(k_1\rho_1) - Y_m(k_1\rho_0) J_m'(k_1\rho_1) \right],
\end{aligned} \tag{2.3.26}$$

where $p_1 = \sqrt{\varepsilon_1/\mu_1}$. Note that the determinant of the transfer matrix in both cases is given by the ratio of the initial and final radii:

$$\det\begin{pmatrix} M_{11} & M_{12} \\ M_{21} & M_{22} \end{pmatrix} = |M| = \frac{\rho_0}{\rho}. \tag{2.3.27}$$

Obviously, the matrix elements are dependent on the radii of the two interfaces. Similarly, for *i*th layer the matrix can be obtained by some simple replacements, i.e., $\rho_0 \to \rho_{i-1}$, $\rho_1 \to \rho_i$, $k_1 \to k_i = \omega\sqrt{\mu_i \varepsilon_i}$, and $p_1 \to p_i = \sqrt{\varepsilon_i/\mu_i}$. In addition, with structure being periodic, one has $\varepsilon_i = \varepsilon_1$ if $i = \text{odd}$, and $\varepsilon_i = \varepsilon_2$ if $i = \text{even}$. For an *N*-period bilayer periodic reflector we have, in total, 2*N* layers and therefore there should be 2*N* matrices in order to set up the total system matrix **M** that relates the first and final interfaces as

$$\begin{bmatrix} V(\rho_f) \\ U(\rho_f) \end{bmatrix} = \mathbf{M} \begin{bmatrix} V(\rho_0) \\ U(\rho_0) \end{bmatrix}, \tag{2.3.28}$$

where

$$\mathbf{M}=\begin{bmatrix} M_{11} & M_{12} \\ M_{21} & M_{22} \end{bmatrix}=\mathbf{M}_{2N}\cdots\mathbf{M}_{2}\mathbf{M}_{1}. \qquad (2.3.29)$$

Unlike 1DPC, the analytic expressions for the matrix elements of **M** for an annular BR cannot be obtained because the elements of each single layer matrix are functions of the radii of the two interfaces. It thus has to be numerically calculated.

Consider an outgoing wave incident on the interface between 0 and 1, which we take to have radius $\rho=\rho_0$, and propagating to the medium $f$, which extends from $\rho=\rho_f$ to $\rho=\infty$. The amplitudes of the electric field and magnetic fields at $\rho_0$ and $\rho_f$ can be written in terms of the amplitude reflection and transmission coefficients $r_d$ and $t_d$ and are related by the transfer matrix $M$ defined in Eq.(2.3.28) and subsequence discussion:

$$\begin{pmatrix} 1+r_d \\ -jp_0C_{m0}^{(2)}-jp_0C_{m0}^{(1)}t_d \end{pmatrix}=M^{-1}\begin{pmatrix} t_d \\ -jp_fC_{mf}^{(2)}t_d \end{pmatrix}, \qquad (2.3.30)$$

where

$$M^{-1}=\begin{pmatrix} M_{11} & M_{12} \\ M_{21} & M_{22} \end{pmatrix}^{-1}=\frac{1}{|M|}\begin{pmatrix} M_{22} & -M_{21} \\ -M_{12} & M_{11} \end{pmatrix}^{T}$$

$$=\frac{1}{|M|}\begin{pmatrix} M_{22} & -M_{12} \\ -M_{21} & M_{11} \end{pmatrix}\equiv\begin{pmatrix} M'_{11} & M'_{12} \\ M'_{21} & M'_{22} \end{pmatrix}. \qquad (2.3.31)$$

Equation (2.3.30) enables us to calculate the reflection and transmission coefficients for multilayered structure,

$$\begin{pmatrix} 1+r_d \\ -jp_0C_{m0}^{(2)}-jp_0C_{m0}^{(1)}t_d \end{pmatrix}=\begin{pmatrix} M'_{11} & M'_{12} \\ M'_{21} & M'_{22} \end{pmatrix}\begin{pmatrix} t_d \\ -jp_fC_{mf}^{(2)}t_d \end{pmatrix} \qquad (2.3.32)$$

$$1+r_d=\left(M'_{11}-jp_fC_{mf}^{(2)}M'_{12}\right)t_d, \qquad (2.3.33)$$

$$-jp_0C_{m0}^{(2)}-jp_0C_{m0}^{(1)}r_d=\left(M'_{21}-jp_fC_{mf}^{(2)}M'_{22}\right)t_d, \qquad (2.3.34)$$

From Eqs. (2.3.33) and (2.2.34), we can get

$$\frac{-jp_0C_{m0}^{(2)} - jp_0C_{m0}^{(1)}r_d}{1+r_d} = \frac{M'_{21} - jp_fC_{mf}^{(2)}M'_{22}}{M'_{11} - jp_fC_{mf}^{(2)}M'_{12}}. \tag{2.3.35}$$

Hence, the reflection coefficients is given by

$$r_d = \frac{\left(M'_{21} + jp_0C_{m0}^{(2)}M'_{11}\right) - jp_fC_{mf}^{(2)}\left(M'_{22} + jp_0C_{m0}^{(2)}M'_{12}\right)}{\left(-jp_0C_{m0}^{(1)}M'_{11} - M'_{21}\right) - jp_fC_{mf}^{(2)}\left(-jp_0C_{m0}^{(1)}M'_{12} - M'_{22}\right)}. \tag{2.3.36}$$

From Eqs. (2.3.33),

$$t_d = \frac{1+r_d}{M'_{11} - jp_fC_{mf}^{(2)}M'_{12}}, \tag{2.3.37}$$

where the numerator

$$\begin{aligned} 1+r_d &= 1+\frac{\left(M'_{21} + jp_0C_{m0}^{(2)}M'_{11}\right) - jp_fC_{mf}^{(2)}\left(M'_{22} + jp_0C_{m0}^{(2)}M'_{12}\right)}{\left(-jp_0C_{m0}^{(1)}M'_{11} - M'_{21}\right) - jp_fC_{mf}^{(2)}\left(-jp_0C_{m0}^{(1)}M'_{12} - M'_{22}\right)} \\ &= \frac{\left(-jp_0C_{m0}^{(1)} + jp_0C_{m0}^{(2)}\right)\left(M'_{11} - jp_fC_{mf}^{(2)}M'_{12}\right)}{\left(-jp_0C_{m0}^{(1)}M'_{11} - M'_{21}\right) - jp_fC_{mf}^{(2)}\left(-jp_0C_{m0}^{(1)}M'_{12} - M'_{22}\right)}. \end{aligned} \tag{2.3.38}$$

Thus the transmission coefficient is given by

$$t_d = \frac{4\sqrt{\varepsilon_0/\mu_0}}{\pi K\rho_0 H_m^{(2)}\left(k_0\rho_0\right)H_m^{(1)}\left(k_0\rho_0\right)\left[\left(-jp_0C_{m0}^{(1)}M'_{11} - M'_{21}\right) - jp_fC_{mf}^{(2)}\left(-jp_0C_{m0}^{(1)}M'_{12} - M'_{22}\right)\right]}, \tag{2.3.39}$$

where $M'_{11}, M'_{12}, M'_{21}$ and $M'_{22}$ are the matrix elements of the inverse matrix of **M**, $K = \omega\sqrt{\mu_0\varepsilon_0}$ is the free-space wave number, and

$$C_{ml}^{(1,2)} = \frac{H_m^{(1,2)\prime}\left(k_l\rho_l\right)}{H_m^{(1,2)}\left(k_l\rho_l\right)}, \quad l = 0, \ f. \tag{2.3.40}$$

where $H_m^{(1)}$ and $H_m^{(2)}$ are the Hankel function of the first and second kind. Equations (2.3.36) and (2.3.39) then leads to the reflectance *R* and the transmittance *T*, i.e.,

$$R = \left|r_d\right|^2, \qquad T = \frac{n_f}{n_0}\left|t_d\right|^2, \tag{2.3.41}$$

where $n_0$ and $n_f$ are respectively the refractive indices of the starting and the final

media. The results for TM wave are also obtainable by simply replacing $\varepsilon \leftrightarrow \mu$, and $j \leftrightarrow -j$ in the formulas of TE wave.

## 2.4 The two-fluid model of superconductors

In 1934, Gorter and Casimir provided the two-fluid model for the electric conduction mechanism of superconductors [12,13]. When $T > 0$ K, the two-fluid model can very successfully explain the character of superconductor device under the condition of superconductivity conduction. According to this theory, one assumes that the total electron density $n$ can be divided into two kinds of conduction electrons, one of which is normal electrons $n_n$ and another is superconducting electrons $n_s$. That is

$$n = n_n + n_s, \tag{2.4.1}$$

and they have different conductivity

$$\sigma = \sigma_n + \sigma_s, \tag{2.4.2}$$

where $\sigma_n$ is the conductivity of normal electrons, and $\sigma_s$ is the conductivity of paired superconductivity electrons. From the Drude model and London equation, we get

$$\sigma_n = n_n e^2 \tau / m(1 + j\tau\omega), \tag{2.4.3}$$

$$\sigma_s = \lim_{\tau \to \infty} \sigma_n = (\pi n_n e^2 / 2m)\delta(\omega) - j n_s e^2 / m\omega. \tag{2.4.4}$$

If the relaxation time $\tau \to \infty$, the conductivity is a complex number, so under the condition of $f \neq 0$ , we have

$$\sigma = (\frac{e^2}{m})\left[ n_n \tau \frac{1 - j\tau\omega}{1 + \tau^2\omega^2} - \frac{j n_s}{\omega} \right]. \tag{2.4.5}$$

In order to satisfy the approximation of the conductivity imaginary part, we assumed the condition is low frequency, so

$$\sigma(\omega) = (\frac{e^2}{m})\left[ n_n \tau (1 - j\tau\omega) - \frac{j n_s}{\omega} \right]. \tag{2.4.6}$$

Therefore according to the two-fluid model the electromagnetic response of a

superconductor can be described in terms of the complex conductivity, $\sigma = \sigma_1 - j\sigma_2$, where the real part, $\sigma_1$, indicating the loss**,** is contributed by the normal electrons, whereas the imaginary part, $\sigma_2$, is due to the superelectrons.

Under the low temperature condition,the imaginary part is expressed as [12,13]

$$\sigma_2 = \frac{1}{\omega\mu_0\lambda_L{}^2}, \tag{2.4.7}$$

where the temperature-dependent penetration depth is given by

$$\lambda_L = \lambda_L(T) = \frac{\lambda_0}{\sqrt{1-f(T)}}, \tag{2.4.8}$$

where the Gorter-Casimir expression for $f(T)$ is given by

$$f(T) = \left(\frac{T}{T_c}\right)^4. \tag{2.4.9}$$

We shall consider the lossless case, meaning that the real part of the complex conductivity of the superconductor can be neglected and consequently it becomes

$$\sigma = -j\sigma_2 = -j\frac{1}{\omega\mu_0\lambda_L{}^2}. \tag{2.4.10}$$

The conditions for a lossless superconductor are well described in Ref. [10,11]. With Eq. (2.4.4), the relative permittivity as well as its associated index of refraction can be obtained, namely

$$\varepsilon_{r2} = 1 - \frac{c^2}{\omega^2\lambda_L{}^2}, \tag{2.4.11}$$

and

$$n_2 = \sqrt{\varepsilon_{r2}} = \sqrt{1 - \frac{c^2}{\omega^2\lambda_L{}^2}}. \tag{2.4.12}$$

# Chapter 3
# Photonic band structure for a superconductor-dielectric superlattice

## 3.1 Introduction

It is well known that photonic crystals have photonic band gaps (PBGs) in the photonic dispersion relation. In the PBGs, optical waves with certain frequencies are not allowed to propagate through the crystal [1, 2]. The PBGs are analogous to the electronic band gaps in a solid and their physical origin can be ascribed to the Bragg diffraction in a periodic multilayer structure. A simple one-dimensional photonic crystal is, in general, made of alternating layers of material with different permittivities, forming a superlattice with infinite periods. The band structure for a dielectric-dielectric photonic crystal shows that the PBG between the first and second bands widens considerably as the difference in dielectric permittivity is increased [3]. In addition, no low-frequency band gap below the first (lowest) band can be found. In a metallic photonic made of a normal metal and a dielectric, it is however found that a low-frequency (or metallicity) gap may exist. Contrary to a PBG, this metallicity gap which does not depend on the periodicity, is of the order of the plasma frequency and thus is regarded as a modified effective plasma frequency [35-37].

On the other hand, studies of photonic crystals consisting of a superconducting material and a dielectric have also been reported recently [10-12]. The electromagnetic properties of Abrkosov vortex lattice as a photonic crystal were investigated by changing the Ginzburg-Landau parameter and static magnetic field [18]. In addition to a low-frequency band gap below the first band, they also obtained the PBGs for a

superconductor in the presence of vortices. In fact, the issue of a superconducting photonic crystal was first investigated by a group in Singapore [19,20]. They considered a one-dimensional superconductor-dielectric superlattcie. By making use of the transfer matrix method accompanied by the Bloch theorem [19], a low-frequency band gap was seen for both transversal magnetic (TM) and transversal electric (TE) modes. This band gap was found to be about one third of the threshold frequency of a bulk superconducting material. The physical information from this work for TE mode however is quite limited because only the first band is given. As for the other higher bands in addition to the possible PBGs cannot be obtained there. In other words, a full band structure for this one-dimensional superconducting photonic crystal remains unavailable thus far.

A full band structure is a basic and important means for understanding the fundamental physics about electromagnetic wave propagation characteristics in a photonic crystal. This information is not only of fundamental but also of technical use for a superconducting material. Motivated by this, in this dissertation we shall extend the work of Ref. [20]. We would like to present the full photonic band structure for TE mode in a superconductor-dielectric photonic crystal. Firstly, we use the Abeles theory for a stratified media to calculate the frequency-dependent transmittance [7]. From the transmittance spectrum, we can clearly learn the locations of all possible pass bands and stop bands. With these in hand, one is able to calculate the band structure from the transcendental equation based on the transfer matrix method together with the Bloch theorem. Then a comparison between the transmittance spectrum and full band structure will be made.

The format of this work is as follows: Section II describes the theoretical approaches to be used in the calculation. The calculated transmittance spectrum and band structure will be given in Section III. Discussion on the PGBs will also be made in Section III. A summary will be addressed in Section 4.

## 3.2 Theory

A one-dimensional nonmagnetic superconductor-dielectric photonic crystal will be modeled as a periodic superconductor-dielectric multilayer structure with a large number of periods, $N >> 1$. Such an *N*-period superlattice is shown in Fig. 3.1, where $a = a_2 + a_3$ is the spatial periodicity, where $a_2$ is the thickness of the superconducting layer and $a_3$ denotes the thickness of the dielectric layer. We consider that a TE wave is incident at an angle $\theta_1$ from the top medium which is taken to be free space with a refractive index, $n_1 = 1$. The index of refraction of the lossless dielectric is given by $n_3 = \sqrt{\varepsilon_{r3}}$, where $\varepsilon_{r3}$ is its relative permittivity. For the superconductor, the index of refraction can be described on the basis of the conventional two-fluid model [20]. According to the two-fluid model the relative permittivity as well as its associated index of refraction can be obtained, namely

$$\varepsilon_{r2} = 1 - \frac{c^2}{\omega^2 \lambda_L{}^2}, \tag{3.1}$$

and

$$n_2 = \sqrt{\varepsilon_{r2}} = \sqrt{1 - \frac{c^2}{\omega^2 \lambda_L{}^2}}. \tag{3.2}$$

According to the Abeles theory, the reflection and transmission coefficients can be determined and are given by[11]

$$\tilde{r} = \frac{\left(M_{11} + M_{12} p_\ell\right) p_1 - \left(M_{21} + M_{22} p_\ell\right)}{\left(M_{11} + M_{12} p_\ell\right) p_1 + \left(M_{21} + M_{22} p_\ell\right)}, \tag{3.3}$$

and

$$\tilde{t} = \frac{2 p_1}{\left(M_{11} + M_{12} p_\ell\right) p_1 + \left(M_{21} + M_{22} p_\ell\right)}. \tag{3.4}$$

Here $p_1 = \sqrt{\varepsilon_0 / \mu_0}\left(n_1 \cos\theta_1\right)$ is for the first medium, and $p_\ell = \sqrt{\varepsilon_0 / \mu_0}\left(n_\ell \cos\theta_\ell\right)$ is

for the last medium. Both media here are taken to be free space. The reflectance (reflectivity) *R*, transmittance (transmissivity) *T* and $\tilde{r}$, $\tilde{t}$ are related by

$$R = \left|\tilde{r}\right|^2, \qquad T = \frac{p_\ell}{p_1}\left|\tilde{t}\right|^2. \tag{3.5}$$

Next, we are going to briefly describe the method used in Ref. [20] for a direct calculation of the band structure in a periodic superconductor-dielectric medium. Based on the basic assumption of translational symmetry and aided by the Floquet (or Bloch) theorem together with the use of transfer matrix method, one can obtain a transcendental equation determining the band structure, namely [8,20]

$$\cos\left(Ka\right) = \cos\left(k_{sx}a_2\right)\cos\left(k_x a_3\right) - \frac{1}{2}\left(\frac{k_x}{k_{sx}} + \frac{k_{sx}}{k_x}\right)\sin\left(k_{sx}a_2\right)\sin\left(k_x a_3\right), \tag{3.6}$$

where *K* is the Bloch wave number,

$$k_x = \frac{\omega}{c}\sqrt{\varepsilon_{r3} - \sin^2\theta_1}, \tag{3.7}$$

and

$$k_{sx} = \frac{\omega}{c}\sqrt{\cos^2\theta_1 - \frac{c^2}{\omega^2\lambda_L^2}}. \tag{3.8}$$

Equation (3.17) can be numerically solved for $\omega$ as a function of *K*, yielding the so-called photonic band structure or dispersion relation. In Ref. [20], only the first band is given and thus it is not sufficient to explore the whole optical properties in a photonic crystal. In the next section, we shall give other possible higher bands. The higher bands then enable us to study the PGBs.

Before presenting the numerical results we mention that the above theoretical formulations are based on the flat interface model. This is legitimate and widely used to theoretically study the fundamental optical properties in a photonic crystal [3, 19, 20]. In the actual material, some interface issues such as interface roughness, lattice imperfection, and surface discontinuity may arise due to the process of a film growth. To

study surface effect on a photonic crystal, other method such as the plane-wave expansion may be employed and some works are available [38]. A study of interface effect on the photonic crystal is not our interest here.

## 3.3 Numerical Results and Discussion

### 3.3.1 Superconductor-dielectric superlattice

Let us now present the numerical results according to the aforementioned equations. Two dimensionless quantities such as $\Omega = \omega a/2\pi c$ and $\Lambda = a/2\pi\lambda_L$ will be used as usual in the analysis of photonic bands. We also define the dielectric thickness ratio as $r = a_3/a$. Figure 3.2 displays the calculated transmittance spectrum (right) and the band structure (left) for the conditions of $\theta_1 = 45^0$, $\varepsilon_{r3} = 15$, $\Lambda = 0.05$, $r = 1/3$, and $N = 500$. It is seen that the calculated transmission spectrum is in fairly good agreement with that of the calculated band structure. For the sake of convenience, the first six cutoff frequencies (at which $T = 0$) are denoted by $\Omega_i$, $i = 1, 2, 3 \sim 6$, as shown in Fig. 3.2. The first band gap, denoted by $\Delta_1$, is equal to $\Omega_1 = 0.017$. The first band gap is referred to as the low-frequency (LF) gap [20], which is not seen in the dielectric-dielectric superlattice. This gap size is nearly equal to one third of the cutoff frequency $\Omega_c$ for a bulk superconductor which is in value of 0.05 here. Thus, its origin can be regarded as a combined effect of the spatial periodicity and of the addition of dielectric material [20]. The dimensionless bulk cutoff frequency $\Omega_c = 0.05$ is equal to a real frequency of $\omega_c = c/\lambda_L \sim 10^{15}$ $s^{-1}$, which is of the same order of plasma frequency for most alkali metals. The dispersion relation for a bulk superconductor is thus recognized as an analogy to the plasma dispersion in metals.[8] On the other hand, $\Delta_1$ also appears in a metallic photonic crystal but its size is near the plasma cutoff frequency, meaning that it does not depend on the periodicity [18]. Thus in the metallic superlattice

$\Delta_1$ is not a real PBG, whereas it is a true PBG in the superconductor superlattice because $\Delta_1$ is indeed related to the periodicity.

In addition to $\Delta_1$, along with the first band from $\Omega_1 = 0.017$ to $\Omega_2 = 0.165$, other higher bands as well as PBGs are also displayed in Fig. 2. The second PBG is denoted by $\Delta_2$ equal to $\Omega_3 - \Omega_2 = 0.368 - 0.165 = 0.203$ . That is almost twelve times larger than $\Delta_1$. The second band is located from $\Omega_3 = 0.368$ to $\Omega_4 = 0.455$. The third PBG, $\Delta_3$, is $\Omega_5 - \Omega_4 = 0.712 - 0.455 = 0.257$ in magnitude and is greater than $\Delta_2$ appreciably. The third band is then above $\Omega_5$ and under $\Omega_6$. From the results in Fig. 2 we can deduce that the photonic band structure for a one-dimensional superconducting photonic crystal is quite reminscent of the electronic band structure. Moreover, it has multiple PGBs, instead of having just one lowest band gap as reported in Ref. [20].

Figure 3.3 shows the first five cutoff frequencies and PBGs as a function of penetration depth at the conditions of $\theta = 45^0$, $\varepsilon_{r3} = 15$, $r = 1/3$, and $N = 500$. The first one, $\Omega_1$, being equal to $\Delta_1$, increases with increasing $\Lambda$. The dependence of $\Delta_2$ on $\Lambda$ is similar to that of $\Delta_3$. Both also increase as $\Lambda$ increases. The variations in $\Delta_2$ and $\Delta_3$, however, are not as salinet as $\Delta_1$, especially at small values of $\Lambda$. Figure 3.4 shows the calculated frequencies and PBGs as a function of angle of incidence at $\varepsilon_{r3} = 15$, $\Lambda = 0.05$, $r = 1/3$, and $N = 500$. It is seen that gap $\Delta_1$ essentially does not change with the variation in the angle of incidence, indicating an omnidirectional feature. In addition, $\Delta_2$ changes slightly as a function of angle of incidence. The change in the third gap size, $\Delta_3$ is appreciable for $\theta_1$ smaller than $20^0$ and becomes nearly linear between $20^0$ and $60^0$. It then approaches a saturation value of about 0.32. In Fig. 3.5, we have plotted the cutoff frequencies versus dielectic constant of dielectric layer for $\theta = 45^0$, $\Lambda = 0.05$, $r = 1/3$, and $N = 500$. All the cutoff frequencies, in general, decrease with increasing dielectric constant. The corresponding first three gap sizes are

depicted in Fig. 3.6, where $\Delta_1$ decreases slowly with increasing dielectric constant. A peak vaule in $\Delta_2$ is attained for $\varepsilon_{r3}=5$, and then decreases as the dielectric constant increases. As for $\Delta_3$, it also attains a maximum when $\varepsilon_{r3}=10$, and $\Delta_3$ is equal to $\Delta_1$ for $\varepsilon_{r3}=3$.

In the above numerical results, the calculated frequency for a superconductor photonic crystal (SPC) is normalized in $1/\lambda_0$, the sole material parameter of a superconductor involved in the formulation. This indicates that the results are valid for all the possible superconductors described by the two-fluid model [20]. Most high-$T_c$ cuprates have a value of $\lambda_0 \approx 200-300$ nm, corresponding to infrared region. As for the conventional superconductor such as a typical A15 compound superconductor with $T_c$ above 10 K, $\lambda_0 \approx 60-90$ nm, it then can work in the yellow to violet region. The feasibility of a SPC has been well discussed by Feng *et al* [39].

### 3.3.2 Extraordinary optical properties in near-zero-permittivity operation range

Let us investigate the reflectance in the vicinity of superconductor threshold wavelength at various angle of incidence. To calculate the reflection response, the layer 1 is taken to be the typical high-$T_c$ superconductor, $YBa_2Cu_3O_7$ (YBCO) with $T_c$ = 92 K and $\lambda_0=140$ nm [40], and the layer 2 is MgO with $\varepsilon_{2r}=10$. The operating temperature is $T$ = 77 K in our simulation. The penetration depth $\lambda_L$ and the permittivity $\varepsilon_{1r}$ of YBCO can be calculated according to Eqs. (3.16) and (3.17). With these material parameters, the threshold wavelength of YBCO is calculated to be $\lambda_{th}$=1245 nm. In addition, the superconductor-dielectric superlattice is immersed in free space, i.e, $n_0=n_f$ =1.

We first consider the conditions of that the thicknesses of YBCO and MgO layers

are set to be $d_1 = 130$ nm and $d_2 = 80$ nm, respectively, and the number of periods is $N = 10$. Figure 3.7 depict the TM-reflectance at angle of incidence (a) $\theta = 0^0$, (b) $\theta = 15^0$, (c) $\theta = 30^0$, (d) $\theta = 45^0$ and (e) $\theta = 60^0$, respectively. It is obvious to see that at $\theta = 15^0, 30^0, 45^0$ and $60^0$ there is an additional PBG within which the threshold wavelength $\lambda_{th}$ is contained. Such a PBG is referred to as a near-zero-$n$ gap because within this gap the refractive index of superconductor is much less one and very close to zero. This gap is strongly dependent on the angle of incidence, and increases largely as the angle increases. This additional PBG however cannot be seen for the TE wave. This gap is due to the existence of radial component of the electric field, $E_\rho$. This $E_\rho$ interacts with the superelectrons in the superconductor and thus a superpolariton gap is created. Figure 3.8 shows the calculated bandedge frequencies as a function of angle of incidence at the conditions of $d_1 = 130$ nm, $d_2 = 80$ nm and the number of periods is $N = 10$. It is seen that there is an additional PBG appears near $\lambda_{th}$ in the oblique-incidence case. Except the additional PBG, the other PBG gradually disappear or appear as the angle increases. When the angle of incidence increases, this additional gap which is at $\lambda_{th}$ doesn't disappear and increases largely.

Next, we shall investigate the PBG which the threshold wavelength of YBCO, $\lambda_{th}$=1245 nm, is located within. To reach this end, the thicknesses of YBCO and MgO layers are also changed to be $d_1 = 100\,\text{mm}$ and $d_2 = 140\,\text{mm}$ and the number of periods $N = 20$ is taken in our calculation. In Fig. 3.9, we see that the threshold wavelength of YBCO $\lambda_{th}$ is located within the PBG. We can see that there are dips near $\lambda_{th}$ within the PBG at oblique incidence for TM wave. The dip in TM wave is shallower compared with the TE wave. The appearance of such dips in reflectance is mainly due to the field component $H_\rho$ of TM wave, which, in fact, does not show up in the PBR in the normal-incidence case. The deep dip in TE wave enables us to design a transmission

narrowband filter or resonator without introducing any physical defect. Moreover, a multi-resonance filter is also possible because of the presence of the multiple dips in the reflection response.

## 3.4 Summary

By using the Abeles theory for a stratified medium and two-fluid model for a superconductor, we have calculated the TE mode transmittance spectrum for a superconductor-dielectric superlattice. We have also presented the photonic band structure based on the transfer matrix method together with the Bloch theorem. Results show excellent agreement for both methods. From the calculated results, some conclusions can be drawn as follows: For a one dimensional superconducting photonic crystal, the band structure shows a multiple-PBG structure, not just the first band as shown previously in Ref. [11]. The fundamental difference is the existence of the low-frequency band gap which is not shown in all-dielectric photonic crystals. This gap is a true PBG, whereas it is not a PBG for a metallic photonic crystal. Besides the first band gap, we also have investigated the second and third PBGs as a function of penetration depth, angle of incidence, and permittivity of dielectric. The results reveal more basic information for the electromagnetic response of superconductor and it could be of technical use in superconducting electronics. Furthermore, we find that there are an additional PBG or dips appear near $\lambda_{th}$ in the oblique-incidence case.

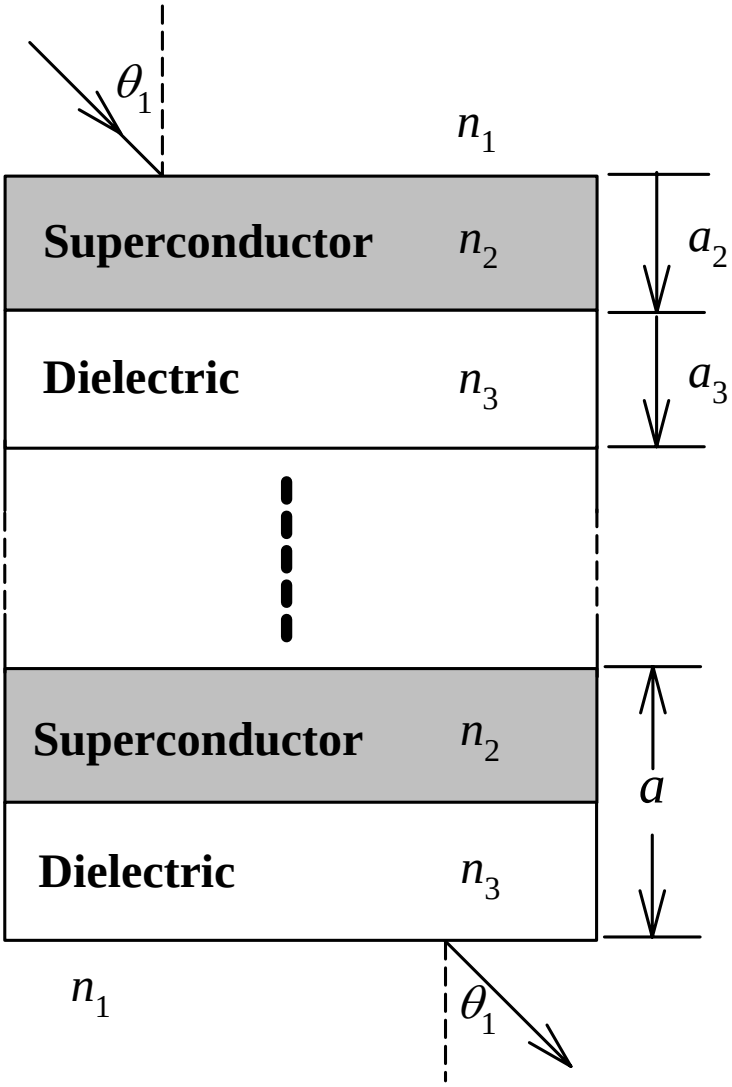


**Fig. 3.1.** A superconductor-dielectric periodic layered structure. A transversal electric mode optical wave is incident obliquely from the top medium at an angle of incidence $\theta_1$ on the plane superconductor boundary. The media are characterized by distinct indices of refraction $n_1$, $n_2$, and $n_3$, respectively. The period is *a* and the thicknesses of superconductor and dielectric layeres are denoted by $a_2$, and $a_3$, respectively.

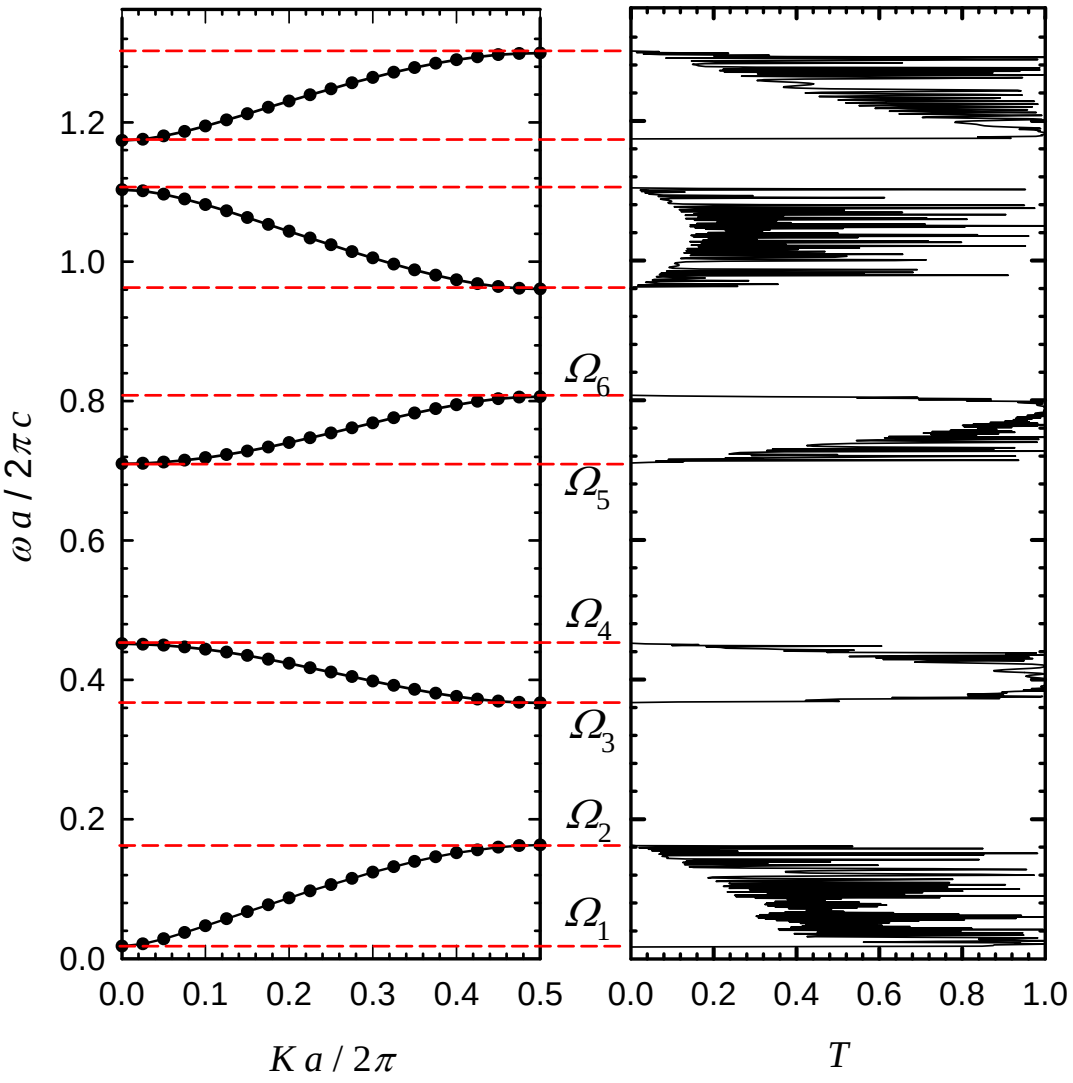


**Fig. 3.2.** The calculated transmittance spectrum (right) and the band structure (left). The horizontal dash lines mark the first six cutoff frequencies denoted by $\Omega_i$, $i = 1, 2, 3 \sim 6$. Excellent agreement is achieved in both results. The conditions are $\theta_1 = 45^0$, $\varepsilon_{r3} = 15$, $\Lambda = 0.05$, $r = 1/3$, and $N = 500$

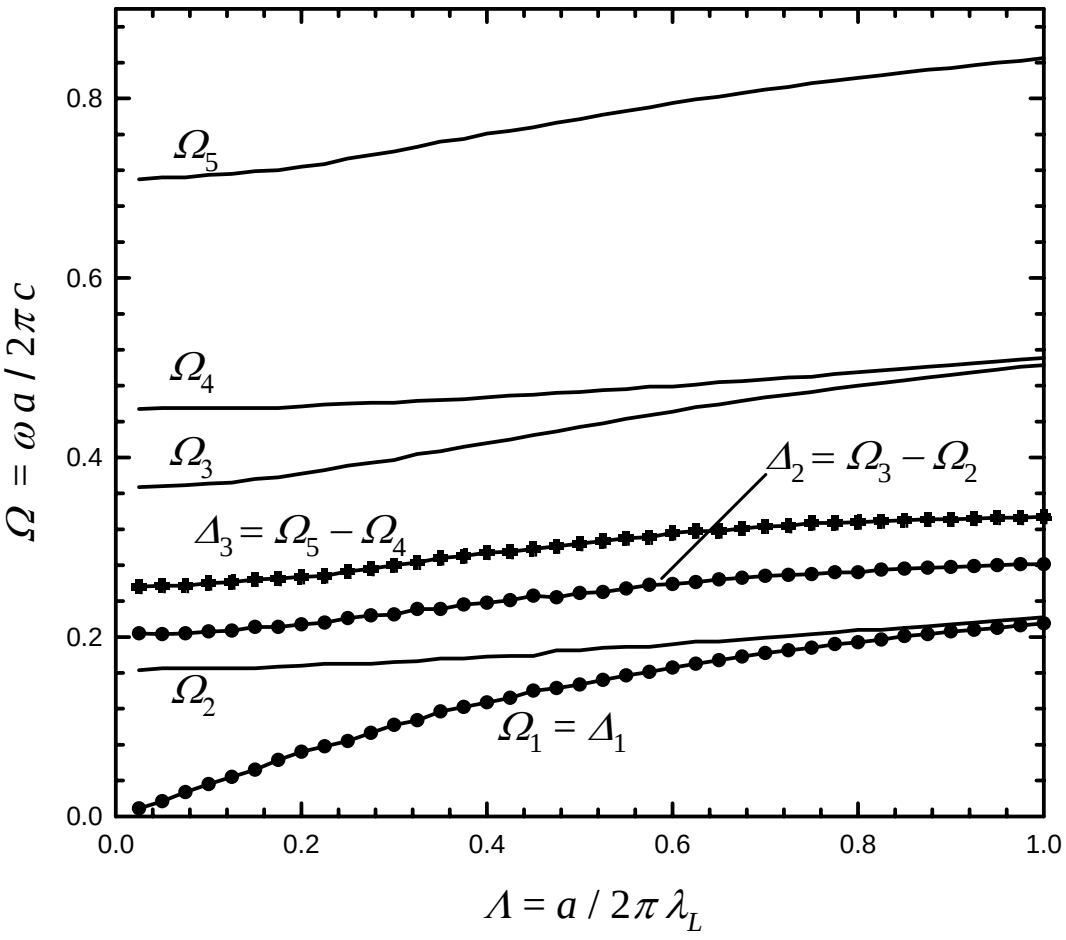


**Fig. 3.3.** Calculated five cutoff frequencies (solid lines) as well as the first three PBGs (dotted lines) as a function of penetration depth. The conditions are $\theta_1 = 45^0$, $\varepsilon_{r3} = 15$, $r = 1/3$, and $N = 500$.

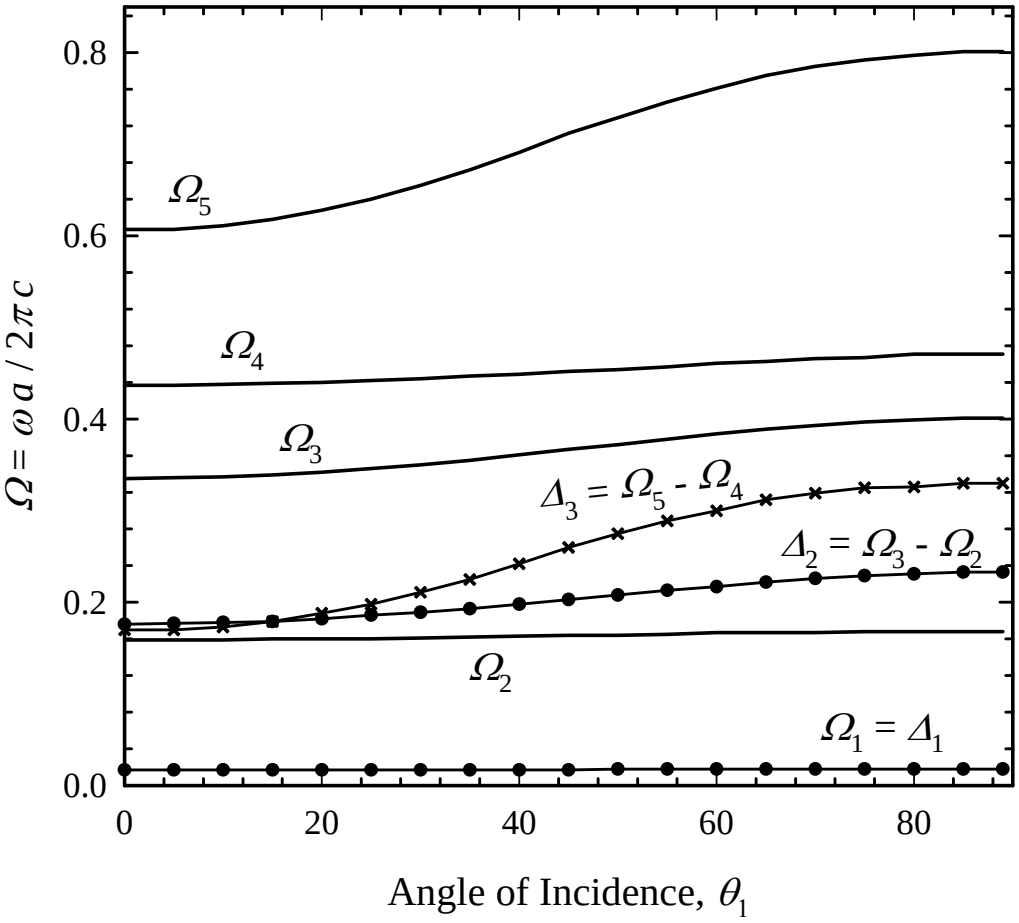


**Fig. 3.4.** Calculated five cutoff frequencies (solid lines) as well as the first three PBGs (dotted lines) as a function of angle of incidence. The conditions are $\varepsilon_{r3} = 15$, $\Lambda = 0.05$, $r = 1/3$, and $N = 500$.

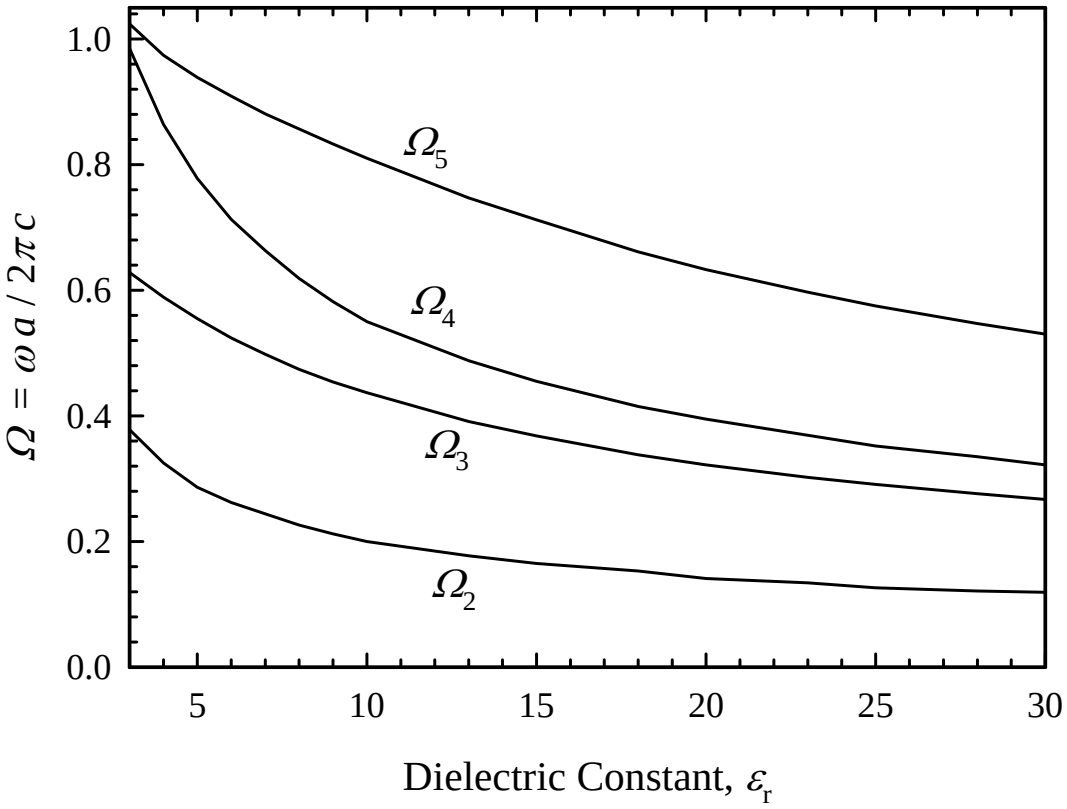


**Fig. 3.5.** Calculated four cutoff frequencies as a function of dielectric constant. The conditions are $\theta_1 = 45^0$, $\Lambda = 0.05$, $r = 1/3$, and $N = 500$.

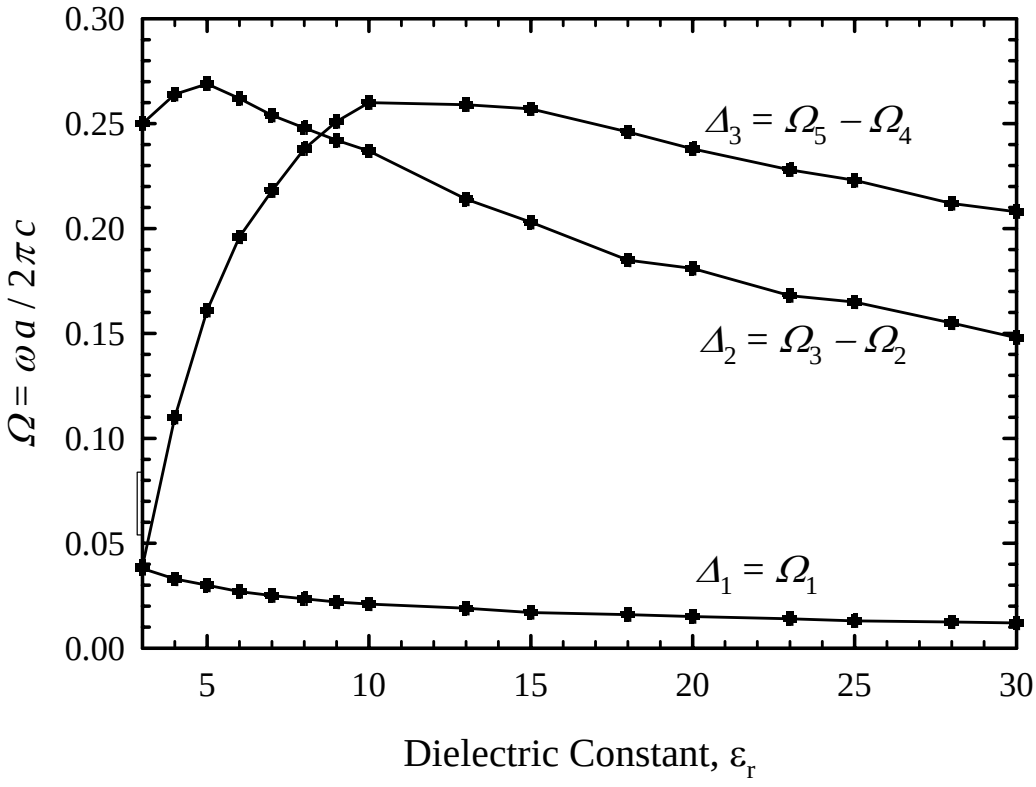


**Fig. 3.6.** The corresponding first three PBGs as a function of dielectric constant calculated from Fig. 3.5 at the same conditions.

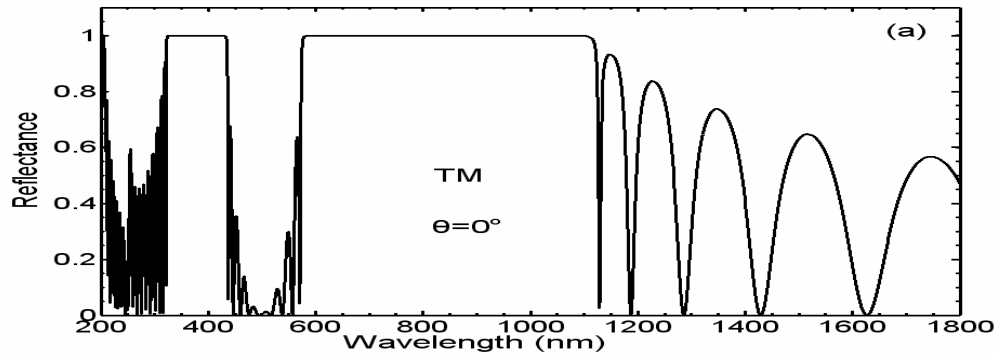
(a)
TM
θ=0°
Reflectance
Wavelength (nm)

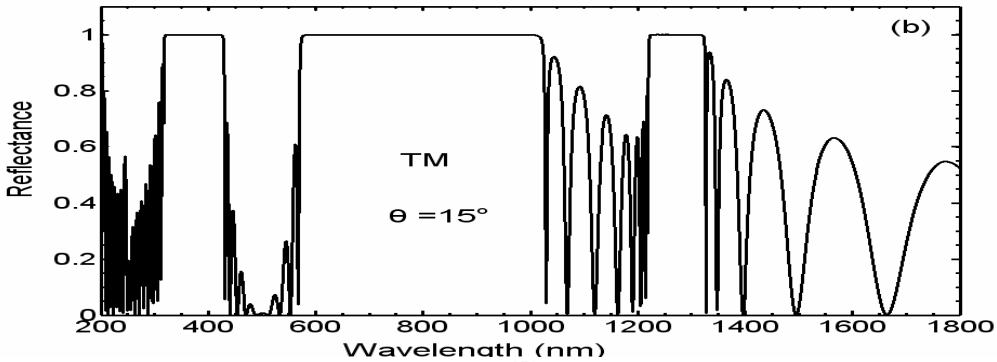
(b)
TM
θ =15°
Reflectance
Wavelength (nm)

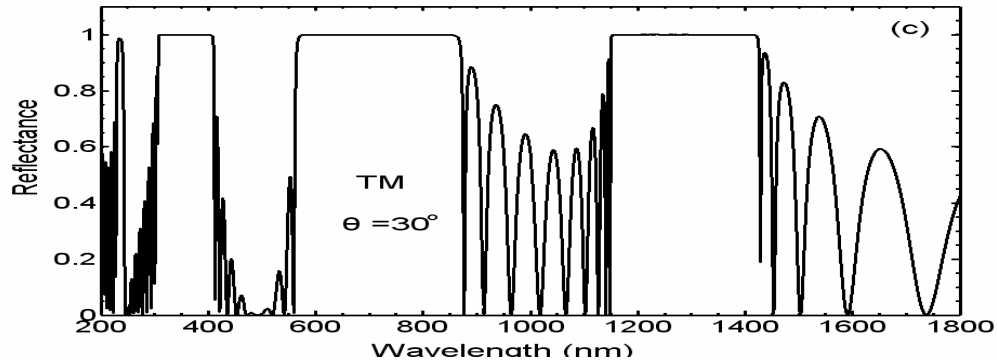
(c)
TM
θ =30°
Reflectance
Wavelength (nm)

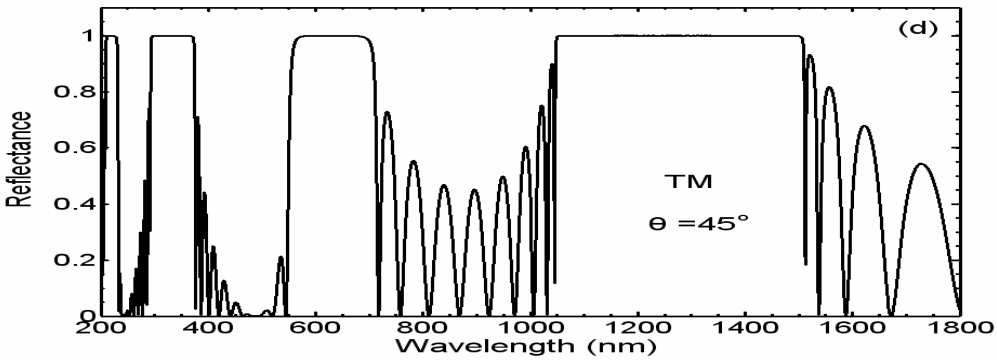
(d)
TM
θ =45°
Reflectance
Wavelength (nm)

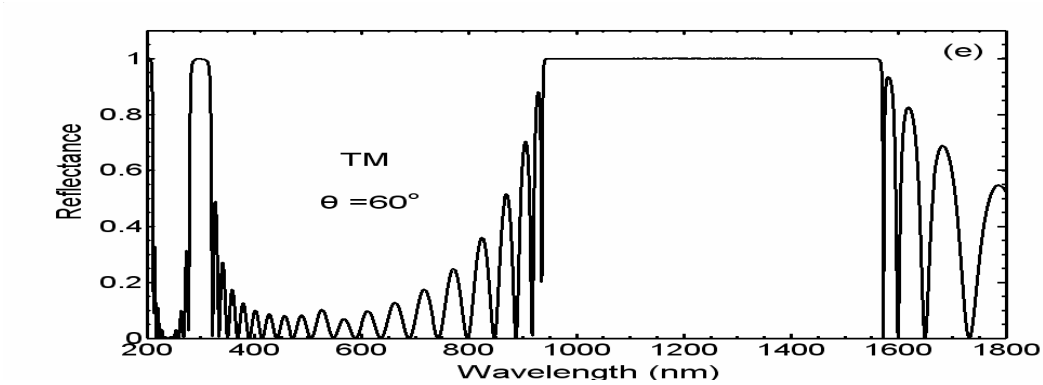


**Fig. 3.7.** Calculated TM wave reflectance spectra of a superconductor-dielectric superlattice at different incident angle (a) $\theta = 0^0$, (b) $\theta = 15^0$, (c) $\theta = 30^0$, (d) $\theta = 45^0$ and (e) $\theta = 60^0$, respectively, under the conditions of $d_1 = 130\,\text{nm}$, $d_2 = 80\,\text{nm}$ and $N = 10$.

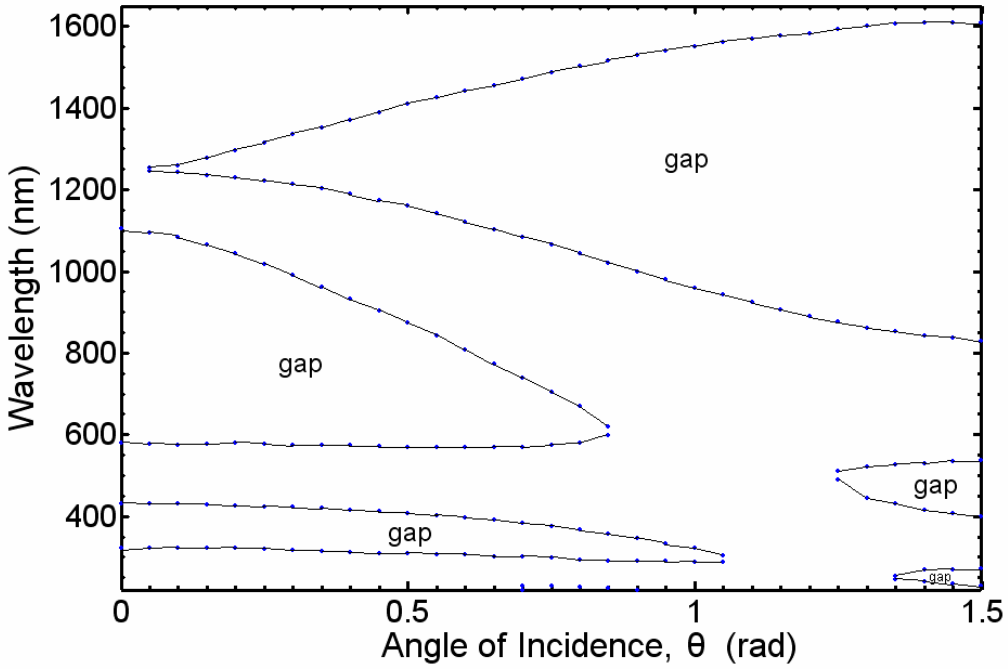


**Fig. 3.8.** Calculated bandedge frequencies as a function of angle of incidence under the conditions of $d_1 = 130$ nm, $d_2 = 80$ nm and the number of periods is $N = 10$.

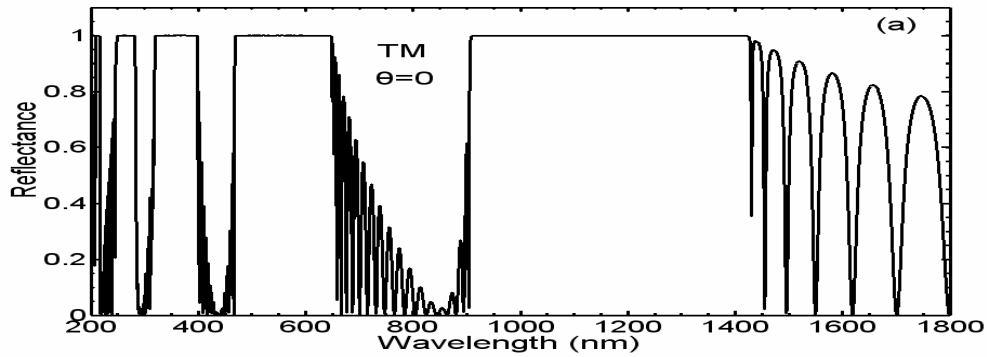
(a)
TM
θ=0
Reflectance
Wavelength (nm)

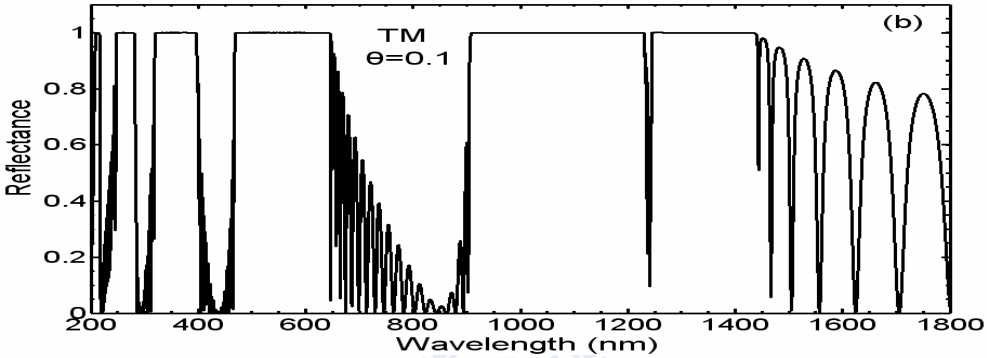
(b)
TM
θ=0.1
Reflectance
Wavelength (nm)

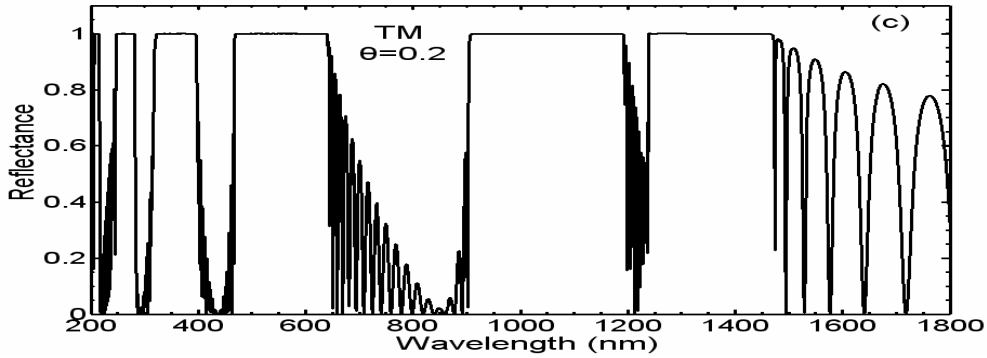
(c)
TM
θ=0.2
Reflectance
Wavelength (nm)

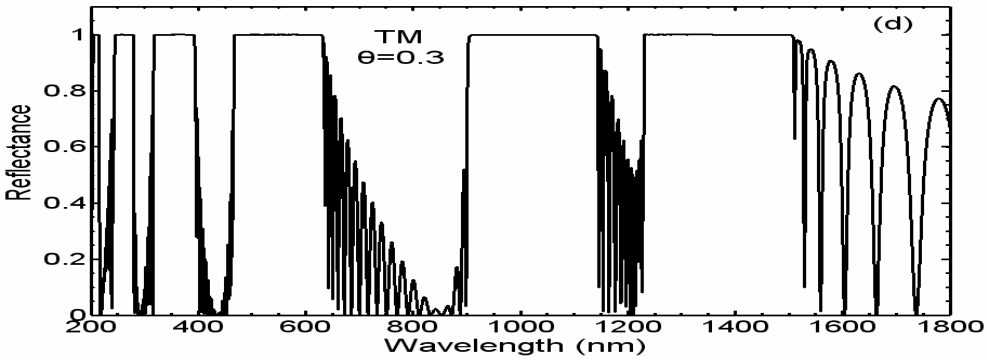
(d)
TM
θ=0.3
Reflectance
Wavelength (nm)

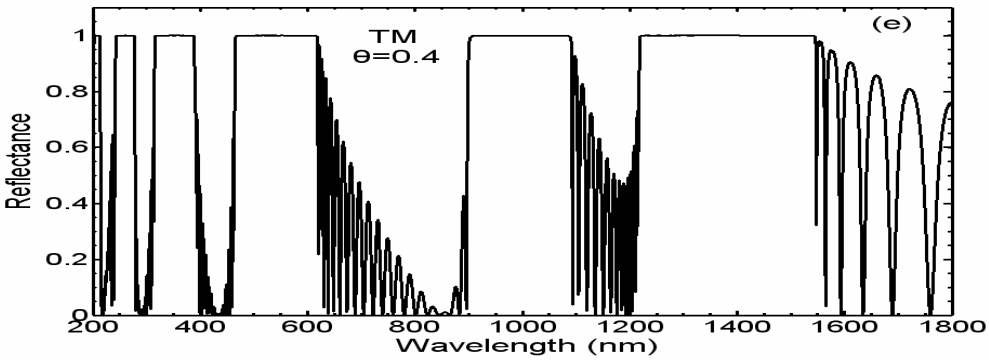
TM
θ=0.4
(e)
Reflectance
Wavelength (nm)

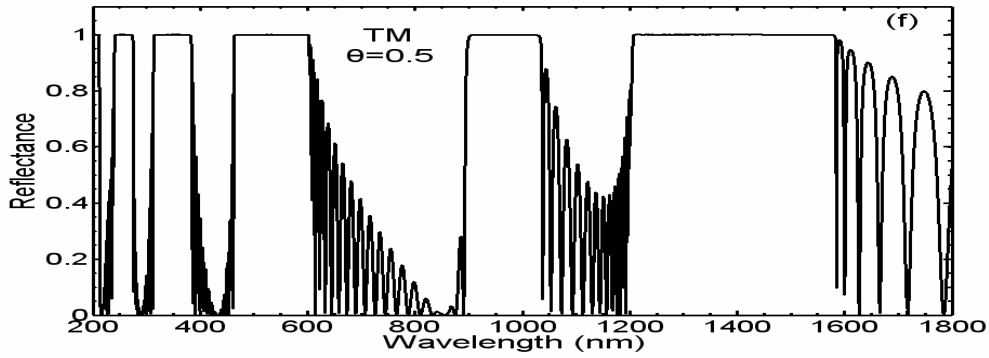
TM
θ=0.5
(f)
Reflectance
Wavelength (nm)

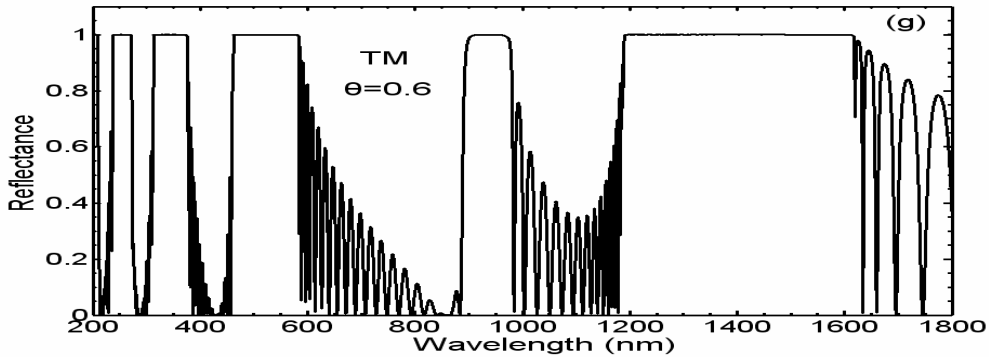
TM
θ=0.6
(g)
Reflectance
Wavelength (nm)

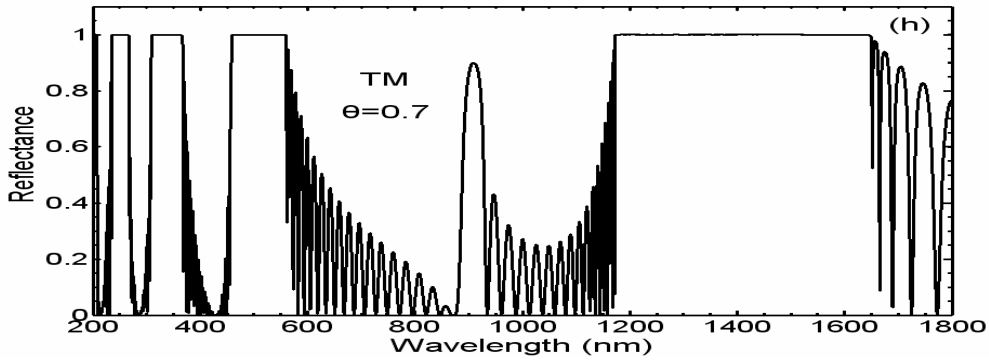
TM
θ=0.7
(h)
Reflectance
Wavelength (nm)

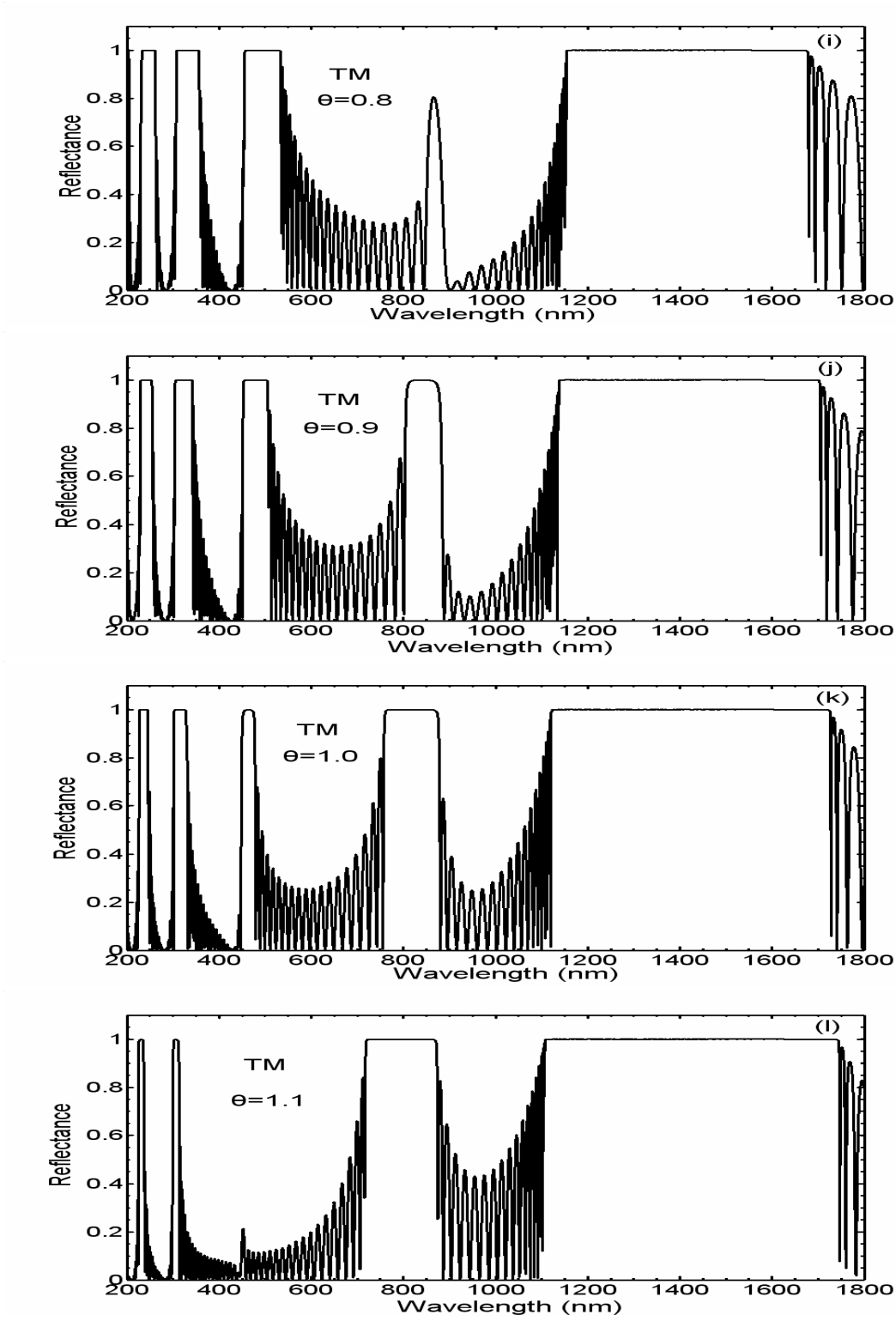


**Fig. 3.9.** Calculated TM wave reflectance spectra of a superconductor-dielectric superlattice for different incident angle (a) $\theta = 0$, (b) $\theta = 0.1$, (c) $\theta = 0.2$, (d) $\theta = 0.3$, (e) $\theta = 0.4$, (f) $\theta = 0.5$, (g) $\theta = 0.6$, (h) $\theta = 0.7$, (i) $\theta = 0.8$, (j) $\theta = 0.9$, (k) $\theta = 1.0$ and (l) $\theta = 1.1$, respectively, under the conditions of $d_1 = 100\,\text{nm}$, $d_2 = 140\,\text{nm}$ and $N = 20$.

# Chapter 4
# Optical properties of a superconducting annular periodic multilayer structure

## 4.1. Introduction

The study of a Bragg reflector (BR) or one-dimensional photonic crystal (1DPC) has been the interesting subject and has attracted lots of attention in recent years. There have been lots of reports on the calculations of the photonic band structures in 1DPCs thus far [41-43]. It is known that PCs have photonic band gaps (PBGs) at which the electromagnetic waves cannot propagate through the layered structures. Materials with PBGs have been playing an important role in modern photonic science and technology.

In the earlier stage, the PBG structures were mainly fabricated by using the usual dielectrics, semiconductors and metals as well. Recently, the studies of the photonic band structures in a periodic multilayer structure consisting of superconducting and dielectric materials have also been reported [18-21]. Such a superconducting planar Bragg reflector (SPBR) has some basic distinctions compared to an all-dielectric plane Bragg reflector. For example, there exists a low-frequency PBG due to the combined effects of periodicity and of incorporating superconducting materials [19-21]. This low-frequency PBG is further tunable as a function of the temperature and the applied static magnetic field as well. This tunable feature comes from the temperature- and field-dependent penetration length of a superconductor. Moreover, in the region near the threshold frequency of the bulk superconductor, which plays a similar role as the plasma frequency in metal, some extraordinary optical properties in a SPBR can be seen [41].

A Bragg reflector with an annular geometric structure shown in Fig. 1 has now

been achievable with the advance of modern fabrication techniques. In our analysis we use the two-fluid model for the superconductor [9,10] together with the transfer matrix method for the cylindrical waves developed by Kaliteevski *et al.* [11]. With the fact that the field solutions of the cylindrical waves are closely related to the azimuthal mode number, denoted by $m$, for both the TE and TM waves, optical properties at different *m*-number will be examined. In this paper, we have found that an additional high-reflectance band or some reflection dips near the threshold wavelength of a superconductor can be found for the TM wave at azimuthal mode number $m \geq 1$. These two distinct features behave like the localized passbands, which provide a feasible way of designing a narrowband transmission filter or an annular resonator without physically introducing any defect layer to break the periodicity of the structure. First we demonstrate that the wavelength-dependent reflectance at $m = 0$ is nearly identical to that of the planar one-dimensional superconducting BR. Second, the reflectance spectra for the TM wave are plotted and compared at different values of $m$. Finally, the role played by the starting radius $\rho_0$ in this SABR will be illustrated.

## 4.2 Theory

The structure of a SABR is shown in Fig. 4.1, in which the inner core region has a refractive index of $n_0$ and a starting radius of $\rho_0$, the layer 1 with index $n_1$ is assumed to be the superconductor, and layer 2 having index $n_2$ is the dielectric layer. In addition, the index of refraction of the outer region is denoted by $n_f$. To calculate the reflectance at the first circular boundary, $\rho = \rho_0$, we use the transfer matrix method in the cylindrical waves [11]. The cylindrical wave is assumed to be diverging from the axis of symmetry, $\rho = 0$, and then impinges normally on the first circular interface of $\rho = \rho_0$.

In our analysis we use the two-fluid model for the superconductor [12,13] together

with the transfer matrix method for the cylindrical waves developed by Kaliteevski *et al.* [8]. Unlike 1DPC, the analytic expressions for the matrix elements of **M** for an annular BR cannot be obtained because the elements of each single layer matrix are functions of the radii of the two interfaces. It thus has to be numerically calculated.

Based on the transfer matrix method for cylindrical wave described in Chapter 2, the reflection and transmission coefficients can be determined through the following relationships [11],

$$r_d = \frac{\left(M'_{21} + jp_0 C_{m0}^{(2)} M'_{11}\right) - jp_f C_{mf}^{(2)} \left(M'_{22} + jp_0 C_{m0}^{(2)} M'_{12}\right)}{\left(-jp_0 C_{m0}^{(1)} M'_{11} - M'_{21}\right) - jp_f C_{mf}^{(2)} \left(-jp_0 C_{m0}^{(1)} M'_{12} - M'_{22}\right)}, \tag{4.1}$$

$$t_d = \frac{4\sqrt{\varepsilon_0/\mu_0}}{\pi K \rho_0 H_m^{(2)}\left(k_0\rho_0\right) H_m^{(1)}\left(k_0\rho_0\right)\left[\left(-jp_0 C_{m0}^{(1)} M'_{11} - M'_{21}\right) - jp_f C_{mf}^{(2)}\left(-jp_0 C_{m0}^{(1)} M'_{12} - M'_{22}\right)\right]}, \tag{4.2}$$

where $p_0 = \sqrt{\varepsilon_0/\mu_0}$ and $p_f = \sqrt{\varepsilon_f/\mu_f}$ are the admittances of the starting and the last medium for the incident wave, $M'_{11}, M'_{12}, M'_{21}$ and $M'_{22}$ are the matrix elements of the inverse matrix of **M**, $K = \omega\sqrt{\mu_0\varepsilon_0}$ is the free-space wave number, and

$$C_{ml}^{(1,2)} = \frac{H_m^{(1,2)\prime}\left(k_l\rho_l\right)}{H_m^{(1,2)}\left(k_l\rho_l\right)}, \quad l = 0, \ f\ . \tag{4.3}$$

where $H_m^{(1)}$ and $H_m^{(2)}$ are the Hankel function of the first and second kind. The results for TM wave are also obtainable by simply replacing $\varepsilon \leftrightarrow \mu$, and $j \leftrightarrow -j$ in the formulas of TE wave.

Regarding the permittivity of the superconducting layer, we shall adopt the two-fluid model. According to the two-fluid this model the relative permittivity and the associated refractive index can be obtained and are given by

$$\varepsilon_{1r} = 1 - \frac{c^2}{\omega^2 \lambda_L^2}, \tag{4.4}$$

$$n_1 = \sqrt{\varepsilon_{1r}} = \sqrt{1 - \frac{c^2}{\omega^2 \lambda_L^2}}, \qquad (4.5)$$

It is seen, from Eq. (4.7), that there is a threshold wavelength $\lambda_{th} = 2\pi\lambda_L$ at which $n_1$ is equal to zero. The threshold frequency, or the threshold wavelength, similar to the plasma frequency in metal characterizes the electromagnetic wave properties of a bulk superconductor.

## 4.3 Numerical results and discussion

To calculate the reflection response, the layer 1 is taken to be the typical high-$T_c$ superconductor, $YBa_2Cu_3O_7$ (YBCO) with $T_c$ = 92 K and $\lambda_0 = 140$ nm [40], and the layer 2 is MgO with $\varepsilon_{2r} = 10$. The operating temperature is $T$ = 77 K in our simulation. The penetration depth $\lambda_L$ and the permittivity $\varepsilon_{1r}$ of YBCO can be calculated according to Eqs. (4.6) and (4.7). With these material parameters, the threshold wavelength of YBCO is calculated to be $\lambda_{th}$ =1245 nm. In addition, the SABR is immersed in free space, i.e, $n_0 = n_f$ =1. The thicknesses of YBCO and MgO layers are set to be $d_1 = 130$ nm and $d_2 = 80$ nm, respectively, and the number of periods is $N = 9$.

In Fig. 4.2, we plot the wavelength-dependent reflectance for both the SABR and SPBR in TE wave, where the dash curve is for SABR with $\rho_0 = 1000$ nm at the lowest mode, $m = 0$, and the solid curve is for SPBR. It is seen that both of the reflection spectra almost coincide. This indicates that means the effect of the curved interfaces in an SABR at $m = 0$ can be neglected compared to the SPBR. In addition, there are two high-reflection bands (PBGs) in Fig. 4.2. The larger bandwidth covering the range from the orange light to the near infrared has the two bandedges of 598 nm and 1059 nm (bandwidth $\Delta\lambda$ = 461 nm). The small bandwidth falling from the violet to the ultraviolet (UV) has two bandedges, 329nm and 421nm, and a bandwidth of $\Delta\lambda$ =92 nm. We can

see that the $\lambda_{th}$=1245 nm is not located within these two PBGs in this case.

Let us now investigate the reflectance at various values of *m*-number. Figure 4.3 depict the TM-reflectance at *m* = 0 (a), 1 (b), 2 (c), and 3 (d), respectively, under the conditions of $d_1 = 130\,\text{nm}$, $d_2 = 80\,\text{nm}$, $\rho_0 = 500\,\text{nm}$ and *N* = 9. It is of interest to see that at $m \geq 1$ there is an additional PBG within which the threshold wavelength is contained. Such a PBG is referred to as a near-zero-$n$ gap because within this gap the refractive index of superconductor is much less one and very close to zero. This gap is strongly dependent on the *m*-value, increasing largely as the *m*-value increases. This additional PBG however cannot be seen for the TE wave. This gap is due to the existence of radial component of the electric field, $E_\rho$. This $E_\rho$ interacts with the superelectrons in the superconductor and thus a superpolariton gap is created. It is noted that this superpolariton gap seen only for the higher order azimuthal mode of the cylindrical wave has not been found in an SPBR in the TM wave. It also should be mentioned that here we do not present the results of TE wave because, in fact, at *m* = 0, the reflectance of TE wave is nearly identical to that of TM wave. Moreover, only a little distinction in reflectance at *m* = 1, 2, or 3 is seen when they are compared to that of at *m* = 0.

In Fig. 4.4, we plot TM-reflectance spectra of the SABR at four different starting radii, 200, 700, 1200, and 2000 nm at $m = 1$. It is seen that the size of superpolariton gap is strongly affected by $\rho_0$. The size apparently decreases as $\rho_0$ increases. That is, a narrowband gap could be obtained at a larger $\rho_0$. This feature suggests that we can control the superpolariton gap size by simply changing the starting radius. However, other PBGs are not changed pronouncedly as a function of the starting radius.

Finally, we shall investigate the PBG at which the threshold wavelength of the superconductor is located within it. To reach this end, we have chosen $d_1 = 90\,\text{nm}$, $d_2 = 160\,\text{nm}$, and $\rho_0 = 1000\,\text{nm}$, and the TM-reflectance is plotted in Fig. 4.5. It is seen from Fig. 5(a) that the threshold wavelength $\lambda_{th}$= 1245 nm is indeed falls within the

PBG at $m$ = 0. It is of interest to observe that, at $m \geq 1$, a sharp dip is seen in the vicinity of $\lambda_{th}$, as shown in Fig. 5(b) - 5(d). In addition to the enhancement of the dip due to the higher mode number, the number of dips is also increased. This phenomenon only due to the higher order azimuthal mode of the cylindrical wave is not present in the SPBR in the normal incidence case, but similar dip(s) can be found in the oblique incidence in the TM wave [41]. The existence of such dips possibly enables us to design a circular transmission narrowband filter or resonator without introducing any physical defect. Moreover, a multi-resonance filter is also possible because of the presence of the multiple resonant dips. All these peculiar features are, in fact, not observed in a usual all-dielectric annular BR.

## 4.4 Summary

The photonic band structures of an SABR have been analyzed in this paper. At $m = 0$, the reflectance characteristics of an SABR is similar to that of an SPBR. At $m \geq 1$, we find that there is an additional PBG called the superpolariton gap only for the TM wave. We also find that there exist some dips when the wavelength of interest is near the threshold wavelength $\lambda_{th}$ of a superconductor. Both these results are closely related to the higher order azimuthal mode of the cylindrical wave in an SABR, which are has not be seen in the SPBR. These special features make the SABR possible to be used to design a narrowband transmission filter without inserting any physical defect layer in the structure.

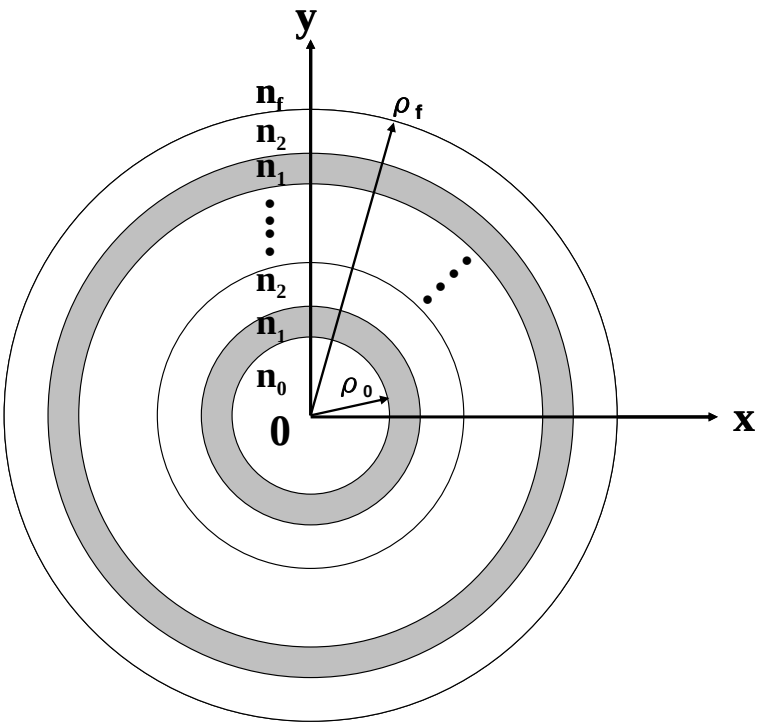


**Fig. 4.1.** The top view of the ABR, where layer 1 and layer 2 are taken to be with indices $n_1$ and $n_2$ , respectively. The thicknesses of layer 1 and layer 2 are $d_1$ and $d_2$, and $\rho_0$ is the starting radius.

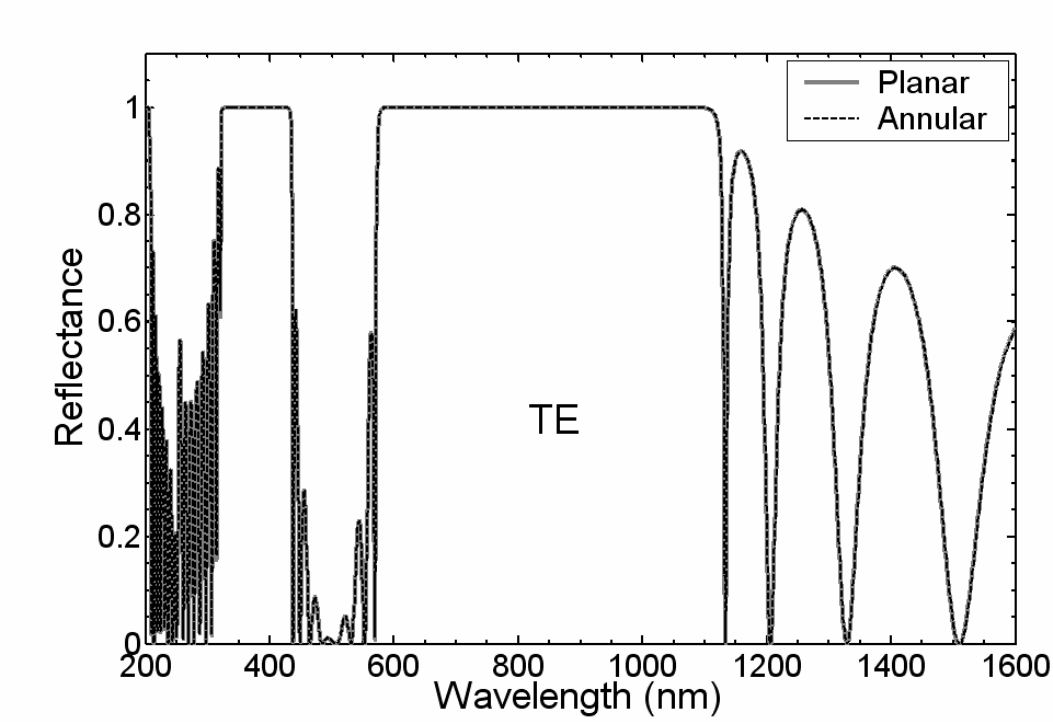


**Fig. 4.2.** Calculated wavelength-dependent reflectance for YBCO/MgO BRs., where the solid curve is for the planar superconducting BR, and the dashed curve is for the SABR.

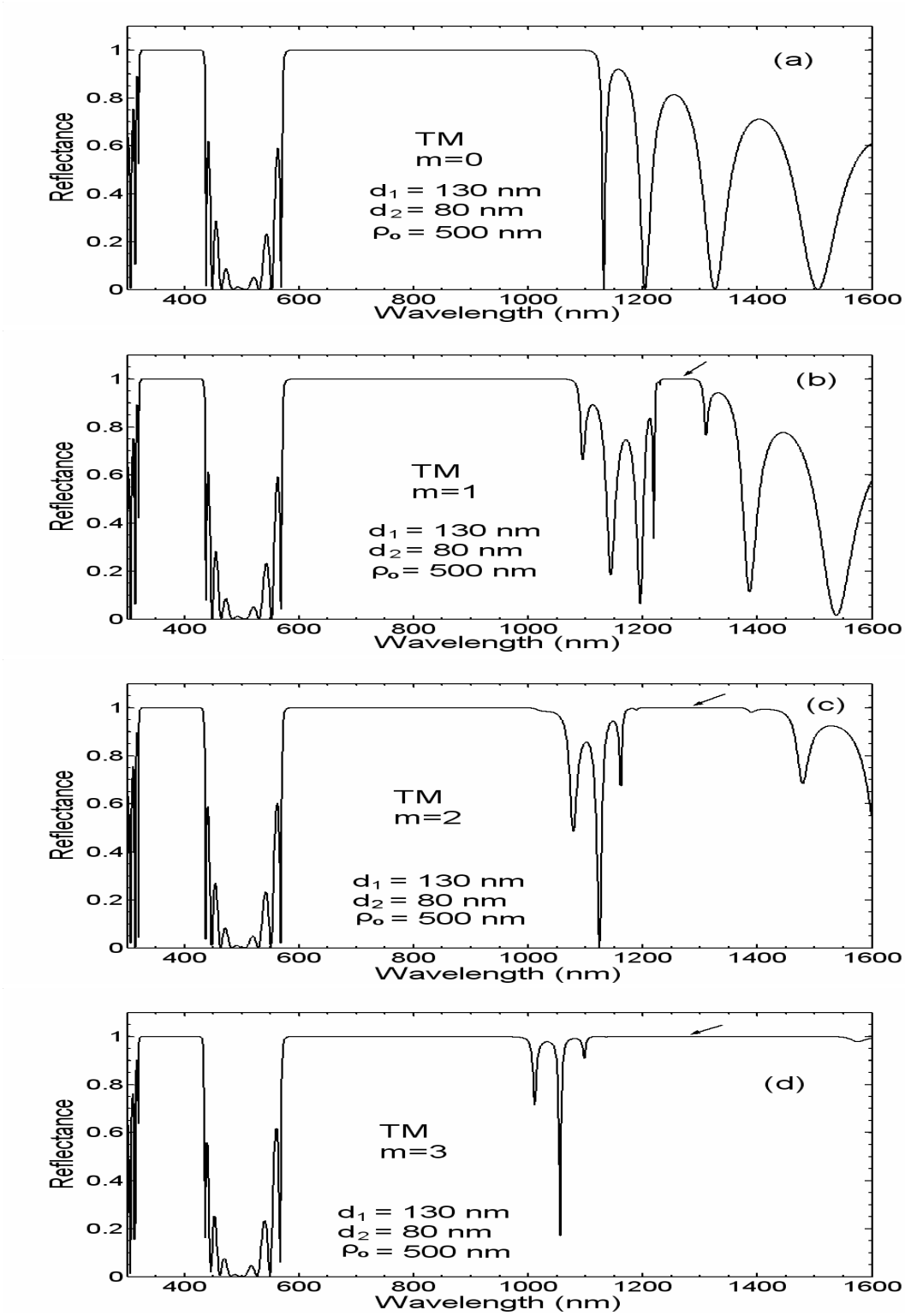


**Fig. 4.3.** Calculated reflectance spectra of TM wave at different azimuthal mode number, (a) $m = 0$, (b) $m = 1$, (c) $m = 2$ and (d) $m = 3$, respectively, under the conditions of $d_1 = 130\,\text{nm}$, $d_2 = 80\,\text{nm}$, $\rho_0 = 500\,\text{nm}$ and $N = 9$.

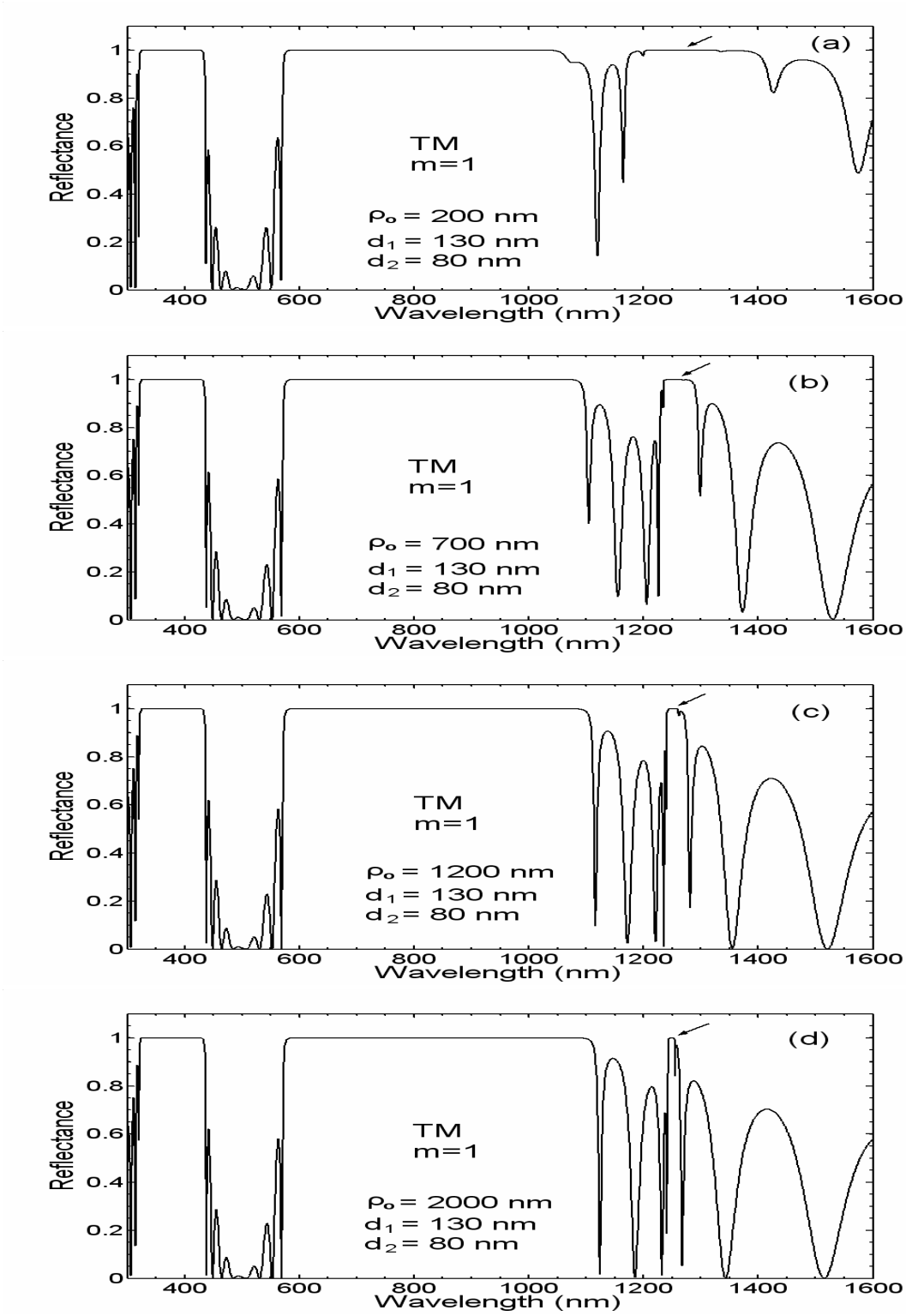


**Fig. 4.4.** Calculated reflectance spectra of TM wave at $m=1$ for different starting radii (a) $\rho_0 = 200$ nm, (b) $\rho_0 = 700$ nm, (c) $\rho_0 = 1200$ nm and (d) $\rho_0 = 2000$ nm, respectively, under the conditions of $d_1 = 130\,\text{nm}$, $d_2 = 80\,\text{nm}$ and $N = 9$.

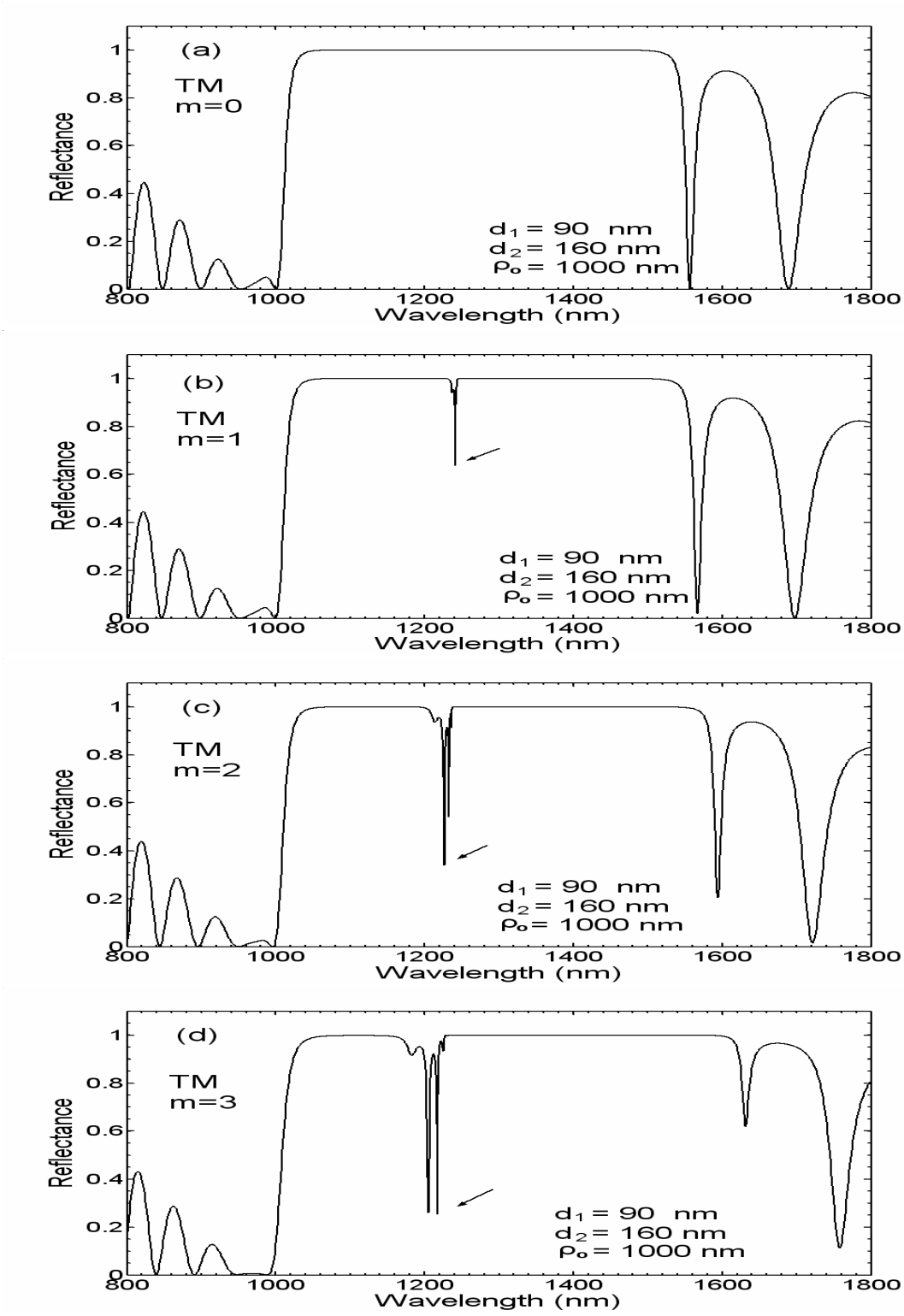


**Fig. 4.5.** Calculated reflectance spectra of TM wave for different azimuthal mode number (a) $m = 0$, (b) $m = 1$, (c) $m = 2$ and (d) $m = 3$, respectively, under the conditions of $d_1 = 90\,\text{nm}$, $d_2 = 160\,\text{nm}$, $\rho_0 = 1000\,\text{nm}$ and $N = 9$.

# Chapter 5
# Optical properties of an annular periodic multilayer structure containing the single-negative materials

## 5.1. Introduction

In 1968, the electromagnetic metamaterials with both the negative permittivity $(\varepsilon < 0)$ and negative permeability $(\mu < 0)$ first predicted by Veselago [23] are called the double-negative (DNG) materials. An SNG material means that only one of the two material parameters, $\varepsilon$ and $\mu$, is negative [31-33]. Thus an SNG material could be the epsilon-negative (ENG) medium with $\varepsilon < 0$ and $\mu > 0$ or the mu-negative (MNG) medium with $\mu < 0$ and $\varepsilon > 0$. It is known that a photonic band gap (PBG) could be formed as a consequence of the interference of Bragg scattering in a periodical layer structure like a one-dimensional photonic crystals (1DPCs) and Bragg reflectors (1DBRs). In a usual 1DBR made of all positive-index materials, the PBG is called the Bragg gap, which is proven to be strongly dependent on the lattice constant and the disorder of a device as well. However, for the SNG materials $\varepsilon$ and $\mu$ are frequency-dependent, so that we have $\varepsilon < 0$ and $\mu > 0$ or $\mu < 0$ and $\varepsilon > 0$ within a certain frequency range, which is called the SNG frequency range. Therefore, the PBG in the SNG frequency range is called the SNG gap. For a 1DBR consisting of ENG-MNG bilayers, it is known that the SNG gap is fundamentally different from the Bragg gap. There have been many reports on the 1D plane BRs (1DPBRs) containing SNG materials [42-45].

Besides the simple 1DPBRs or 1DPC, two-dimensional BRs (2DBRs) are also

important in the photonic and physical communities. A similar version 2DBR is a periodic bilayer structure in an annular geometry called an annular Bragg reflector (ABR). An ABR plays an important and useful role in modern laser system with a feature of vertical emission [9]. Similar device like the annular Bragg resonator is also available in the present [10].

In this paper, based on the transfer matrix method for the cylindrical Bragg waves developed by Kaliteevski *et al*. [11], we shall theoretically investigate the optical properties in an ABR consisting of the MNG-ENG materials. With the fact that the field solutions of the cylindrical Bragg waves for both TE and TM waves are dependent on the azimuthal mode number denoted by $m$, optical reflectance will be studied at different *m*-number. The frequency-dependent reflectance at $m = 0$ is first shown to be nearly identical to that of 1DPBR containing the SNG materials. Next, the reflectance spectra are plotted and compared at different values of $m$. At $m \geq 1$, it is found that there exist some novelties compared with the usual PBR. Furthermore, we insert a defect layer in the periodic multilayers and conclude the property of the SNG gap for an ABR is insensitive to the disorder as same as the one-dimensional BR.

## 5.2 Theory

We first introduce an ABR consisting of the MNG/ENG double layers. The relative permittivity and permeability for a MNG material are given by [42, 43]

$$\varepsilon_m = a, \quad \mu_m = 1 - \frac{\omega_{mp}^2}{\omega^2}, \tag{5.1}$$

whereas those of an ENG material are

$$\varepsilon_e = 1 - \frac{\omega_{ep}^2}{\omega^2}, \quad \mu_e = b, \tag{5.2}$$

where $a$ and $b$ are positive constants, and $\omega_{mp}$ and $\omega_{ep}$ are the magnetic plasma

frequency and the electronic plasma frequency respectively. It is seen from Eqs. (5.1) and (5.2) that the SNG frequency range exist when the frequency satisfies $\omega < \min\left\{\omega_{mp}, \omega_{ep}\right\}$ whereas the materials will be double-positive (DPS) if $\omega > \max\left\{\omega_{mp}, \omega_{ep}\right\}$.

The top view of the ABR is depicted in Fig. 4.1, where $\rho_0$ is called the starting radius, $n_1$-layer is the MNG material, and $n_2$-layer is the ENG material. The cylindrical wave is assumed to be radiated from the axis of symmetry, $\rho = 0$, and to be incident normally on the first interface at $\rho = \rho_0$. The reflectance at $\rho = \rho_0$ can be analytically analyzed by making use of the transfer matrix method in cylindrical Bragg wave [11]. There are two possible polarizations for the cylindrical Bragg wave, i.e., *E*-polarization (TE) and the *H*-polarization (TM).

Based on the transfer matrix method for cylindrical wave described in Chapter 2, the matrix elements of the inverse of **M** denoted by $M'_{11}, M'_{12}, M'_{21}$ and $M'_{22}$ can be readily obtained and then the reflection and transmission coefficients are determined by the following equations [11],

$$r_d = \frac{\left(M'_{21} + jp_0 C_{m0}^{(2)} M'_{11}\right) - jp_f C_{mf}^{(2)}\left(M'_{22} + jp_0 C_{m0}^{(2)} M'_{12}\right)}{\left(-jp_0 C_{m0}^{(1)} M'_{11} - M'_{21}\right) - jp_f C_{mf}^{(2)}\left(-jp_0 C_{m0}^{(1)} M'_{12} - M'_{22}\right)}, \tag{5.3}$$

$$t_d = \frac{4\sqrt{\varepsilon_0/\mu_0}}{\pi K \rho_0 H_m^{(2)}\left(k_0\rho_0\right) H_m^{(1)}\left(k_0\rho_0\right)\left[\left(-jp_0 C_{m0}^{(1)} M'_{11} - M'_{21}\right) - jp_f C_{mf}^{(2)}\left(-jp_0 C_{m0}^{(1)} M'_{12} - M'_{22}\right)\right]}, \tag{5.4}$$

where $p_0 = \sqrt{\varepsilon_0/\mu_0}$ and $p_f = \sqrt{\varepsilon_f/\mu_f}$ are the admittances of the starting and the last medium for the incident wave, $K = \omega\sqrt{\mu_0\varepsilon_0}$ is the free-space wave number, and

$$C_{ml}^{(1,2)} = \frac{H_m^{(1,2)\prime}\left(k_l\rho_l\right)}{H_m^{(1,2)}\left(k_l\rho_l\right)}, \quad l = 0, \ f\,. \tag{5.5}$$

where $H_m^{(1)}$ and $H_m^{(2)}$ are the Hankel function of the first and second kind. Equations (5.3) and (5.4) then leads to the reflectance *R* and the transmittance *T*, i.e.,

$$R = |r_d|^2, \qquad T = \frac{n_f}{n_0}|t_d|^2, \tag{5.6}$$

where $n_0$ and $n_f$ are respectively the refractive indices of the starting and the final media. By simply replacing $\varepsilon \leftrightarrow \mu$, and $j \leftrightarrow -j$ in the above formulations, the corresponding results for the TM wave can be readily obtained.

In the above formulations, we have considered that the input signal is an outgoing cylindrical wave that is uniformly radiated at $\rho = 0$ and impinges normally on $\rho = \rho_0$. Our goal is to calculate the reflectance at one point on $\rho = \rho_0$. However, there should be a reflected wave at the opposite end to this point and it can be regarded as the secondary input signal for the considered point. This secondary signal has been assumed to be neglected for the convenience of formulation. Technically, this secondary source can be eliminated by placing a receiving antenna or a metallic absorber at $\rho = 0$. And the above formulations are thus acceptable and reasonable.

## 5.3 Numerical results and discussion

In what follows we will present the numerical results for the optical reflectance. We suppose that the ABR is immersed in free space, i.e, $n_0 = n_f = 1$. The SNG material parameters are $a = 3.5$, $b = 1.2$, $\omega_{mp} = 10^{10}$ rad/s , and $\omega_{ep} = 1.3\times10^{10}$ rad/s [43]. This indicates that the SNG frequency range exist under the condition of $\omega < 10^{10}$ rad/s. The thicknesses of the MNG and ENG layers are $d_1 = 10$ mm and $d_2 = 5$ mm, and the number of the periods is $N = 21$.

We first investigate the geometric effect on the reflection response for both the ABR and PBR. In Fig. 5.1, we plot the frequency-dependent TE-reflectance, where the dashed curve is for ABR with $\rho_0 = 28$ mm at the lowest azimuthal mode, $m = 0$, and the gray solid curve is for PBR. It is seen that that both of the reflection spectra almost

coincide, indicating that at $m = 0$ the geometric difference due to the curved interfaces in ABR nearly has no effect on the reflectance compared to the PBR. In addition, there are two high-reflection band gaps. The narrow one at frequency lower than $10^{10}$ rad/s is referred to as the SNG gap. The wide band gap at frequency higher than $3\times10^{10}$ rad/s with DPS materials is the usual Bragg gap (BG). The fundamental features between SNG gap and BG are well described in Refs. [42-47].

Because the optical properties at $m = 0$ for an ABR is nearly the same as the usual PBR, we thus study the effects due to field solutions at the higher modes. The TE-reflectance for $m$ = 0 (a), 1 (b), 2 (c), and 3 (d) are plotted in Figs. 5.2, where $\rho_0 = 30\,\text{mm}$ is used. It is of interest to find that at $m \geq 1$ an additional PBG appear near $\omega_{mp} = 10^{10}$ rad/s. Such a PBG is referred to as the near-zero-*n* gap for the MNG material, because within this gap the refractive index of the MNG material is much less one and very close to zero, and this additional PBG is referred to as the MNG gap or the magnetic gap. The MNG gap is enhanced as $m$ increases. At $m$ = 2, this additional gap wider than $m$ = 1, is not pure SNG gap but a mixed gap of SNG and MNG gap. At $m$ = 3, a wider flat top mixed gap is obtained, as shown in Fig. 3(d). In Fig. 5.3, we plot the TM-reflectance for $m$ = 0 (a), 1 (b), 2 (c), and 3 (d) at $\rho_0 = 30\,\text{mm}$. Similar results in Fig. 3 can also be obtained for the TM wave. Here an additional gap is now near $\omega_{ep} = 1.3\times10^{10}$ rad/s, and the additional PBG can be called the ENG gap or the electric gap. This ENG gap will interact with SNG gap considerably at $m > 1$ and then again merges as wider PBG in Fig. 4(d). The results illustrate the effects of the higher-mode cylindrical Bragg wave. In addition, the values in the plasma frequencies, $\omega_{mp}$ and $\omega_{ep}$, will determine the position of the additional MNG or ENG gap. It is evident that MNG gap is due to the existence of radial component of the magnetic field $H_\rho$ of TE wave, and ENG gap is caused by $E_\rho$

of TM wave. Moreover, the higher-order mode causes a strong interaction between the MNG (or ENG) gap and SNG gap, leading to a wider mixed gap. These special results arising from the higher order azimuthal mode of the cylindrical waves are not found in the usual PBR containing of SNG materials. The additional MNG and ENG gap suggest that the ABR could be used to design a narrowband transmission filter or an annular resonator without introducing any physical defect layer in the structure.

In Figs. 5.4 and 5.5, we plot TM-reflectance spectra of the ABR for three different starting radii at $m=1$ and $m=2$, respectively. (The reflectance spectra of TM wave for $\rho_0 = 30\,\text{mm}$ at both $m=1$ and $m=2$ are shown in Fig. 4.) It is seen that the side lobes near the upper bandedge of SNG gap are highly enhanced as the starting radius decreases. Thus, the gap near $10^{10}$ rad/s is effectively enlarged at $\rho_0$ = 5 mm. The results suggest that care therefore should be taken in the choice of the starting radius for designing an ABR.

Next, we shall investigate the PBG which the magnetic plasma frequency $\omega_{mp}$ and the electronic plasma frequency $\omega_{ep}$ are located within. To reach this end, the SNG material parameters are chosen as $a=6$, $b=2.5$, $\omega_{mp}=4\times10^{10}$ rad/s, and $\omega_{ep}=4.5\times10^{10}$ rad/s [29,32] and the thicknesses of MNG and ENG layers are also changed to be $d_1=6\,\text{mm}$, $d_2=3\,\text{mm}$. The starting radius, $\rho_0=22\,\text{mm}$ and number of periods $N=6$, are taken in our calculation. In Fig.5.6 and Fig. 5.7, we see that $\omega_{mp}$ and $\omega_{ep}$ are located within the PBG. Some features are to be noted. There are dips near $\omega_{mp}$ within the PBG at mode $m\geq1$ for TE wave, whereas dips appearing near $\omega_{ep}$ in the PBG for TM wave. The dip in TM wave is shallower compared with the TE wave. The appearance of such dips in reflectance is mainly due to the higher azimuthal mode of the

cylindrical wave, which, in fact, does not show up in the PBR in the normal-incidence case. In addition, these dips in the PBG are related to the field component $H_\rho$ of TE wave and $E_\rho$ of TM wave, respectively. The deep dip in TE wave enables us to design a circular transmission narrowband filter or resonator without introducing any physical defect. Moreover, a multi-resonance filter is also possible because of the presence of the multiple dips in the reflection response.

It should be noted that the SNG material parameters and the film thicknesses in plotting Figs. 7 and 8 are different from in Figs. 2-6. We use these because the SNG gap is insensitive to the lattice constant and the SNG gap midfrequency is invariant of the ratio of the thickness (see Ref. [43]), it is thus difficult to change the position of the SNG gap in the spectra. In Figs. 2-6, the magnetic plasma frequency $\omega_{mp}$ and the electronic plasma frequency $\omega_{ep}$ are very close to the SNG gap. If we only change the film thicknesses but use the same values of the plasma frequencies as in Figs. 2-6 to achieve the condition that the plasma frequencies are located within the PBG, this PBG will approach to the SNG gap, which may lead to a confusion in the dips as well as the band edges. Moreover, the PBG may even overlap the SNG gap, which also makes the condition more complicated.

The thickness-dependent band structure in plotted in Fig. 5.8, where we take a fixed thickness ratio of the two constituent layers with different lattice constants. It is seen that SNG gap is nearly invariant for a fixed thickness ratio, robust to the variation in the lattice constant. However, the Bragg gap is strongly affected by the variation in the lattice constant. That is, the change in the lattice constant leads to a shift in the Bragg gap. In addition, the gap is enhanced as the lattice constant is decreased. These features in SNG and Bragg gaps are also seen in the usual SNG PBR. Conclusively, the fundamental

optical properties are proven to be preserved even in the ABR where the boundaries are geometrically changed from the planar shape to the annular one.

Finally, let us consider ABR containing a defect layer D with $\varepsilon_d = 1.8$, $\mu_d = 1.8$ and $d_d = 45\,\text{mm}$. The structure is denoted as $(MNG/ENG)^6 D(MNG/ENG)^6$. Here we take the material parameters of MNG and ENG as $a = 1.5$, $b = 1.5$, $\omega_{mp} = 10^{10}\,\text{rad/s}$, and $\omega_{ep} = 10^{10}\,\text{rad/s}$. For convenience of comparison, the reflectance of ABR without defect is first plotted in Fig. 5.9(a). The reflectance in the presence of the defect is then shown in Fig. 5.9(b), in which two different magnitudes of thickness, $d_1 = 24$ mm, $d_2 = 12$ mm (gray solid curve), and $d_1 = 16\,\text{mm}$, $d_2 = 8\,\text{mm}$ (dash-dotted curve) are taken, and the starting radius $\rho_0 = 30\,\text{mm}$ is used as well. When the lattice constant is scaled down by 2/3, the Bragg gap in the presence of the defect is obviously moved to the higher frequency, while it remains fixed for the SNG gap. The result again elucidates that the SNG gap is indeed robust to the lattice constant (with a fixed thickness ratio of the constituent bilayer) even in the ABR. It is also contrasted with the Bragg gap that the spectral position of the defect mode inside the SNG gap is nearly invariant with the lattice constant scaling.

## 5.4 Summary

The photonic band structures of an ABR containing SNG materials have been theoretically examined in this work. With the field solutions of the circular Bragg waves being dependent on the azimuthal mode number $m$, optical properties including the SNG and Bragg gaps at different $m$ modes are examined numerically. The conclusion can be drawn as follows. First, at the lowest mode, $m = 0$, the PBG structure in an ABR is nearly identical to that of a PBR. Second, At higher order azimuthal mode $m \geq 1$, we

find that there is an additional PBG called the MNG gap and the ENG gap for the TE wave and TM wave, respectively. We also find that there exist some reflection dips when $\omega_{mp}$ and $\omega_{ep}$ are taken in the PBG for TE and TM waves, respectively. These results are closely related to the higher order azimuthal mode of the cylindrical wave in an ABR, which are has not be seen in the PBR with SNG materials. Such special filtering responds make it possible to design the structure of a narrowband resonator without introducing any defect layer to break the periodicity. Third, the PBGs are strongly affected by the starting radius in addition to the *m*-number at $m > 0$. The SNG gap is robust to the lattice constant with a fixed thickness ratio of the constituent bilayer. Finally, for an ABR including a defect layer, it is found that the property of the SNG band gap is insensitive to the disorder.

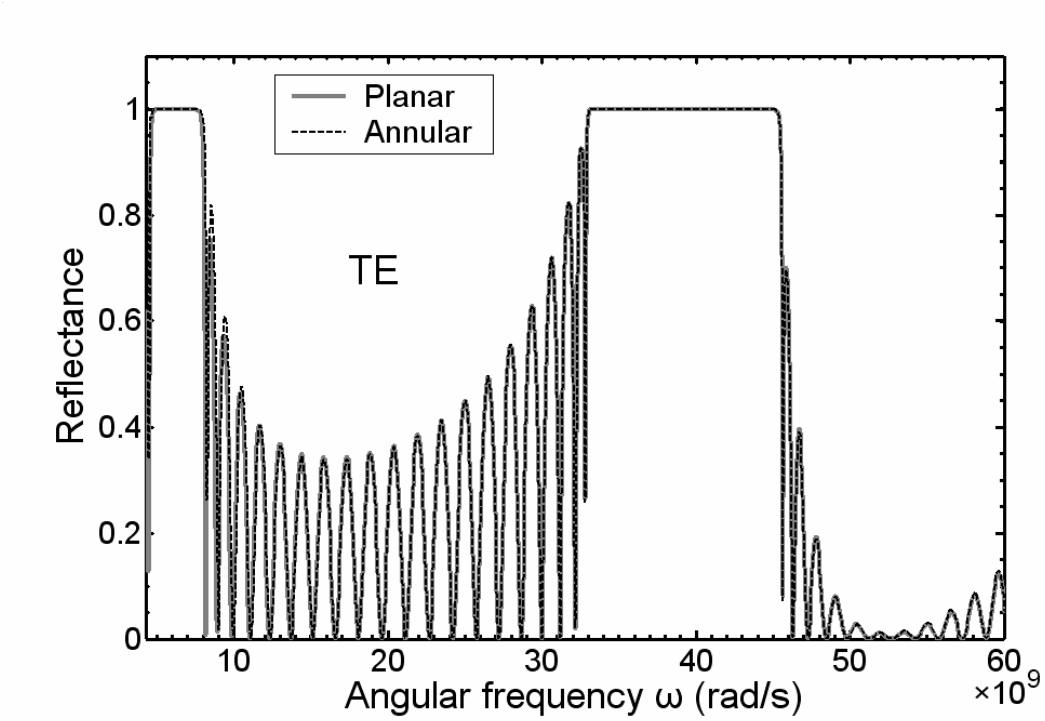


**Fig. 5.1.** Calculated reflectance spectra for MNG/ENG Bragg reflectors, where the gray solid is for the PBR, and the dashed line is for the ABR.

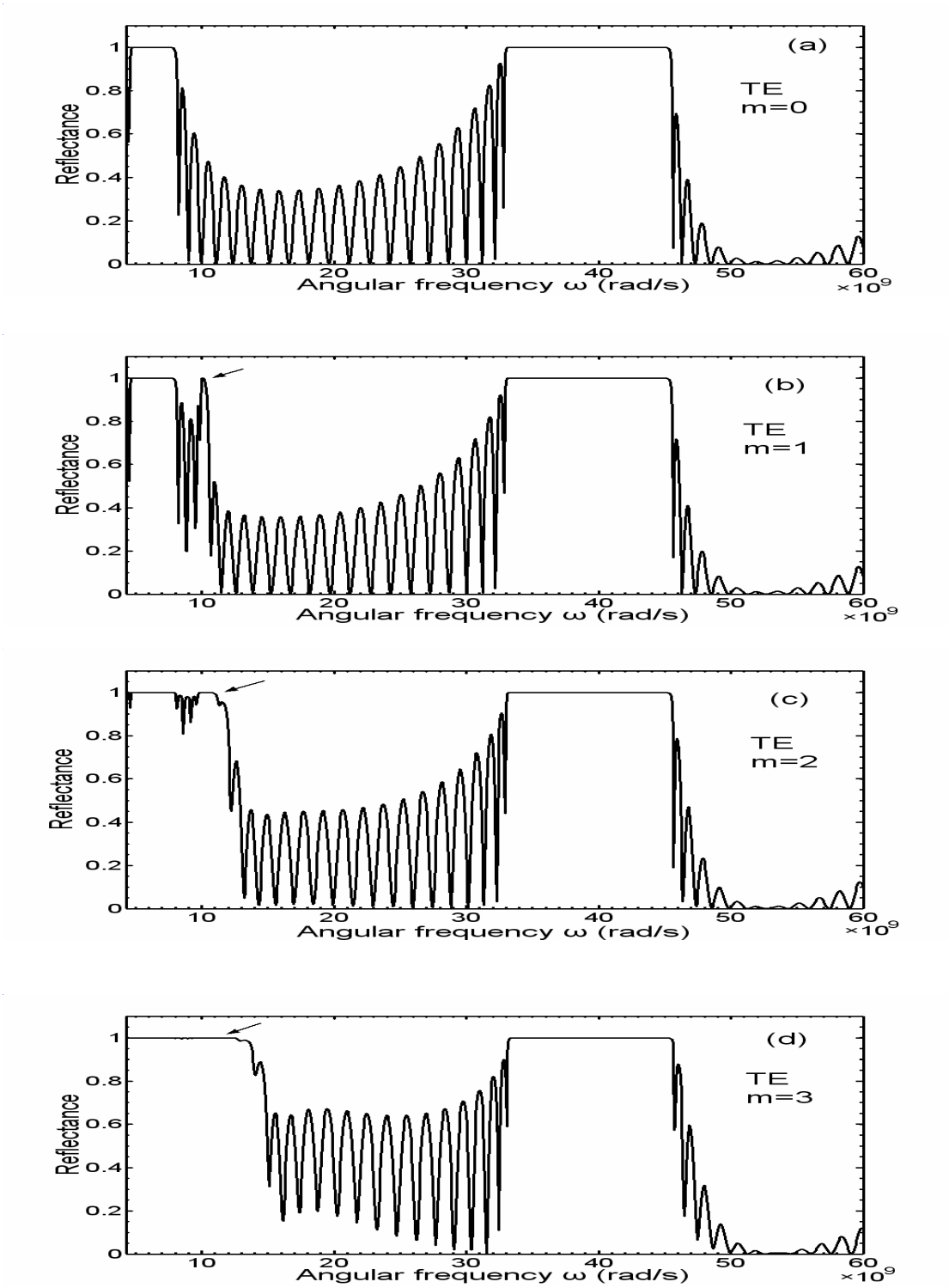


**Fig. 5.2.** Calculated reflectance spectra of TE wave for the ABR at different azimuthal modes (a) $m = 0$, (b) $m = 1$, (c) $m = 2$ and (d) $m = 3$, respectively, under the conditions of $a = 3.5$, $b = 1.2$, $\omega_{mp} = 10^{10}$ rad/s, $\omega_{ep} = 1.3 \times 10^{10}$ rad/s, $d_1 = 10$ mm, $d_2 = 5$ mm, $\rho_0 = 30$ mm and $N = 21$.

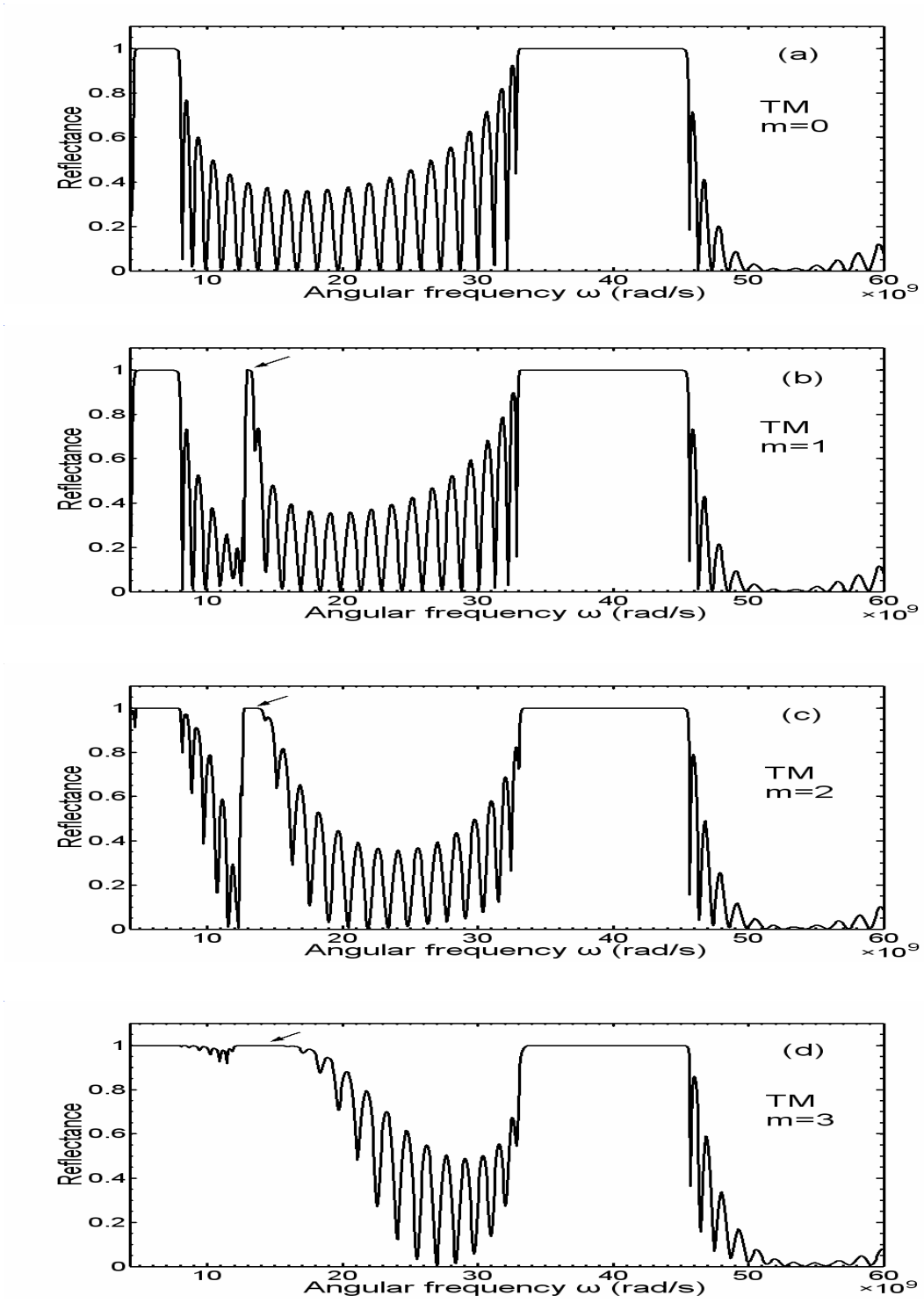


**Fig. 5.3.** Calculated reflectance spectra of TM wave for the ABR at different azimuthal mode (a) $m = 0$, (b) $m = 1$, (c) $m = 2$ and (d) $m = 3$, respectively, under the conditions of $a = 3.5$, $b = 1.2$, $\omega_{mp} = 10^{10}$ rad/s, $\omega_{ep} = 1.3 \times 10^{10}$ rad/s, $d_1 = 10$ mm, $d_2 = 5$ mm, $\rho_0 = 30$ mm and $N = 21$.

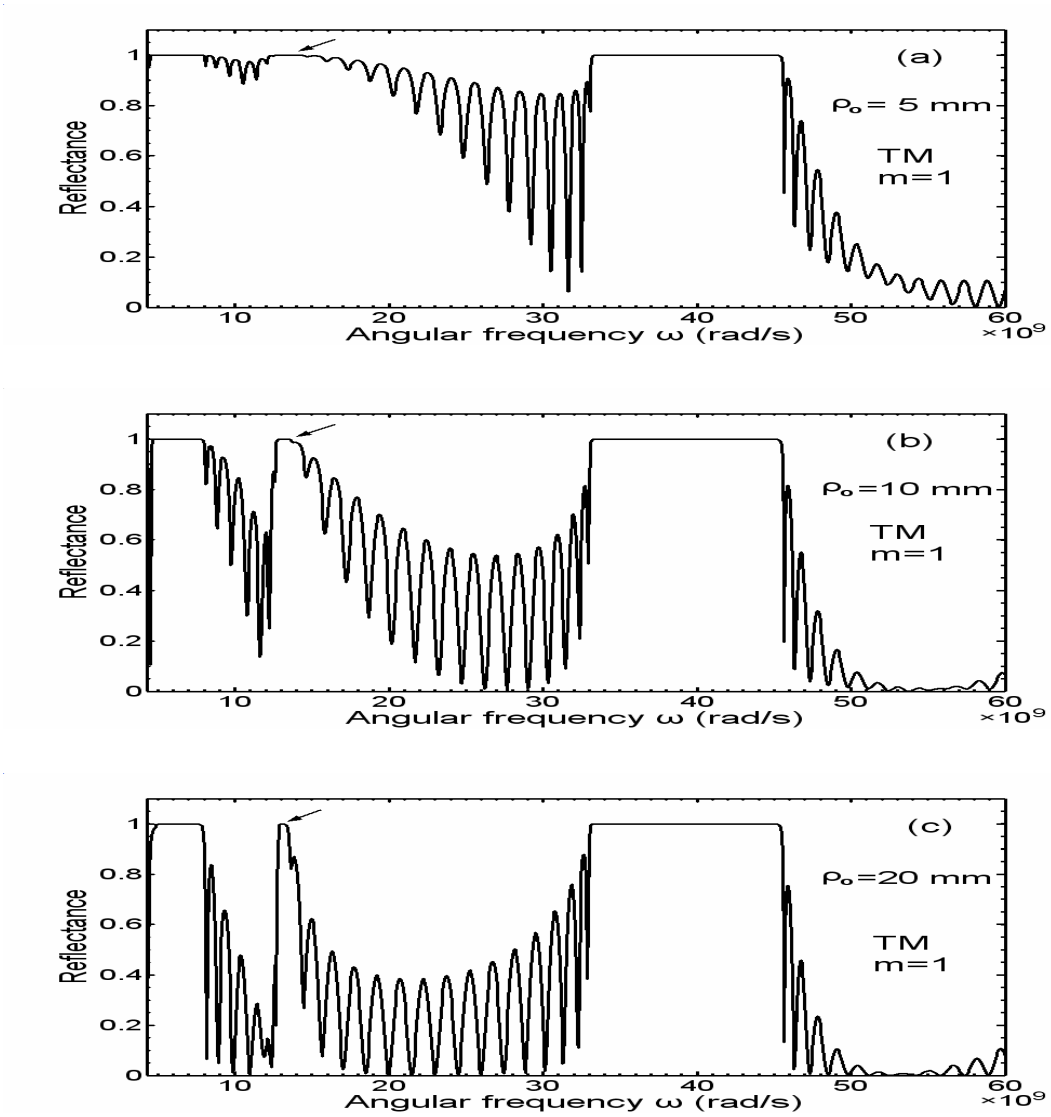


**Fig. 5.4.** Calculated reflectance spectra of TM wave at azimuthal mode $m=1$ for the ABR at different starting radii $\rho_0 = 5\,\text{mm}$ (a), $\rho_0 = 10\,\text{mm}$ (b) and $\rho_0 = 20\,\text{mm}$ (c), respectively, under the conditions of $a = 3.5$ , $b = 1.2$ , $\omega_{mp} = 10^{10}$ rad/s , $\omega_{ep} = 1.3\times10^{10}\,\text{rad/s}$, $d_1 = 10\,\text{mm}$, $d_2 = 5\,\text{mm}$ and $N = 21$.

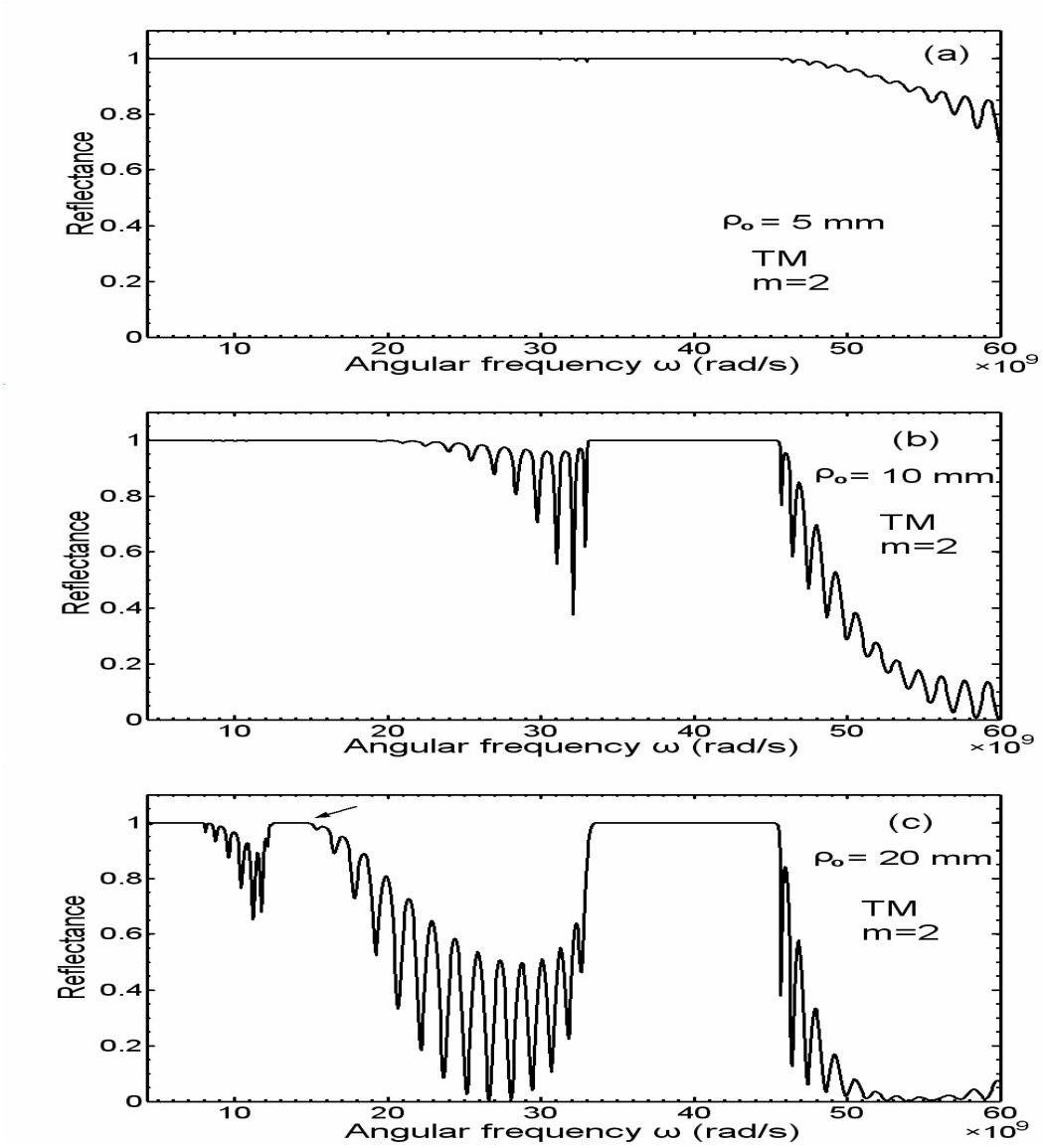


**Fig. 5.5.** Calculated reflectance spectra of TM wave at azimuthal mode $m = 2$ for the ABR at different starting radii $\rho_0 = 5\,\text{mm}$ (a), $\rho_0 = 10\,\text{mm}$ (b) and $\rho_0 = 20\,\text{mm}$ (c), respectively, under the conditions of $a = 3.5$, $b = 1.2$, $\omega_{mp} = 10^{10}$ rad/s, $\omega_{ep} = 1.3\times10^{10}\,\text{rad/s}$, $d_1 = 10\,\text{mm}$, $d_2 = 5\,\text{mm}$ and $N = 21$.

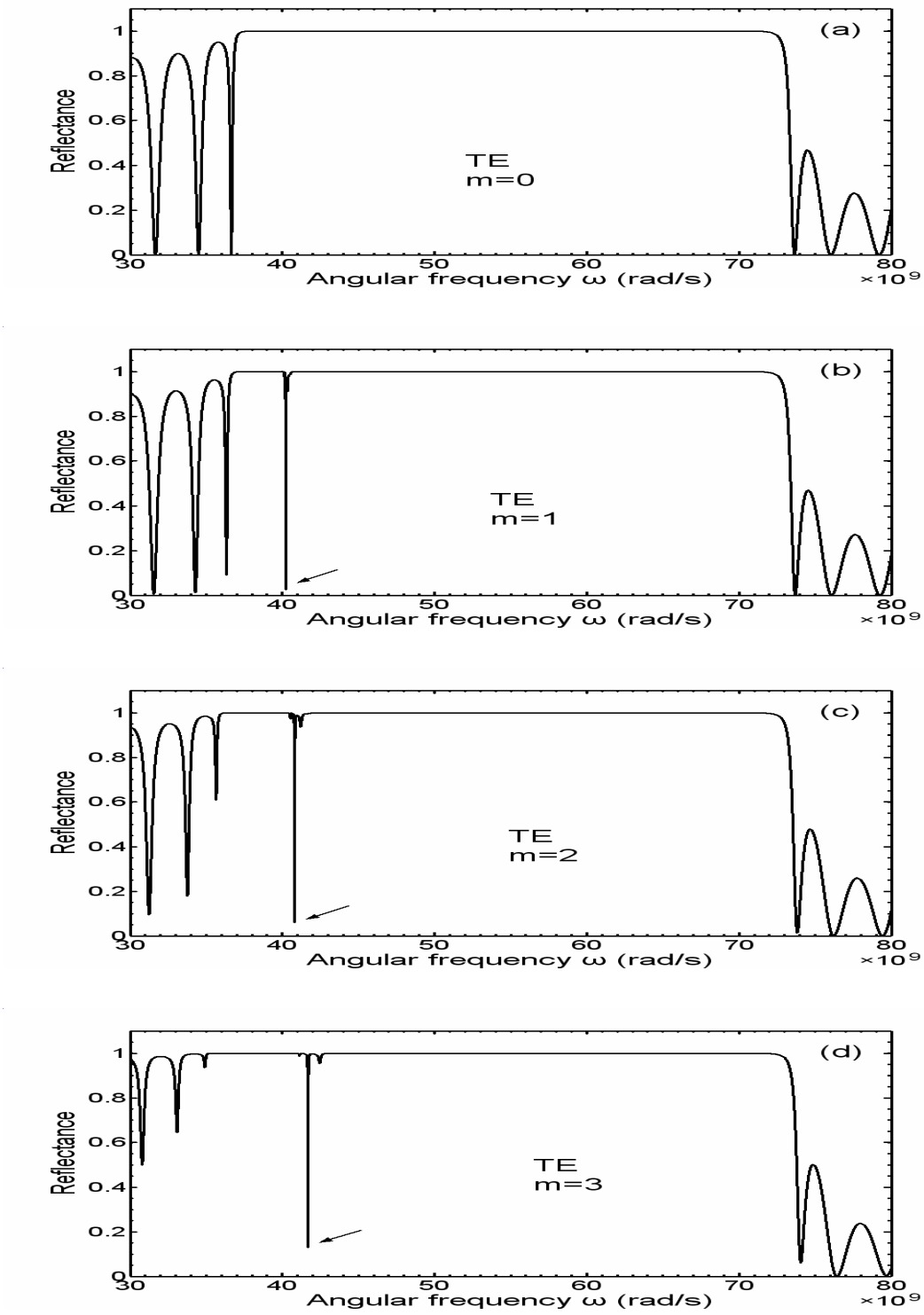


**Fig. 5.6.** Calculated reflectance spectra of TE wave for the ABR at different azimuthal mode $m = 0$ (a), $m = 1$(b), $m = 2$ (c), and $m = 3$ (d), respectively, under the conditions of $a = 6$, $b = 2.5$, $\omega_{mp} = 4\times10^{10}$ rad/s , $\omega_{ep} = 4.5\times10^{10}$ rad/s, $d_1 = 6$ mm, $d_2 = 3$ mm, $\rho_0 = 22$ mm and $N = 6$.

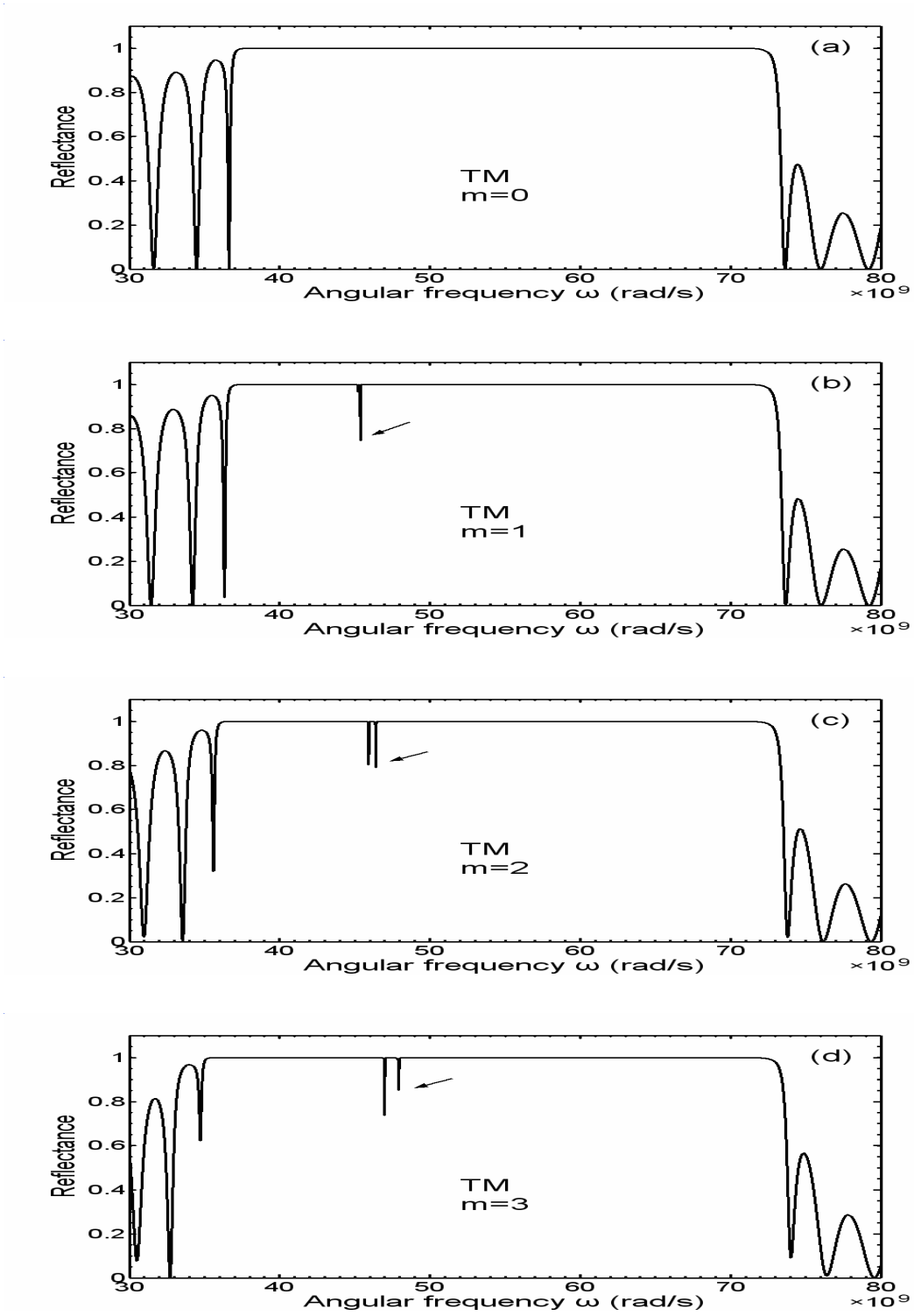


**Fig. 5.7.** Calculated reflectance spectra of TM wave for the ABR at different azimuthal mode $m = 0$ (a), $m = 1$ (b), $m = 2$ (c) and $m = 3$ (d), respectively, under the conditions of $a = 6$ , $b = 2.5$ , $\omega_{mp} = 4 \times 10^{10}$ rad/s , $\omega_{ep} = 4.5 \times 10^{10}$ rad/s, $d_1 = 6$ mm, $d_2 = 3$ mm, $\rho_0 = 22$ mm and $N = 6$.

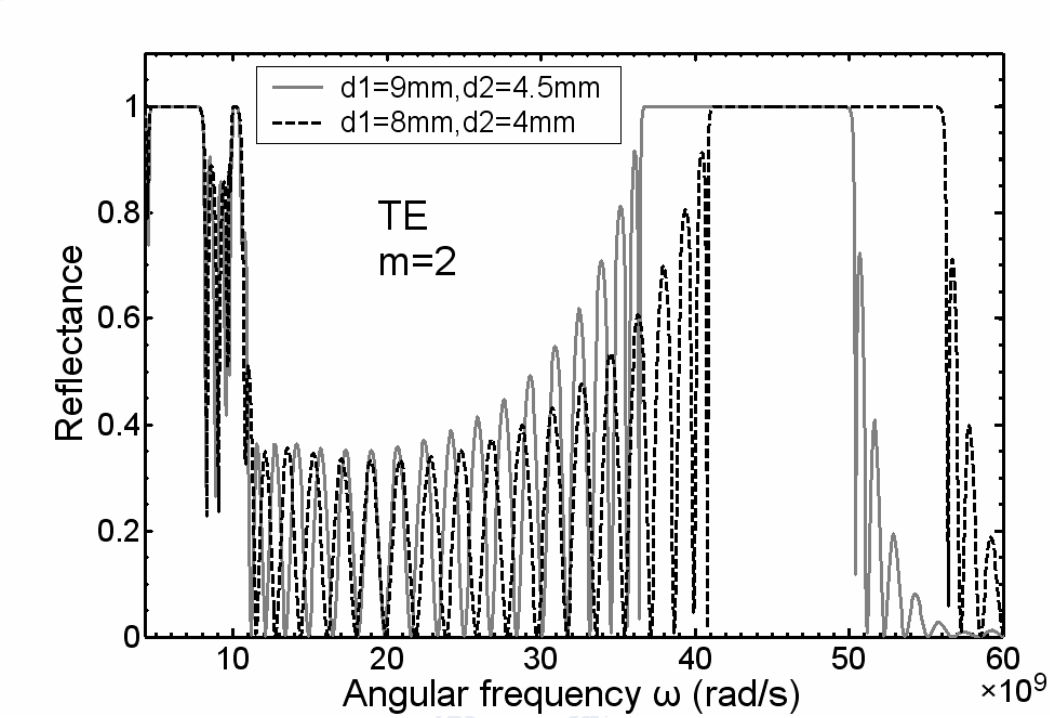


**Fig. 5.8.** Calculated reflectance spectra of TE wave at azimuthal mode $m = 2$ for the ABR, under the conditions of $a = 3.5$, $b = 1.2$, $\omega_{mp} = 10^{10}$ rad/s, $\omega_{ep} = 1.3\times10^{10}$ rad/s, $\rho_0 = 60$ mm and $N = 21$. The gray solid is for $d_1 = 9$ mm, $d_2 = 4.5$ mm. The dashed line is for $d_1 = 8$ mm, $d_2 = 4$ mm (scaled by $8/9$).

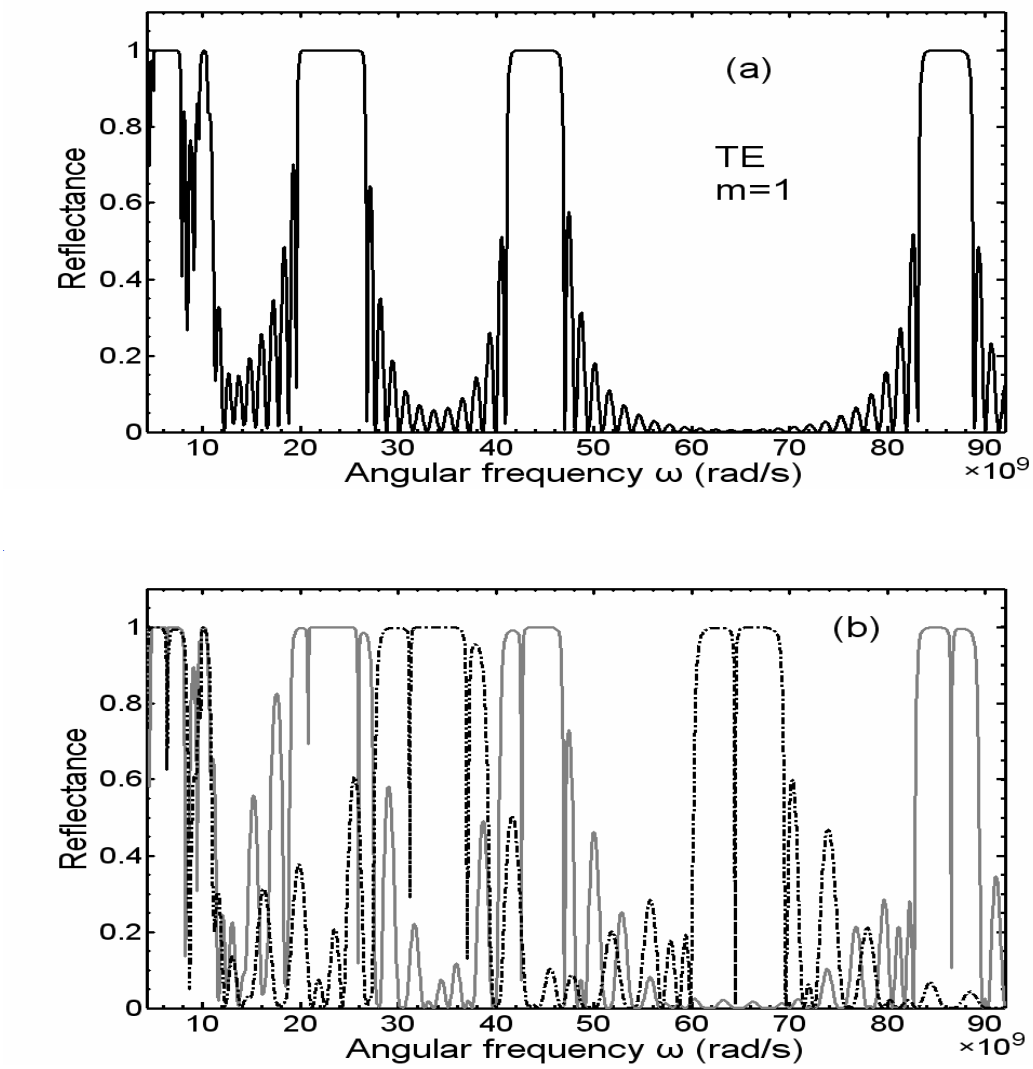


**Fig. 5.9.** Calculated reflectance spectra of TE wave at $m=1$ for the ABR. The material parameters are $a=1.5$, $b=1.5$, $\omega_{mp}=10^{10}$ rad/s , and $\omega_{ep}=10^{10}$ rad/s. The spectrum with no defect is in (a), where $d_1=24$ mm, $d_2=12$ mm, $\rho_0=30$ mm and $N=13$. The spectrum of structure with defect layer, is shown in (b), where the defect layer has $\varepsilon_d=1.8$, $\mu_d=1.8$ and $d_d=45$ mm. The gray solid curve is for $d_1=24$ mm, $d_2=12$ mm. The dash-dotted curve is for $d_1=16$ mm, $d_2=8$ mm (scaled by $2/3$). The starting radius $\rho_0=30$ mm is used.

# Chapter 6
# Optical properties of an annular periodic multilayer structure containing the double-negative materials

## 6.1. Introduction

Although the concept of a DNG medium (i.e., a double-negative medium with $\varepsilon < 0$ and $\mu < 0$) was first proposed by Veselago early in 1968 [23], it took many years until experimental evidence for the existence of such a medium was presented [24, 25]. The DNG materials are also known as left-handed materials (LHMs) because for an electromagnetic wave propagating in them the electric field, the magnetic field and the wave vector satisfy the left-handed triad contrary to the usual right-handed triad for the ordinary materials. It is equivalent to say that the Poynting vector is antiparallel to the wave vector in a DNG material. A significant result coming from the DNG material is that its index of refraction is negative. Thus, a DNG material is commonly referred to as the negative-index material (NIM). Recently, NIMs were realized by the appropriate combination of conductive and dielectric elements deposited on a substrate [46-51]. In the microwave regime, NIMs are fabricated from metallic wires and rings assembled in a periodic cell structure. The rings are generally referred to as split ring resonators (SRR). NIMs have the property that the effective permittivity $\varepsilon$ and permeability $\mu$ are both negative. This results in an effective negative index of refraction, $n = \sqrt{\varepsilon}\sqrt{\mu}$.

During the last decade, the studies of electromagnetic properties of one-dimensional photonic crystals (1DPCs) and Bragg reflectors (BRs) have attracted

much attention. It is known that a photonic band gap (PBG) could be formed as a consequence of the interference of Bragg scattering in a periodical layer structure. In a usual BR made of all positive-index materials, the high-reflectance band or PBG is called the Bragg gap, which is proven to be strongly dependent on the lattice constant and the disorder of a device as well. However, for the DNG materials $\varepsilon$ and $\mu$ are frequency-dependent. For a BR consisting of DNG materials, i.e., the DNG-dielectric bilayers, it is known to have the photonic band gap different from the Bragg gap. There have been many reports on the one-dimensional plane BRs (PBRs) containing DNG materials [52-56].

We shall theoretically investigate the optical properties in an annular Bragg reflector (ABR) consisting of the DNG-dielectric materials in this work. Based on the transfer matrix method for the cylindrical Bragg waves developed by Kaliteevski *et al.* [11], the photonic band structure is calculated. At first we demonstrate that the frequency-dependent reflectance at $m = 0$ is nearly identical to that of the planar one-dimensional BR containing the DNG materials. Next, the reflectance spectra for the cylindrical wave are plotted and compared at different values of $m$. At the azimuthal mode number $m \geq 1$, it is found that there exist some special phenomena compared with the usual planar BR. In the vicinity of the magnetic plasma frequency and the electronic plasma frequency of the materials for TE wave and TM wave, respectively, an additional high-reflectance band is seen and some reflection dips exist when the plasma frequency is located in the PBG. These two distinct results arising from the higher order azimuthal mode of the cylindrical waves are not found in the PBR consisting of single-negative materials. Such peculiar filtering responses make it possible to adopt the structure in the design of a narrowband transmission filter or an annular resonator without introducing any physical defect layer to break the periodicity.

## 6.2 Theory

An annular periodic multilayer structure which consists of the DNG/dielectric double layers is first introduced. The relative permittivity and permeability for a DNG material are given by [50,51,54]

$$\varepsilon = 1 - \frac{\omega_{ep}^2}{\omega^2}, \tag{6.1}$$

$$\mu = 1 - \frac{\omega_{mp}^2}{\omega^2}, \tag{6.2}$$

where $\omega_{mp}$ and $\omega_{ep}$ are the magnetic plasma frequency and the electronic plasma frequency respectively. We can see that from Eqs. (6-1) and (6-2) the DNG materials can exist when the frequency satisfies $\omega < \min\left\{\omega_{mp}, \omega_{ep}\right\}$ whereas the materials will be double-positive (DPS) if $\omega > \max\left\{\omega_{mp}, \omega_{ep}\right\}$.

The top view of the ABR containing the DNG materials is depicted in Fig. 4.1, where $\rho_0$ is called the starting radius, $n_1$-layer is the DNG material, and $n_2$-layer is the dielectric material. Based on the transfer matrix method for cylindrical wave described in Chapter 2, the reflection and transmission coefficients are determined by the following equations [8],

$$r_d = \frac{\left(M'_{21} + jp_0 C_{m0}^{(2)} M'_{11}\right) - jp_f C_{mf}^{(2)}\left(M'_{22} + jp_0 C_{m0}^{(2)} M'_{12}\right)}{\left(-jp_0 C_{m0}^{(1)} M'_{11} - M'_{21}\right) - jp_f C_{mf}^{(2)}\left(-jp_0 C_{m0}^{(1)} M'_{12} - M'_{22}\right)}, \tag{6.3}$$

$$t_d = \frac{4\sqrt{\varepsilon_0/\mu_0}}{\pi K \rho_0 H_m^{(2)}\left(k_0\rho_0\right) H_m^{(1)}\left(k_0\rho_0\right)\left[\left(-jp_0 C_{m0}^{(1)} M'_{11} - M'_{21}\right) - jp_f C_{mf}^{(2)}\left(-jp_0 C_{m0}^{(1)} M'_{12} - M'_{22}\right)\right]}, \tag{6.4}$$

where $M'_{11}$, $M'_{12}$, $M'_{21}$ and $M'_{22}$ are the matrix elements of the inverse of **M,** $p_0 = \sqrt{\varepsilon_0/\mu_0}$ and $p_f = \sqrt{\varepsilon_f/\mu_f}$ are the admittances of the starting and the last medium for the incident wave, $K = \omega\sqrt{\mu_0\varepsilon_0}$ is the free-space wave number, and

$$C_{ml}^{(1,2)} = \frac{H_m^{(1,2)\prime}(k_l \rho_l)}{H_m^{(1,2)}(k_l \rho_l)}, \quad l = 0, \quad f \,. \tag{6.5}$$

where $H_m^{(1)}$ and $H_m^{(2)}$ are the Hankel function of the first and second kind. Equations (6.3) and (6.4) then leads to the reflectance *R* and the transmittance *T*, i.e.,

$$R = |r_d|^2, \qquad T = \frac{n_f}{n_0}|t_d|^2, \tag{6.6}$$

where $n_0$ and $n_f$ are respectively the refractive indices of the starting and the final media. For the TM wave the corresponding results can be readily obtained by simply replacing $\varepsilon \leftrightarrow \mu$, and $j \leftrightarrow -j$ in the above formulations.

## 6.3 Numerical Results and Discussion

To calculate the photonic band structure, the layer 1 is taken to be the double-negative (DNG) materials with $\omega_{mp} = 2\pi \times 3 \times 10^9$ rad/s and $\omega_{ep} = 2\pi \times 5 \times 10^9$ rad/s [49], and the layer 2 is CaO with $\varepsilon_{2r} = 12$. We assume that the SABR is immersed in free space, i.e, $n_0 = n_f = 1$. The thicknesses of DNG and CaO layers are set to be $d_1 = 7.75\,\text{mm}$ and $d_2 = 3.2\,\text{mm}$, respectively, the starting radius is $\rho_0 = 50\,\text{mm}$ and the number of periods is $N = 10$.

In Fig. 6.1, we investigate the frequency-dependent TE-reflectance, where the gray solid curve is for ABR at the lowest azimuthal mode, $m = 0$, and the dashed curve is for PBR. Because both of the reflection spectra almost coincide, it is indicated that at *m* = 0 the geometric difference due to the curved interfaces in ABR nearly has no effect on the reflectance compared to the PBR. The band gap at frequency higher than $2\pi \times 5 \times 10^9$ rad/s with DPS materials is the usual Bragg gap (BG).

In Figs. 6.2, the TE-reflectance for *m* = 0 (a), 1 (b), 2 (c), and 3 (d) are plotted,

respectively. We find that at $m \geq 1$ an additional PBG appear near $\omega_{mp} = 2\pi \times 3 \times 10^9$ rad/s. Because within this gap the refractive index of the DNG material is much less one and very close to zero, such a PBG is referred to as the near-zero-*n* gap for the DNG material, and can be called the magnetic gap. The magnetic gap is enhanced as *m* increases. At *m* = 2 this additional gap becomes wider than *m* = 1, and at *m* = 3, a further wider gap is obtained, as shown in Fig. 6.2(d). We plot the TM-reflectance for *m* = 0 (a), 1 (b), 2 (c), and 3 (d) in Fig. 6.3. Similar results in Figs. 6.2 can also be obtained for the TM wave. At *m* > 1 an additional gap is now near $\omega_{ep} = 2\pi \times 5 \times 10^9$ rad/s and the additional PBG can be called the electric gap. The electric gap is also enhanced as *m* increases. The results illustrate the effects of the higher-mode cylindrical Bragg wave. In addition, the values in the plasma frequencies, $\omega_{ep}$ and $\omega_{mp}$, will determine the position of the additional magnetic or electric gap. It is evident that magnetic gap is due to the existence of radial component of the magnetic field, $H_\rho$, of TE wave, and electric gap is caused by $E_\rho$ of TM wave. These special results arising from the higher order azimuthal mode of the cylindrical waves are not found in the usual PBR consist of DNG materials. The additional magnetic and electric gaps make it possible that the ABR could be used to design a narrowband transmission filter or an annular resonator without introducing any physical defect layer in the structure.

Similarly to the above chapters, we shall investigate the PBG at which the magnetic plasma frequency $\omega_{mp}$ and the electronic plasma frequency $\omega_{ep}$ are located within it. To reach this end, for TM wave we take the conditions the conditions of $\omega_{mp} = 2\pi \times 3 \times 10^9$ rad/s , $\omega_{ep} = 2\pi \times 5 \times 10^9$ rad/s, $n_2 = \sqrt{12}$ , $d_1 = 6$ mm, $d_2 = 7$ mm, $\rho_0 = 70$ mm and $N = 10$. In Fig.6.4, it is shown that for TM wave $\omega_{ep}$ is located within

the PBG and there are dips near $\omega_{ep}$ at mode $m \geq 1$. Then for TE wave $\omega_{mp} = 2\pi \times 3 \times 10^9$ rad/s , $\omega_{ep} = 2\pi \times 5 \times 10^9$ rad/s, $n_2 = \sqrt{12}$, $d_1 = 25.5$ mm, $d_2 = 15$ mm, $\rho_0 = 13$ mm and $N = 11$ are taken in our calculation. It is seen in Fig.6.5 that $\omega_{mp}$ is located within the PBG and there are dips near $\omega_{mp}$ at mode $m \geq 1$ for TE wave. The appearance of such dips in reflectance is mainly due to the higher azimuthal mode of the cylindrical wave, which, in fact, does not show up in the PBR in the normal-incidence case. In the same reason of electric and magnetic gap, these dips have relationship with $H_\rho$ of TE wave and $E_\rho$ of TM wave.

## 6.4 Summary

We have theoretically examined the photonic band structures of an ABR containing DNG materials. With the fact that the field solutions of the cylindrical Bragg waves for both TE and TM waves are dependent on the azimuthal mode number denoted by $m$, optical properties including the DNG and Bragg gaps at different $m$ modes are studied numerically. We make the conclusion as follows. First, at the mode $m = 0$, the PBG structure in an ABR is nearly as same as that of a PBR. Second, At higher order azimuthal mode $m \geq 1$, it is found that there is an additional PBG called the magnetic gap and the electric gap for the TM wave and TE wave, respectively. We also find that there exist some reflection dips when $\omega_{mp}$ and $\omega_{ep}$ are taken in the PBG for TM and TE waves, respectively. These unique phenomena are closely related to the higher order azimuthal mode of the cylindrical wave in an ABR, which are has not be seen in the PBR containing DNG materials. Such special filtering responds enables us to design a circular transmission narrowband filter or resonator without introducing any physical defect. to

break the periodicity.

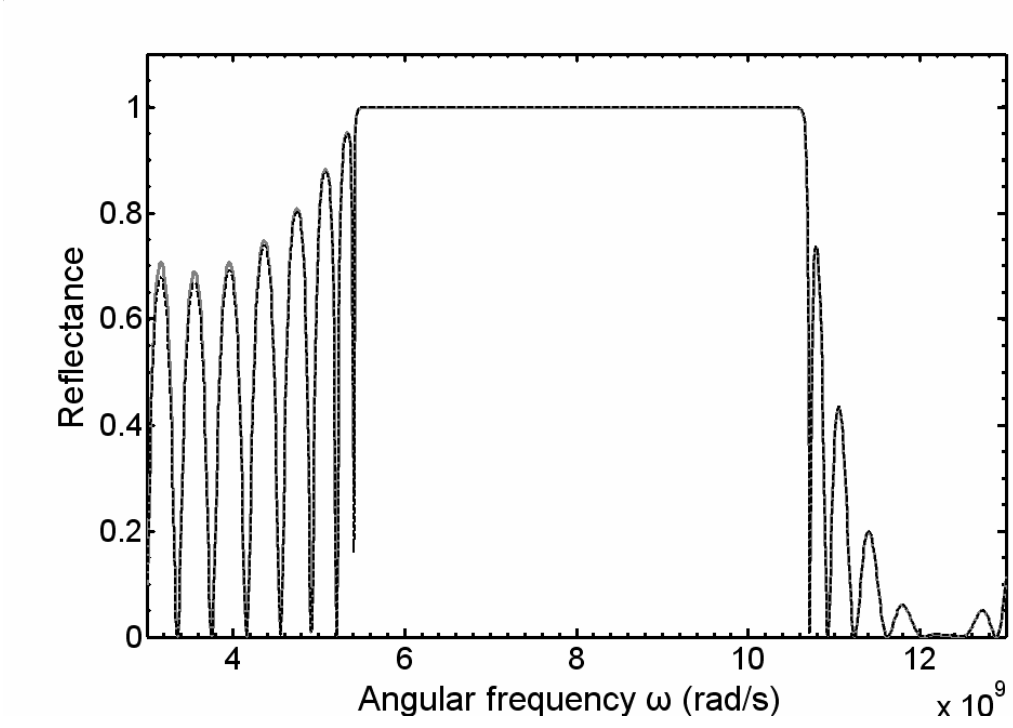


**Fig. 6.1.** Calculated reflectance spectra for DNG/dielectric Bragg reflectors, where the gray solid is for the ABR, and the dashed line is for the PBR.

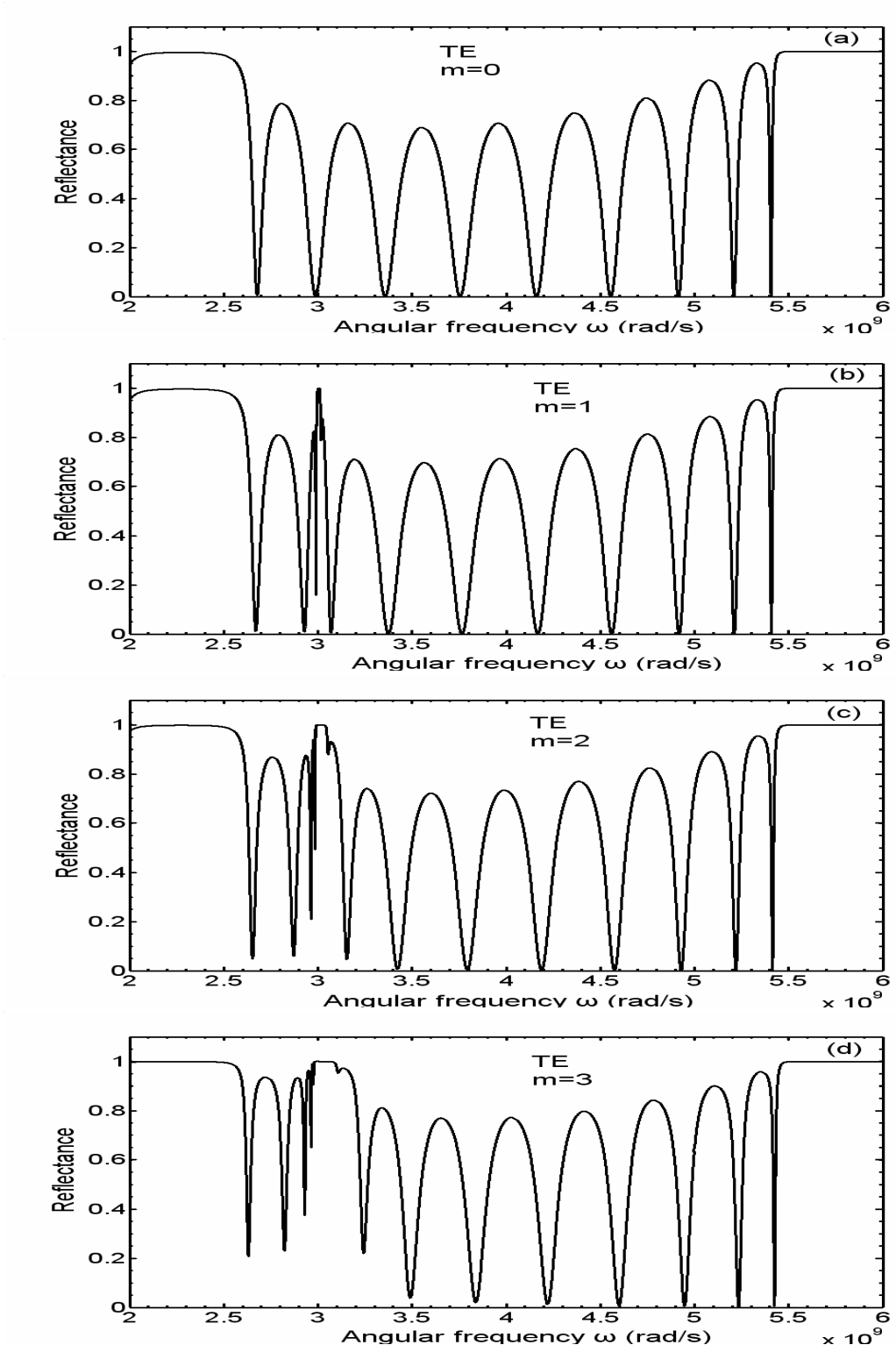


**Fig. 6.2.** Calculated reflectance spectra of TE wave for the ABR with DNG materials at different azimuthal mode $m = 0$ (a), $m = 1$ (b), $m = 2$ (c) and $m = 3$ (d), respectively, under the conditions of $\omega_{mp} = 2\pi \times 3 \times 10^9$ rad/s , $\omega_{ep} = 2\pi \times 5 \times 10^9$ rad/s, $n_2 = \sqrt{12}$ , $d_1 = 7.75\,\text{mm}$, $d_2 = 3.2\,\text{mm}$, $\rho_0 = 50\,\text{mm}$ and $N = 10$.

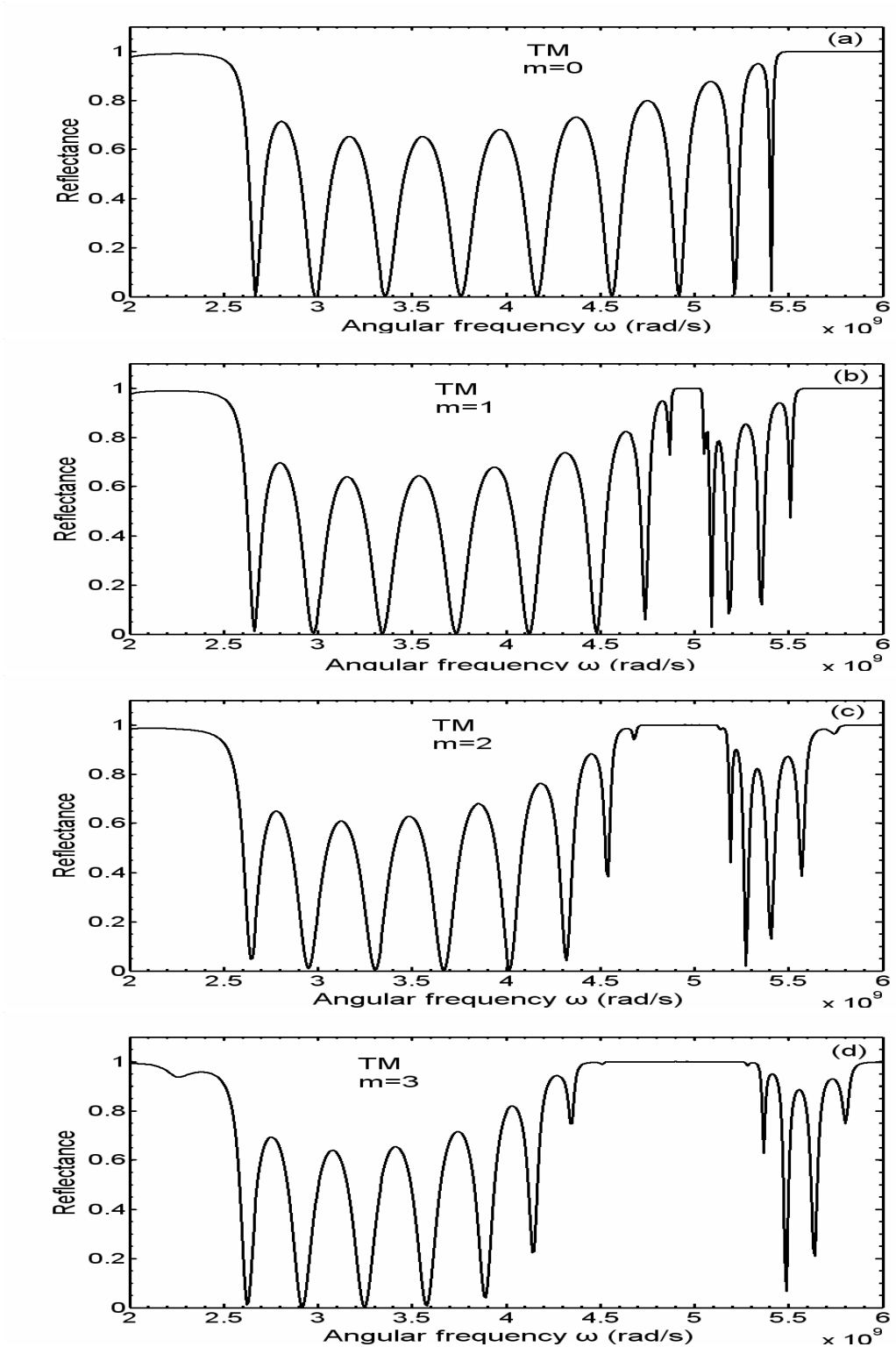


**Fig. 6.3.** Calculated reflectance spectra of TM wave for the ABR with DNG materials at different azimuthal mode $m = 0$ (a), $m = 1$ (b), $m = 2$ (c) and $m = 3$ (d), respectively, under the conditions of $\omega_{mp} = 2\pi \times 3 \times 10^9$ rad/s , $\omega_{ep} = 2\pi \times 5 \times 10^9$ rad/s, $n_2 = \sqrt{12}$ , $d_1 = 7.75\,\text{mm}$, $d_2 = 3.2\,\text{mm}$, $\rho_0 = 50\,\text{mm}$ and $N = 10$.

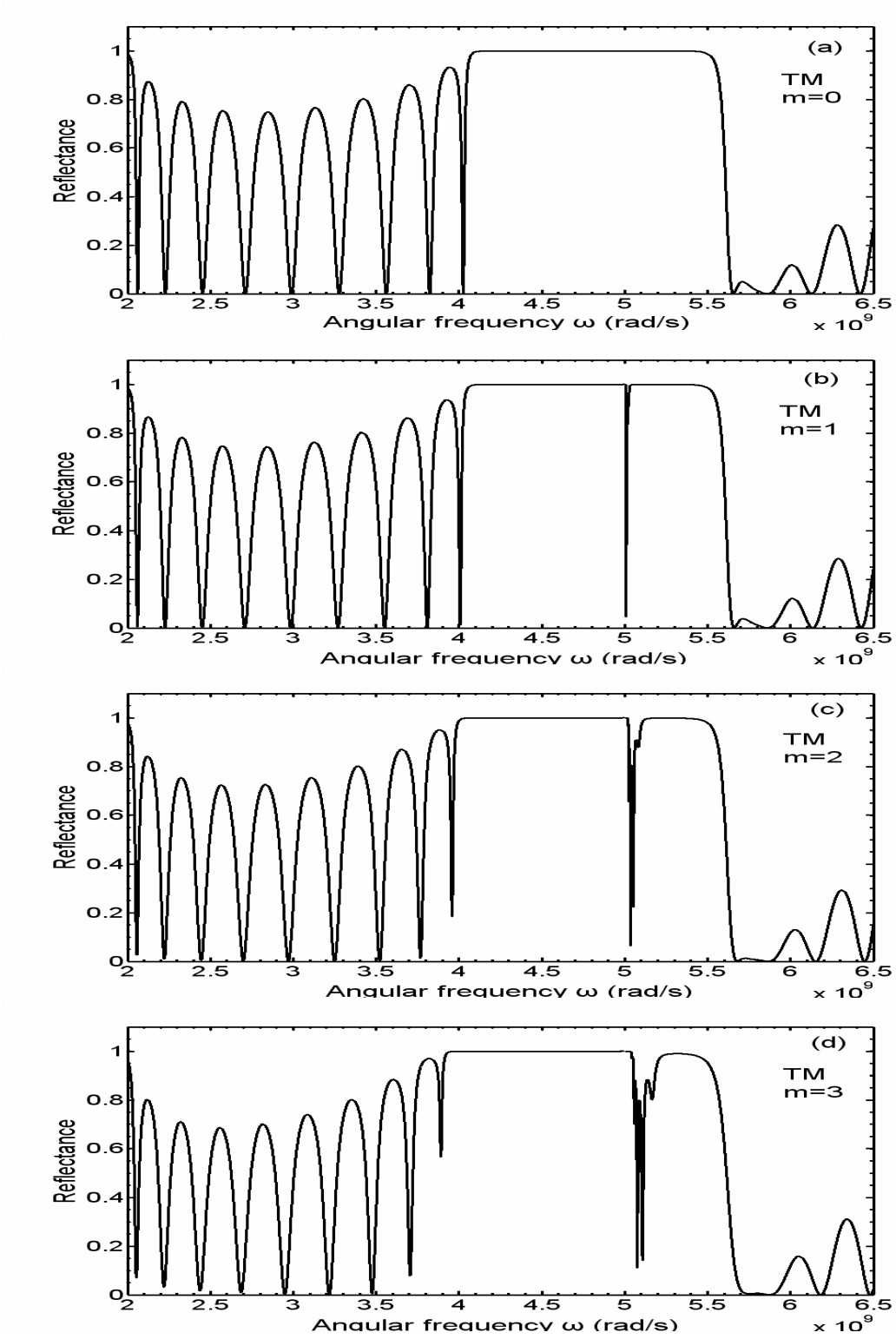


**Fig. 6.4.** Calculated reflectance spectra of TM wave for the ABR with DNG materials at different azimuthal mode $m = 0$ (a), $m = 1$ (b), $m = 2$ (c) and $m = 3$ (d), respectively, under the conditions of $\omega_{mp} = 2\pi \times 3 \times 10^9$ rad/s , $\omega_{ep} = 2\pi \times 5 \times 10^9$ rad/s, $n_2 = \sqrt{12}$ , $d_1 = 6$ mm, $d_2 = 7$ mm, $\rho_0 = 70$ mm and $N = 10$.

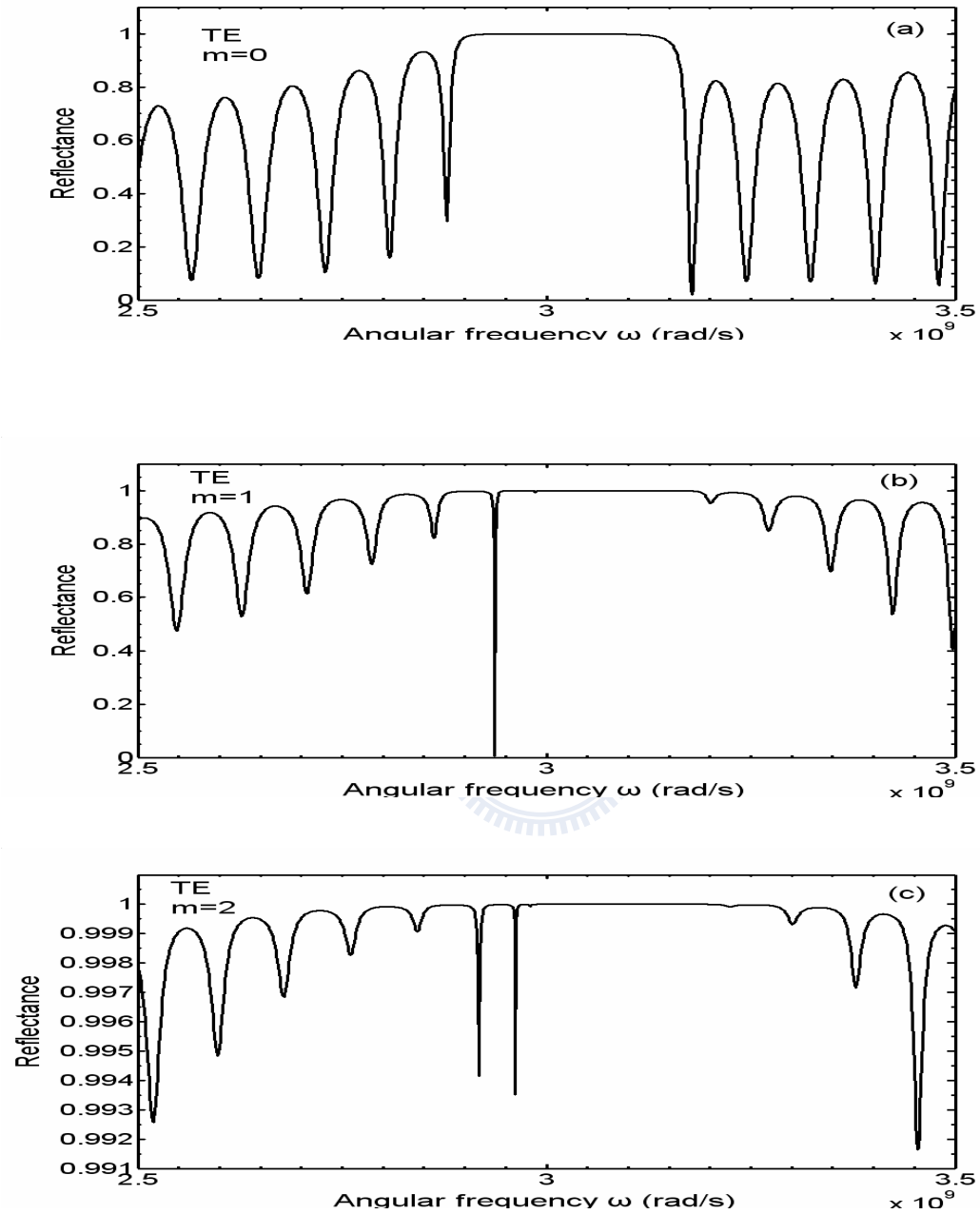


**Fig. 6.5.** Calculated reflectance spectra of TM wave for the ABR with DNG materials at different azimuthal mode $m = 0$ (a), $m = 1$ (b) and $m = 2$ (c), respectively, under the conditions of $\omega_{mp} = 2\pi \times 3 \times 10^9$ rad/s , $\omega_{ep} = 2\pi \times 5 \times 10^9$ rad/s, $n_2 = \sqrt{12}$ , $d_1 = 25.5$ mm, $d_2 = 15$ mm, $\rho_0 = 13$ mm and $N = 11$.

# Chapter 7
# Conclusions

In this dissertation, at the beginning the photonic band structure in the transversal electric mode for a one-dimensional superconductor-dielectric superlattice is theoretically calculated. By using the Abeles theory for a stratified medium, we first calculate the transmittance spectrum from which all the possible bands can be directly seen. Then we calculate the real photonic band structure based on the transcendental equation derived from the transfer matrix method and Bloch theorem. The band structure is shown be strongly consistent with the transmittance spectrum. Moreover, we find that there are an additional PBG or dips appear near $\lambda_{th}$ in the oblique-incidence case.

Next, we are dedicated to the annular Bragger reflectors. The optical properties of an annular periodic structure made of superconducting and dielectric layers are theoretically investigated. By using the transfer matrix method for the cylindrical waves, we calculate the reflectance spectra for such a superconducting annular Bragg reflectors (SABR). Numerical results show that the optical properties of SABR are fundamentally different from those of the planar Bragg reflector for the TM wave with azimuthal mode number $m \geq 1$. First, it is found that there is an additional high-reflectance band. Second, there exist some reflection dips near the threshold wavelength of a superconductor. These two special results arising from the higher order azimuthal mode of the cylindrical waves are not found in the usual superconducting plane Bragg reflector (SPBR). The results suggest that the SABR could be used to design a narrowband transmission filter or an annular resonator without introducing any physical defect layer in the structure.

The photonic band structure of an annular periodic multilayer structure containing metamaterials are theoretically investigated based on the transfer matrix method of the

cylindrical waves. At the azimuthal mode number $m \geq 1$ and near the magnetic plasma frequency and the electronic plasma frequency for the TE wave and TM wave, respectively, we find that there is an additional high-reflectance band and some reflection dips exist when the plasma frequency is located in the photonic band gap. These two special features arising from the higher order azimuthal mode of the cylindrical waves are not seen in the planar one-dimensional Bragg reflector consisting of the metamaterials. Such filtering responses provide a feasible way of designing a narrowband resonator without physically introducing any defect layer in the structure.

# Reference


[1] E. Yablonovitch, Phys. Rev. Lett. 58 (1987) 2059.

[2] S. John, Phys. Rev. Lett. 58 (1987) 2486.

[3] J. D. Joannopoulos, R. D. Meade, and J. N. Winn, *Photonic Crystals*, Princeton University Press, New Jersey, 1995, p. 41.

[4] K. Sakoda, *Optical Properties of Photonic Crystals*, Springer Series in Optical Sciences, 2001.

[5] K.W-K Shung and Y-C Tsai, Phys. Rev. B 48, (1993) 11265.

[6] E. Yablonovitch and T. J. Gmitter, Phys. Rev. Lett. 63, (1989) 1950.

[7] M. Born and E. Wofl, Principles of Optics, Cambridge, London, 1999.

[8] Pochi Yeh, Optical Waves in Layered Media, Wiley, New York, 1988.

[9] William M. J. Green, J. Scheuer, G. DeRose, and A. Yariv, Appl. Phys. Lett. 85 (2004) 3669.

[10] J. Scheuer, W. M. J. Green, G. DeRose, and A. Yariv, Opt. Lett. 29 (2004) 2641.

[11] M. A. Kaliteevski, R. A. Abram, V. V. Nikolaev, and G. S. Sokolovski, J. Mod. Opt. 46 (1999) 875.

[12] Michael Tinkham, *Introduction to Superconductivity*, 2nd ed., McGraw-Hill, New York (1996).

[13] T. van Duzer and C. W. Turner, *Principles of Superconductive Devices and Circuits*, Edward Arnold, London (1981).

[14] P. G.. de Gennes, *Superconductivity of Metal and Alloys*, Addison-Wesley Publishing Company,1989.

[15] K. Fossheim and A. Sudbø, *Superconductivity*, John Wiley & Sons Inc., 2004.

[16] Li L, Zhao B. R., Shi Y. H., et al. Chin. Phys. Lett. 4, (1987) 31.

[17] Tian Y. J., Lu H. B., Xu S. F. ,et al. Physica C, 220, (1994) 114,.

[18] H. Takeda, K. Yoshino, and A. A. Zakhidov, *Phys. Rev. B* **70**, 085109 (2004).

[19] C. H. Raymond Ooi, T. C. Au Yeung, *Phys. Lett. A* **259**, 413 (1999).

[20] C. H. Raymond Ooi, T. C. Au Yeung, C. H. Kam, and T. K. Lim, *Phys. Rev. B* **61**, 5920 (2000).

[21] C.-J. Wu, M.-S. Chen, and T.-J. Yang, *Physica C* **432**, 133 (2005).

[22] O. L. Berman, Y. E. Lozovik, S. L. Eiderman, and R. D. Coalson, *Phys. Rev. B* **74**, 092505 (2006).

[23] V. G. Veselago, Sov. Phys. Usp. 10 (1968) 509.

[24] D. R. Smith, W. J. Padilla, D. C. Vier, S. C. Nemat-Nasser, and S. Schultz, Phys. Rev. Lett. 84 (2000) 4184.

[25] R. A. Shelby, D. R. Smith, and S. Schultz, Science 292 (2001) 77.

[26] J. B. Pendry, Phys. Rev. Lett. 85 (2000) 3966.

[27] H. Jiang, H. Chen, H. Li, and Y. Zhang, Appl. Phys. Lett. 83 (2003) 5386.

[28] J. Li, L. Zhou, C. T. Chan, and P. Sheng, Phys. Rev. Lett. 90 (2003) 083901.

[29] I. V. Shadrivov, A. A. Sukhorukov, and Y. S. Kivshar, Appl. Phys. Lett. 82 (2003) 3820.

[30] Hideo Kosaka, Takayuki Kawashima, Akihisa Tomita, et al. Phys. Rev. B, 58, R10096 (1998).

[31] J. B. Pendry, A. J. Holden, D. J. Robbins and W. J. Stewart, J. Phys. : Condens. Matter 10 (1998) 4785.

[32] J. B. Pendry, A. J. Holden, D. J. Robbins and W. J. Stewart, IEEE Trans. Microwave Theory Tech. 47 (1999) 2075.

[33] A. Alù and N. Engheta, IEEE Trans. Antennas Propag. 51 (2003) 2558.

[34] Neil W. Ashcroft and N. David Mermin, *Solid State Physics*, Thomson Learning, Inc.,

1976.

[35] M. M. Sigalas, R. Biswas, K. M. Ho, C. M. Soukoulis, and D. D. Crouch, Phys. Rev. B 60 (1999) 4426.

[36] V. Kuzmaik and A. A. Maradudin, Phys. Rev. B 55 (1997) 7427.

[37] A. R. McGurn and A. A. Maradudin, Phys. Rev. B 48 (1993) 17576.

[38] R. D. Meade, K. D. Brommer, A. M. Rappe, and J. D. Joannopoulos, Phys. Rev. B 44 (1991) 13772, and Phys. Rev. B 44 (1991) 10961.

[39] L. Feng, X.-P. Liu, J. Ren, Y.-F. Tang, Y.-B. Chen, Y.-F. Chen, and Y.-Y. Zhu, J. Appl. Phys. 97 (2005) 073104

[40] C. P. Poole Jr., H. A. Farach, and R. J. Creswick, *Superconductivity*, Academic Press, San Diego (1995).

[41] Arafa H. Aly, H.-T. Hsu, T.-J. Yang, C.-J. Wu, C. K. Hwangbo, *J. Appl. Phys*. **105**, 083917 (2009).

[42] D. R. Fredkin, and A. Ron, Appl. Phys. Lett. 81 (2002) 1753.

[43] L.-G. Wang, H. Chen, and S.-Y. Zhu, Phys. Rev. B 70 (2004) 245102.

[44] H. Jiang, H. Chen, H. Li, Y. Zhang, J. Zi, and S. Zhu, Phys. Rev. E 69 (2004) 066607.

[45] P. Li, Y. Liu, Phys. Lett. A 373 (2009) 1870.

[46] H. Y. Zhang, Y. P. Zhang, P. Wang, and J. Q. Yao, J. Appl. Phys. 101 (2007) 013111.

[47] G. Guan, H. Jiang, H. Li, Y. Zhang, and H. Chen, Appl. Phys. Lett. 88 (2006) 211112.

[48] J. Li, L. Zhou, C. T. Chan, and P. Sheng, Phys. Rev. Lett. Vo.90, No.8 (2003) 083901.

[49] C. G. Parazzoli, R. B. Greegor, K. Li, B. E. C. Koltenbah, and M. Tanielian, Phys. Rev. Lett. 90 (2003) 107401.

[50] D. R. Smith and N. Kroll, Phys. Rev. Lett. 85 (2000) 2933.

[51] I. V. Shadrivov, A. A. Sukhorukov, and Y. S. Kivshar, Appl. Phys. Lett. 82 (2003) 3820.

[52] D. R. Smith, W. J. Padilla, D. C. Nemat-Nasser, and S. Schultz, Phys. Rev. Lett. 84 (2000) 4184.

[53] Y. Xiang, X. Dai, S. Wen, and D. Fan, Opt. Lett. 33 (2008) 1255.

[54] H. Jiang, H. Chen, H. Li, and Y. Zhang, Appl. Phys. Lett. 83 (2003) 5386.

[55] J. R. Canto, S. A. Matos, C. R. Paiva, and A. M. Barbosa, PIERS Vo.4, No.5 (2008) 546.

[56] Y. Li, L. Ran, H. Chen, J. Huangfu, X. Zhang, and K. Chen, IEEE Trans. Micro. Theory and Tech. 53 (2005) 1522.